Department of Precision and Microsystems Engineering

Design of an inherently fully dynamically balanced aerial manipulator with omnidirectional workspace

Alexander Bom

Report no	:	2024.011
Coaches	:	Dr.ir. V. van der Wijk & Dr.ir. S. Hamaza
Professor	:	Prof.dr.ir. J.L. Herder
Specialisation	:	Mechatronic System Design
Type of report	:	Master Thesis
Date	:	20 February 2024

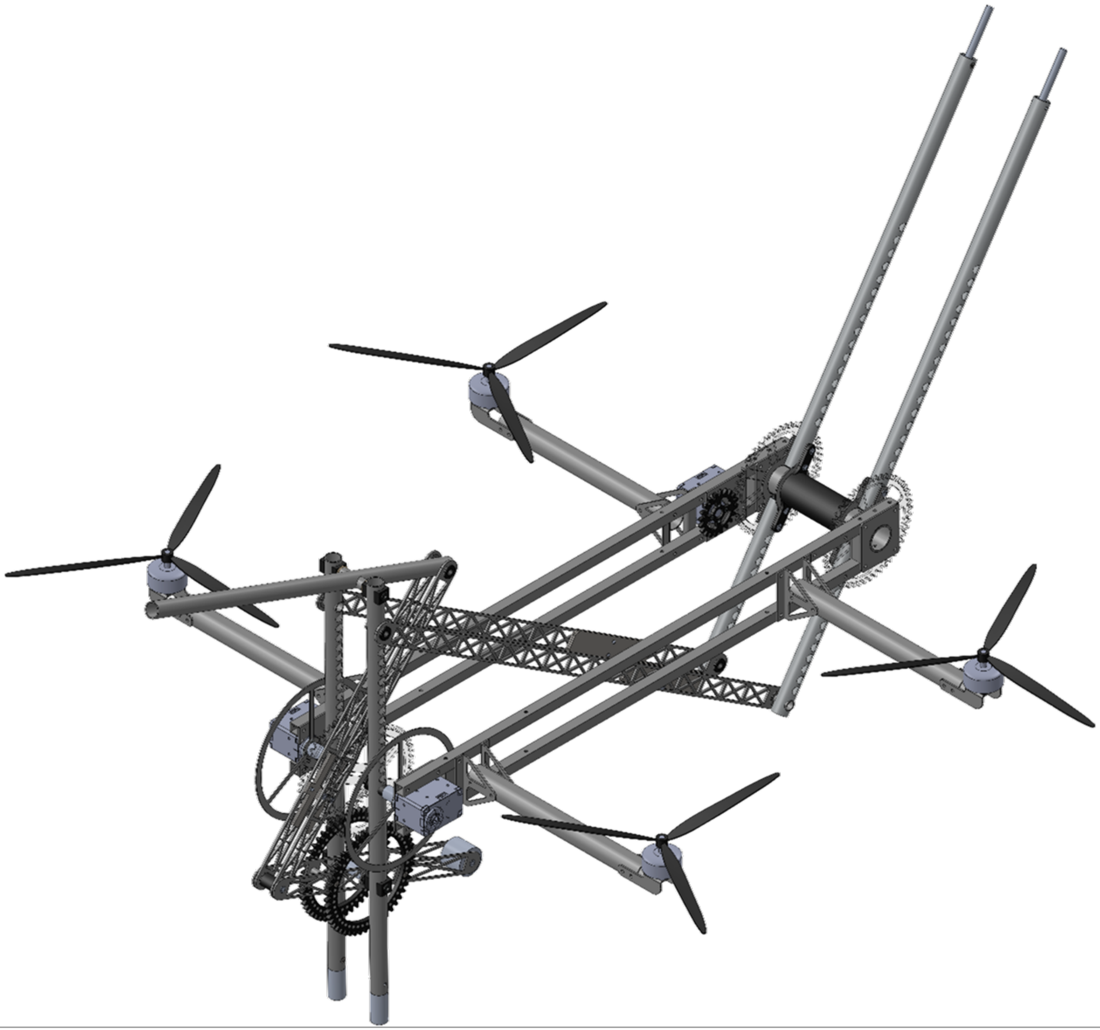

Delft University of Technology

Challenge the future

Design of an inherently fully dynamically balanced aerial manipulator with omnidirectional workspace

by

A.H. Bom

to obtain the degree of Master of Science
at the Delft University of Technology,
to be defended publicly on Tuesday February 27, 2024 at 15:00 PM.

Student number:	4960238	
Project duration:	September 1, 2022 – February 27, 2024	
Thesis committee:	Prof. dr. ir. J.L. Herder,	TU Delft (ME)
	Dr. ir. V. van der Wijk,	TU Delft, supervisor (ME)
	Dr. ir. S. Hamaza,	TU Delft, co-supervisor (AE)
	Dr. ir. J.F.L. Goosen,	TU Delft (ME)

TU Delft

Contents

1

Introduction

On 29 September 1907, the Gyroplane No. I was flown for the first time [1]. Since then, the quadrotor, colloquially known as a 'drone,' has come a long way. Whereas the Gyroplane required four men to steady it and was unsteerable, today's drones are capable of autonomous flight while performing complex maneuvers. These drones, also referred to as unmanned aerial vehicles (UAVs), serve as a flying platform for mounting a variety of tools. Most commonly, cameras are attached to capture aerial footage or perform visual inspections on hard-to-reach infrastructure.

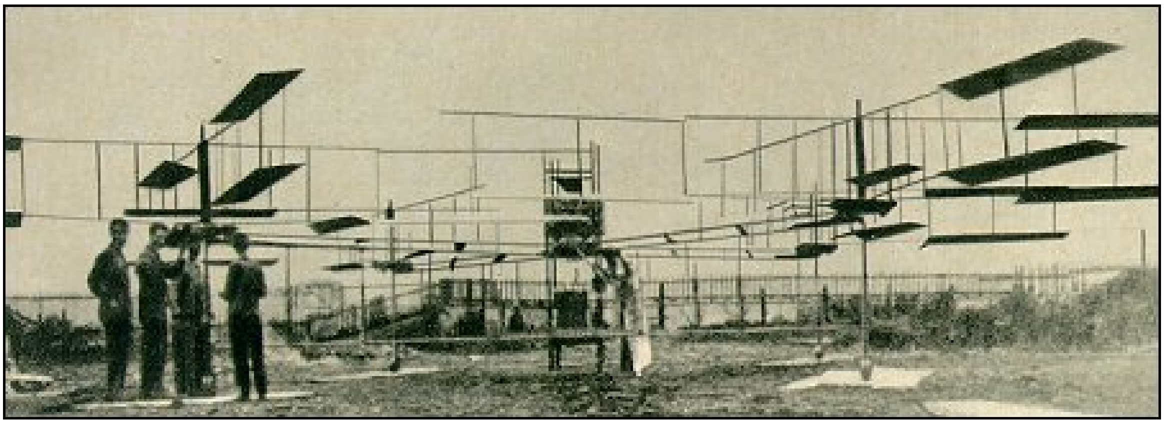

Figure 1.1: Picture of the Gyroplane No.1 built by Louis and Jacques Breguet in association with Professor Charles Richet. The system could lift itself but had to be steadied by four men located at the ground. Source: [1]

The field of aerial manipulation aims to combine the agility of UAVs with the manipulation capabilities of manipulators (robotic arms), creating unmanned aerial manipulators (UAMs). UAMs can be used to perform tasks that are difficult or dangerous for humans, such as sensor placement or infrastructure inspections at height. Existing UAM designs range from so-called flying hands, where a one degree of freedom (DoF) gripper is attached to a UAV, to aerial manipulators equipped with many DoF manipulator arms. Only few designs are able to manipulate below, to the side and above the UAM, limiting the range of applications where UAMs could be used [2]. To gain familiarity with the field, [3] and [4] are recommended. Furthermore these works provide an overview of the common challenges faced by UAMs that need to be addressed for their utilization in industry.

One of these is the disturbance caused by the movement of the manipulator, or in other words the dynamic unbalance. This unbalance shifts the Center of Mass (COM) of the UAM and can exert reaction forces and moments on the UAV. These disturbances directly impact the position and attitude of the UAV, leading to reduced manipulation accuracy. This issue is effectively illustrated in the work presented in [7]. In their study, the researchers demonstrated the benefits of utilizing a manipulator arm by achieving a significant reduction in end-effector error compared to using a rigid arm. Furthermore, they observed how the error increased as the manipulator's motion became faster, due to the larger disturbances. To mitigate this effect, the researchers proposed integrating a dynamic compensation

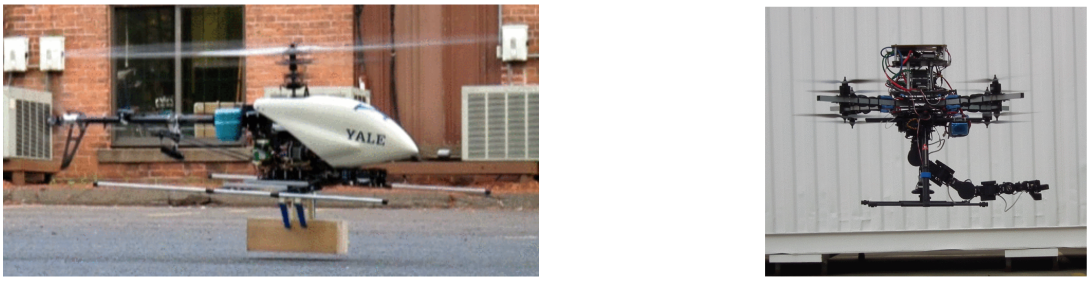

(a) Example of flying hand aerial manipulator, source: [5]. (b) Example of UAM utilizing multi DoF manipulator, source: [6].

Figure 1.2: Two examples of UAMs which illustrate the diversity of aerial manipulators presented in the literature.

term into their control algorithm. However, experimental results indicated a decrease in performance, highlighting the challenge of using control approaches to address this problem. Hence, a mechanical solution avoiding or reducing these disturbances is desired. State-of-the-art UAMs reduce the disturbance created by dynamic unbalance by reducing the mass of the moving components by for instance using parallel manipulator designs which allow for stationary actuator placement close to the UAV's COM [7]. Other examples go a step further by adding active mechanisms which prevent the shifting center of gravity [8], [2]. In [9] a force-balanced delta robot was implemented to reduce the reaction force exerted onto the base.

The field of dynamic balance focuses on designing mechanism such that these do not exert reaction forces and moments to their base. In this field the reaction forces due to the unbalance, are often called shaking forces. The shaking forces can cause vibration, noise, fatigue and wear problems [10]. Similarly to reaction forces, reaction moments can be generated by the movement of a mechanism. The field of dynamic balance can be split up into force balance and moment balance, and once a mechanism is force and moment balanced this is often called full dynamic balance. Combining full dynamic balance with UAMs could therefore lead to UAMs with superior manipulation accuracy as the disturbances caused by the movement of the manipulator can be removed.

To remove the shaking forces, the linear momentum of the system should be kept stationary which comes down to the rule that the general center of mass of a mechanism should be made stationary or should move at a constant rate. In [10], [11], different methods to achieve this can be found. For moment balancing, the angular momentum of the mechanism should be kept stationary. In practice, this means that every rotation requires a counter-rotation. An overview of several methods to moment balance a mechanism is presented in [12].

Generally dynamic balance comes at the cost of an increase in weight and inertia. For the use in aerial manipulation this should be avoided as much as possible, as dynamic balance otherwise could do more harm than good. This is seen in [9], where the use of a force balanced manipulator did not yield significant improvement in the achieved accuracy. Likely caused by the large weight increase due to the balance masses, and the large increase of the moment of inertia of the UAM as the manipulator had to be placed at a large distance from the UAV to accommodate for the balance masses. This demonstrates more work is required to find better ways of integrating dynamically balanced manipulators into UAMs reducing the added mass and inertia. As well as it indicates the importance of using manipulator designs that can be balanced efficiently.

In [13], the increase of weight and inertia was studied, several balance methods were compared by using these to balance a double pendulum. This showed that the best method led to an increase in mass of four times. In an attempt to reduce the added weight, a design shift was proposed. Instead of balancing a mechanism once the kinematics were established, this method proposes to start with balance in mind and construct a mechanism out of an inherently balanced structure [14]. Reducing the need for balance masses by balancing a mechanism using the masses of the links itself. This makes inherent dynamic balance the most promising direction for dynamically balanced manipulators suited for aerial manipulation as it could help to reduce weight. Although it could complicate the integration with an UAV as inherently balanced mechanisms typically consist of many links which could easily interfere with the UAVs components.

1.1. Research Goal

The goal of this thesis is to design a two degree of freedom inherently fully dynamically balanced manipulator with omnidirectional workspace which can be used for aerial manipulation. Dynamic balance enhances manipulation accuracy of UAMs by removing the disturbances created by movement of the manipulator. The omnidirectional workspace makes that the manipulator can be used for a broader set of mission scenarios. A new design approach is used by making a manipulator fly in stead of the common approach of mounting a manipulator arm to a UAV, circumventing interference of the manipulator arm and the UAV.

1.2. Thesis outline

First, a literature study was performed to get insight into the field of aerial manipulation. This study investigated aerial manipulator morphologies to determine which morphology offers the largest workspace, which is the most stable and which is the safest. This is done by comparing various state-of-the-art UAMs based on their morphology and the effect it has on these aspects. The results of this study are presented in chapter two of this thesis. In chapter three the design of a inherently fully dynamically balanced flying manipulator with omnidirectional workspace is presented. In this chapter, the design's kinematics, workspace and balance equations are presented. Furthermore, the design's workspace and mass are optimised. A prototype is built and the balance is validated both by simulation and experiment. In chapter four, the results of this thesis will be discussed. Finally, the conclusions are presented in chapter five. Appendices A, B and C show other design concepts that were considered during the design process. Appendixes D and E give more information about respectively, the motor inertia measurement and the reaction force measurement.

2

Investigation into aerial manipulator morphologies to determine which morphology offers the largest workspace, which is the most stable and which is the safest

Investigation into aerial manipulator morphologies to determine which morphology offers the largest workspace, which is the most stable and which is the safest.

Alexander Bom

***Abstract*—In the field of aerial manipulation much research effort is put into the control of aerial manipulators. In contrary, the influence of mechanical design on the performance of aerial manipulators received less attention. In this work existing, unmanned aerial manipulator (UAM) designs are categorized based on the placement, i.e. morphology of the manipulator. For the different morphologies, a set of representative examples will be shown, and their key features are listed. The morphologies are compared to find which morphology offers the largest workspace, which is the most stable and which is the safest.**

***Index Terms*—Unmanned aerial manipulator, UAV, UAM, Morphology.**

I. INTRODUCTION

Recently, the COVID pandemic showed how useful automation can be. Robots were used in all sorts of cases to keep our society working [1]. Not only are robots useful in the case of a pandemic, but robots can help out with other problems too. ‘Europe’s working-age population is shrinking and we need to find ways to sustain economic growth by bringing more people into jobs and increasing productivity.’ [2] A solution for this can be found in automation. A specific example of a direction that could help is the area of aerial manipulation. Already in 2009, this type of robotics appeared on the European robotic strategic research agenda [3]. Bridge inspection, inspection of pipes, and maintenance of powerlines are examples where aerial manipulators could be used to lighten the workload, or improve safety.

In the last years, much research effort has been put into the field of unmanned aerial manipulators (UAMs), which led to many unique designs. Often the designs consist of an unmanned aerial vehicle, referred to as UAV, to which a manipulator is mounted. The manipulator design depends on the task/research that is performed with the UAM. In many studies found in this area, most effort is put into the control aspect of aerial manipulation. This can also be seen in the literature reviews found in this field. In [3] a brief review of the control of UAVs, followed by a collection of results reached in research so far can be found. A connection to manipulation in space is made, and is accompanied by a brief review on this topic. A thorough overview of platforms for aerial manipulation and aerial platforms with robotic arms is presented in [4]. In [5] next to an overview of commonly used aerial manipulation systems, a study into realized missions and scenarios can be found. Furthermore, attention is given to modelling methodologies and control schemes for aerial manipulators. These reviews give a good overview of what is available in terms of UAM designs but an analysis of manipulator placement and its effect, especially from a mechanical point of view, is not yet present. This study will investigate existing UAM designs, these will be categorized based on the morphology, in other words, the placement of the manipulator relative to the UAV. These morphologies are compared to answer the research question: which UAM morphology offers the largest workspace, which is the most stable and which is the safest. In this work, the workspace is defined as the ability to operate around the UAV. The reach of the manipulator is of less interest as the UAV itself is also able to move, which makes the area in which can be manipulated theoretically infinitely large. The stability of the UAMs is considered from a mechanical point of view, and does not incorporate control. In this work stability mostly concerns how much the movement of the manipulator influences or disturbs the pose or position of the UAV. This is mostly a problem once accurate positioning of the end effector is required. For instance, the weight distribution, a shifting COM or reaction forces due to the movement of the manipulator can affect the stability of the UAV. These two aspects are key for practical applications of aerial manipulators. Lastly, safety is considered, as it is acknowledged to be one of the challenges that have to be tackled in new generations of UAMs [4]. Especially collisions with the rotors are dangerous, as these spin at high velocity and therefore contain much energy. The risk of collision with the rotor decreases as the UAM can stay further from the object. Another factor is how much the UAM is disturbed by the manipulator and its interaction forces. These could result in positioning errors or even full destabilisation which could lead to a crash.

This paper is structured in the following manner. First, an overview of existing designs per category will be given. These examples will be directly followed by a discussion about the particulars of the respective category. Next, the individual categories will be compared on the workspace, stability and safety of the morphology after which this study will be concluded.

II. MORPHOLOGIES

The UAMs found in literature can be categorised based on many criteria, such as the degrees of freedom (DoFs), the UAV platform used or the type of joint used in the manipulator. In this work, it is chosen to classify the UAMs based on the manipulator’s placement in respect of the UAV. This, to get an overview of the differences coming from this fundamental design decision.

A. *Bottom-Mounted Manipulator*

The bottom-mounted morphology places the manipulator underneath the UAV, and is by far the most common configuration found in the field of UAMs. This morphology does not imply that the workspace has to be limited to the area underneath the drone, only that the manipulator is mounted underneath the UAV. Not all existing examples will be covered but, to the author's knowledge, the main flavours are included and should give a sufficient overview of the state of the art.

An early example of a UAM is presented in [6], the design consists of a helicopter to which a compliant gripper is mounted, see Figure 1A. The stability of the UAM was studied while holding an object with the gripper and appeared to be well within the stable limits. This example only uses a one-DoF gripper but this is certainly not always the case. An autonomous helicopter with a 7 DoF industrial manipulator, depicted in Figure 1F, is presented in [7]. From their initial calculations and experiments, it is found that the inertia forces due to the movement of the manipulator have negligible influence on the helicopter. Significant influence is caused by moving the position of the center of mass (COM) and as a result of interaction forces. This shift in the COM is a more common problem and some designs allow to compensate for it by having additional DoFs. For example, the UAM illustrated in Figure 1C and D uses two arms mounted on a slider which can balance each other out [8]. The UAM depicted on Figure 1 E also uses a slider but then positions the manipulator and its load such that the COM is on the line of symmetry to avoid disturbances in the attitude of the UAV [9].

It is important to mention that the inertia forces can not be neglected in general. For example, in [10] a delta-like manipulator is mounted to the bottom of a UAV, shown in Figure 1J. The design uses an omnidirectional tilt-rotor flying base which makes it possible for the manipulator to manipulate all around the UAV. The manipulator's fast dynamics are exploited to reduce tracking errors. In their work, they noticed the non-negligible dynamics of fast end effector motion, which increased the tracking error in their experiments. Compensating dynamic coupling effects during fast end effector motion by using the base controller to counteract the coupling forces and moments is proposed in [10]. From the results, it is concluded that future work in coupled dynamic controllers is needed. Opposed to control-related solutions also mechanical solutions can be exploited to reduce or even remove the coupled dynamics. In [11], see Figure 1M, another delta-like manipulator is presented. This manipulator is dynamic force balanced which removes reaction forces but still suffers reaction moments. Other examples of bottom mounted delta like manipulators are shown in Figure 1K, I and L, respectively [12], [13], [14].

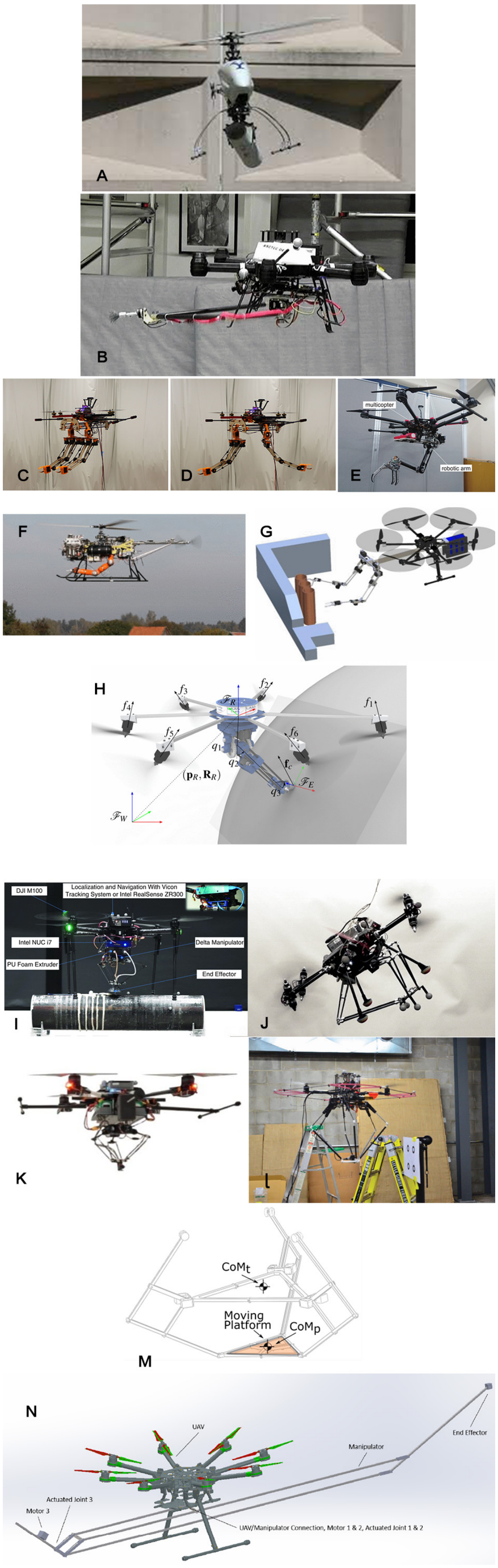

Fig. 1. Pictures of the presented examples of bottom-mounted UAMs. The sources of the pictures are given following the alphabetical order of the pictures themselves. Sources: [6], [15], [8], [9], [7], [16], [17], [13], [10], [12], [14], [11], [18].

Next to the delta configuration other parallel manipulator designs are exploited in existing UAMs. A 3 DoF manipulator, consisting of a 2 DoF parallel 5 bar linkage with an additional rotation is proposed in [15], see Figure 1B. The 3 DoFs make it possible to perform tasks underneath as well as to the side of the UAM. Furthermore, the 3 DoFs allow compensation of small movement and orientation errors of the UAV. The parallel design is chosen for the mass distribution which remains close to the UAV's COM. Another example is a dynamically balanced 2 DoF manipulator, shown in Figure 1N, created by reducing the DoFs of the system by one and actively controlling this DoF to cancel reaction moments [18]. This manipulator is designed such that, although it is mounted underneath the drone, it can reach in front of it beyond the propellers.

Besides parallel also serial manipulators are widely present in this morphology. Figure 1H shows, a 3 DoF manipulator mounted underneath a UAV [17]. The end-effector is equipped with a force and torque sensor to enhance the control method during interaction with the environment. The control method is based on a multi-task optimization problem, which is inspired by whole-body control methods applied to humanoid robots. Another example is a long-reach design, which means the manipulator is placed on a link extending the manipulator's reach outside of the area occupied by the rotors. In this design, see Figure 1G , the link is made compliant and this feature is exploited for collision detection and obstacle localization and allows control of the contact force exerted by the manipulator. The manipulator itself consists of a dual-arm setup, both arms are serial 5 DoF lightweight manipulators. The long reach aims to increase safety during physical interaction with the environment. This setup however places the manipulator's mass far from the UAV's COM and to compensate for this the designers propose to place the batteries on the other side as a counterweight [16].

Discussion

The shown bottom-mounted manipulators have in common that the rotors limit their workspace. In most cases, the UAM is therefore only able to manipulate underneath it. In some cases, the manipulator can also manipulate to the side of the UAM, but their workspace remains below the rotors. How far a manipulator can extend to the side is limited by the shifting COM, as this shift has to be corrected in order to keep the UAM stable. The controller of the drone is able to correct for these changes to a limited extent [19]. In many cases this is therefore compensated by a counter mass, taking the increased weight for granted. The counter mass, for instance a battery, can be placed at a fixed position only balancing the UAM for one configuration. But more advanced solutions are also found in this morphology. For instance, designs C and E shown in Figure 1, use additional dofs to compensate for the shift in COM and design M uses a balanced design keeping the COM stationary over its whole workspace. Another general design approach seen in this morphology which helps keep the UAM stable is placing the heavy components of the manipulator, such as motors, close to the COM of the UAV. This also helps to keep inertia low and the influence of reaction forces relatively small. Lastly, a practical aspect of this morphology is found to be a limiting factor for the workspace. The landing gear, see for instance Figure 1A, B, F, G, J and N, that is commonly used to land the UAM on is also located underneath the UAV. This forms an obstacle for the workspace of the manipulator and could result in a smaller achievable workspace.

B. Top-Mounted Manipulator

The placement of the manipulator on top of a UAV might not be logical at first, as intuitively this morphology might seem unstable. The stability under additional load of conventional helicopters and quadrotors is investigated in [19]. The quadrotor showed to remain stable for loads applied on top, in other words above the COM of the quadrotor.

For rigid tools, so once the manipulator holds a static configuration, it is even shown to be beneficial if the tooltip, i.e. end effector, is positioned above the COM of the system. It is shown to be a necessary condition for internal stability when one wants to control the position of the tooltip [20]. As mentioned in [3] a similar study for aerial manipulators is missing. However, from this stability does not seem to be an issue, yet significantly fewer examples are found in literature.

The most common concept places a one-DoF gripper on the drone to create a so-called flying hand, which attaches to an object above the UAV see for instance Figure 2A and E, respectively [21], [22]. Other cases extend this with an additional manipulator, for example the UAM in Figure 2B, where a bottom-mounted manipulator is added [23]. The top-mounted gripper is utilized to hang itself from an object and stabilize the UAV which saves energy while manipulating. Also, more advanced manipulators can be found in literature, such as [24] shown in Figure 2D, where a design consisting of a five-DoF serial manipulator attached to the top of the UAV is proposed. In this paper, a special control method is applied and tested. The experiments performed with this platform resulted in an interesting finding, namely the contact force between the end-effector and the environment (in this case a bridge) did not cause destabilisation and even seemed to improve stability, while the pitch and roll oscillations decreased during contact. Furthermore, in [25] a top-mounted serial manipulator is proposed to use in the application of mounting sensors, see Figure 2C. Their simulations show that their adaptive impedance controller is capable of maintaining the required force for placing sensors. In [26] the manipulator uses a complaint DoF to store the kinetic energy of an impact into potential energy. Furthermore, an additional DoF is used to align the impact force with the COM of the UAV to minimize reaction moments. This combined leads to a manipulator that is able to cope with impacts without any modification to the flight controller. This UAM design is depicted in Figure 2F.

Discussion

Similar to the bottom-mounted morphology, the top-mounted morphology's workspace is limited by the propellers. The area is restricted to the area above and possibly includes the area to the side of the UAM.

In contrast to the bottom-mounted morphology, this space on top of the UAV is mostly unoccupied and therefore available for the manipulator. The designs found using this morphology do not show advanced balancing solutions to keep the COM stationary. But, the design principle which places heavy components close to the base is also a strategy used for the designs in this morphology. Lastly, design F shown in Figure 2 again uses compliance to cope with impact forces, and this could avoid destabilisation of the UAV making the UAM safer.

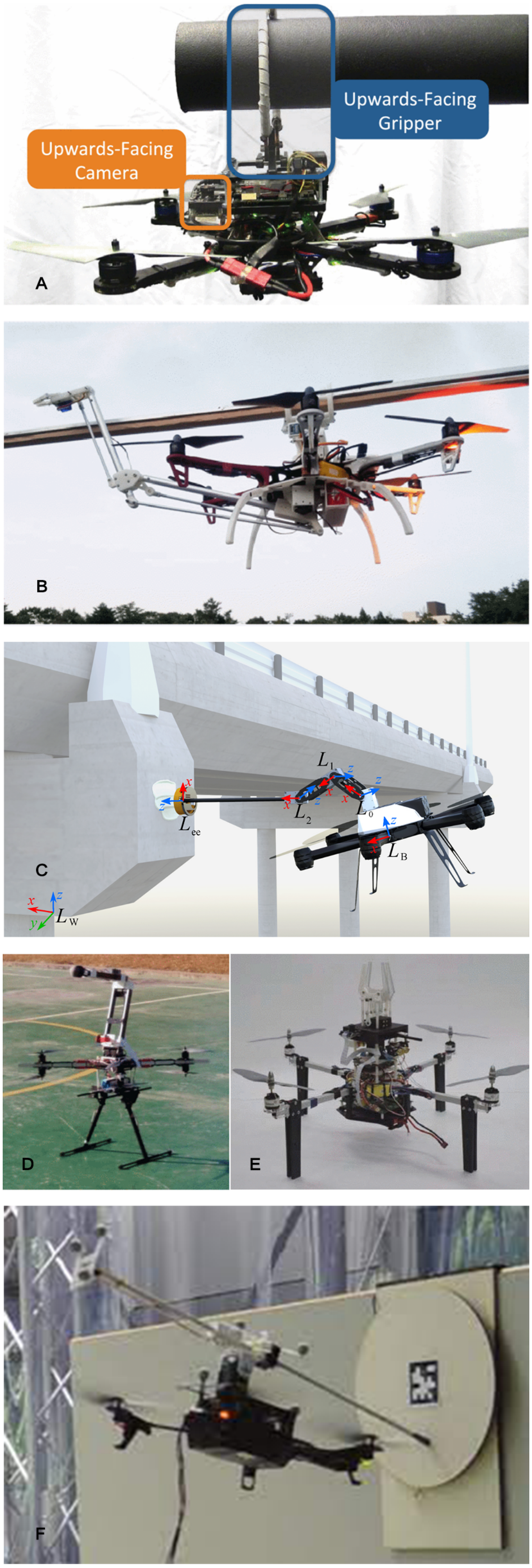

Fig. 2. Pictures of the presented examples of top-mounted UAMs. The sources of the pictures are given following the order of the pictures themselves. Sources: [21], [23], [25], [24], [22], [26].

C. Side-Mounted Manipulator

Examples of side-mounted manipulators are rare. To the author's knowledge, only one example containing a manipulator exists. It uses a small delta-like manipulator to lower tracking error during hovering and is used to perform contact interaction with its environment [27], [28], [29]. The actuator is used both on a ducted fan platform, Figure 3A, and on a more conventional quad-rotor, see Figure 3B. Other side-mounted UAMs do exist, these do not possess a manipulator, instead they have tools mounted to the UAV. For example, the UAM shown in Figure 3C, a brush is mounted to the side of a quadrotor. The design also includes an additional propeller to balance the normal force coming from contact [30].

Discussion

As the manipulator is placed on the side of the UAV, already beyond the rotors, it seems easy for the manipulator to manipulate both below, beside and above the UAV. However, examples that are able to do this are not found in literature. A likely cause for this is the undesired distribution of mass, which is due to the placement of the manipulator positioned very far from the COM of the UAV. As mentioned earlier this has to be compensated by a counter mass if the manipulator's weight is significant, leading to heavier designs. This could explain why only a very small and lightweight manipulator is used in the given example. The placement far from the center will increase the inertia leading to slower dynamics and the long moment arm will cause more significant coupling effects in the dynamics, lowering the stability of this morphology. In the example found the manipulation happens in very close proximity to the UAV which is undesired for safety.

D. Suspended Manipulator

The manipulator can also be connected non-rigidly to a UAV. The category of suspended manipulators utilizes ropes or rods to suspend the manipulator underneath the UAV. UAMs designed to interact with plants often make use of this morphology. An example is the Mamba [31], see Figure 4B, where a one-DoF gripper in combination with a cutting device makes it possible to collect samples of plants from hard to reach places. The Rod like manipulator has additional propellers to be able to control its position and correct for disturbances caused by external factors. Another example is the so-called flying tree top sampler, shown in Figure 4A [32]. The sampler consists of a combination of a gripper with a cutting blade that is able to cut a piece from

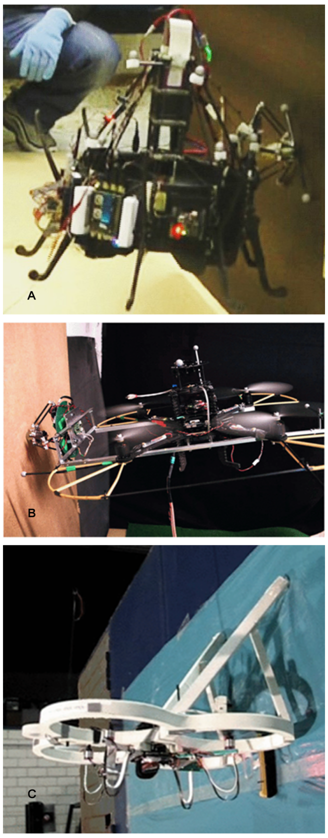

Fig. 3. Pictures of the presented examples of side-mounted UAMs. The sources of the pictures are given following the order of the pictures themselves. Sources: [29], [28], [30].

the tree and take it with it. This device is suspended by 3 pieces of 1m aluminium tubing with custom made motion dampers in between each section. These are used to dampen the pendulum effect once the drone transitions from flying to hovering.

In the case that a UAM has to interact with plants, the suspended setup is used mainly because of two reasons. First, the down wash directly underneath the UAV will affect the plants and make it difficult to grasp the plants. With downwash, the airflow due to the propellers is meant. Secondly, the drone is kept away from the plants. This is beneficial as the plants could easily get caught in the rotors and lead to failure. Outside the scope of interaction with plants, similar reasons are found for the use of the suspended morphology. Figure 4E shows a design where a 2-DOF compliant joint arm is suspended under a UAV by a one-meter-length link in passive pendulum configuration [33]. The larger distance between the obstacles and the UAM increases safety as the reaction time becomes longer. In the paper, the example of maintenance at a chemical plant is used to illustrate the importance of safety for both the drone and the environment.

Besides directly suspending the manipulator another approach can be found in literature, which reduces positioning errors or stability issues due to the suspended setup. Just like the Mamba additional actuators/thrusters are used, but then not directly integrated into the manipulator's design. A separate suspended platform is created and on that platform, a manipulator can be mounted. In [34] a gripper is mounted to a swing suppression platform, see Figure 4D, the system is also equipped with a winch to control the height of the manipulator platform. The suspended aerial manipulator [35], or in short SAM, uses a similar platform to create a stable platform from which a 7 DOF industrial manipulator can operate. The system also uses winches but now to adjust for the change in COM of the manipulator and uses 8 rotors which create a full set of independent torques and forces to decouple the control of position and orientation. Figure 4 C shows the SAM platform, the picture shows the platform which needs to be suspended and should not be mistaken for a UAV.

A similar platform can be created by using multiple UAVs connected to the same platform as shown in Figure 4F. The so-called Fly-Crane System uses three aerial vehicles to support a platform using six cables [36]. The main benefit of this system is that for the control the reasoning mainly comes from the kinematics and the dynamic effects are considered disturbances. This comes with the drawback that accelerations should be kept low, to keep the disturbances and therefore tracking errors low.

Discussion

The suspended morphology has the ability to work underneath a UAV, with little restriction to the shape and size of the manipulator. In the simplest case, the design should allow for just one cable connecting the two. The suspended setup has the advantage that the UAV can stay far away from objects in its environment. This decreases the risk of unwanted contact between UAV and obstacles and increases the reaction time the controller has to cope with disturbances. The non-rigid connection reduces the transmission of impact forces to the UAV, which lowers the risk of destabilisation. The downside of the nonrigid connection is that the manipulator can not exert reaction forces on the UAV and thus complicates controlling the pose of the manipulator. The examples show that this can be resolved with additional actuators.

The suspended designs allow keeping the UAV far from the to be manipulated objects to decrease the influence of downwash created by the rotors. This also holds to a large extent for designs where additional thrusters are used near, or incorporated, in the manipulator while the force that is exerted by these thrusters is commonly much smaller than the forces exerted by the thrusters of the UAV itself as gravity is already compensated [35].

E. Center-Mounted Manipulator

This morphology places the manipulator in the center and constructs the UAV around it. From the examples found this results in the unique ability to manipulate below, beside and above the UAV. The Aerox manipulator, shown in Figure 5A, is an example of such a UAM. The UAM has six degrees of

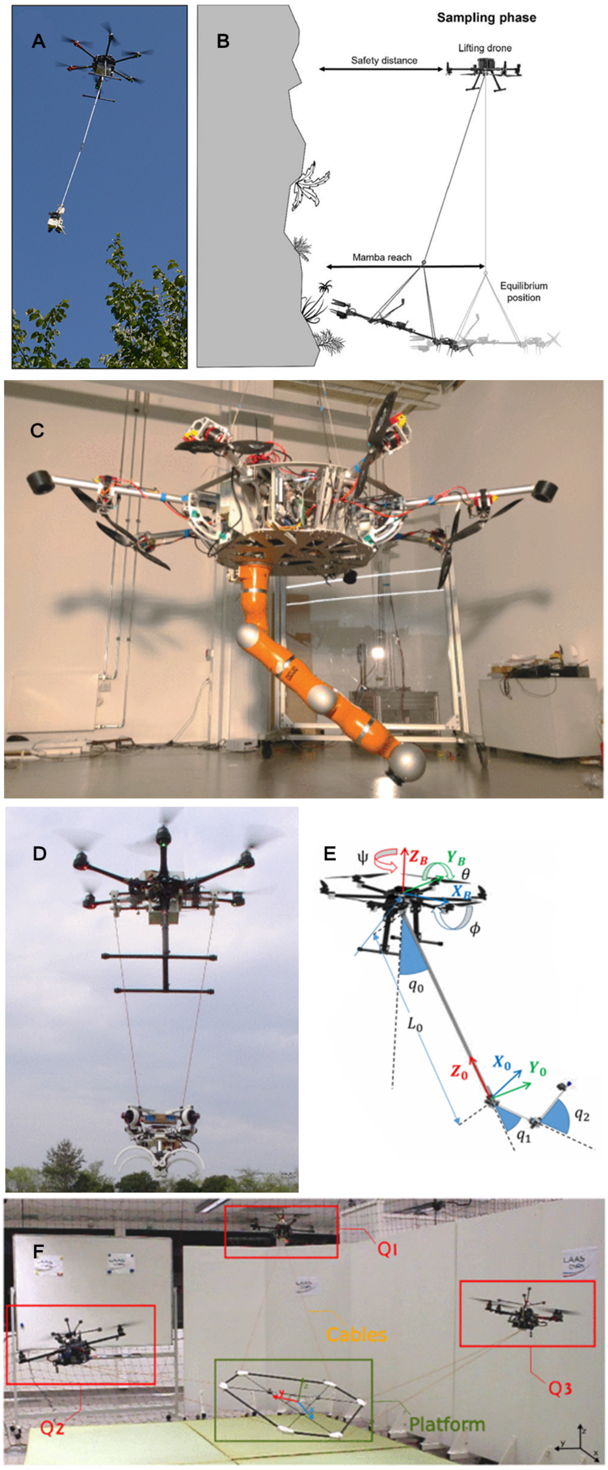

Fig. 4. Pictures of the presented examples of suspended UAMs. The sources of the pictures are given following the order of the pictures themselves. Sources: [32], [31], [35], [34], [33], [36].

freedom the first two are rotations about its geometric center. The third degree is a linear translation along the axis that is going through the geometric center which is also made the COM. This makes that the reaction forces are applied to the COM of the UAM simplifying its stabilization and control [37]. The other three DoFs are rotations of the end effector.

Another example is presented in [38], see Figure 5B. This Omni-Drone consists of a 5-bar linkage plus an additional rotation giving the drone an omnidirectional circular workspace. The counterweight is connected to the same rotational flange as the 5-bar linkage and has an additional DoF to balance the load held by the end-effector.

Discussion

Placing the manipulator in the center of the design and constructing the UAV around it has a benefit. As seen in the examples it is the only morphology found that houses a manipulator that is able to manipulate all around the UAV, although limited to a spherical workspace. This makes the manipulator versatile and can therefore be used for many different tasks. Furthermore, this morphology has a lot of design freedom which allows for beneficial design features, a noticeable example in both designs is the placement of the counterweights, they are mounted in such a way that they rotate with the manipulator to improve balance throughout the entire workspace. The movement of the manipulator has therefore less effect on the UAV, but in these designs reaction forces are not prevented. The examples found in this morphology have to manipulate close to the UAV as the reach of the manipulators is limited, which makes the risk of contact with the rotors higher.

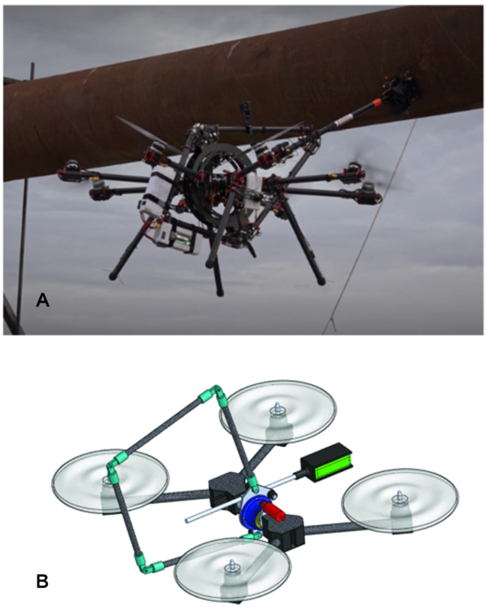

Fig. 5. Pictures of the presented examples of center-mounted UAMs. The sources of the pictures are given following the order of the pictures themselves. Sources: [37], [38].

F. Whole-Body Manipulator

The last morphology distinguishes itself by the use of the UAV as the manipulator, this is also known as whole-body

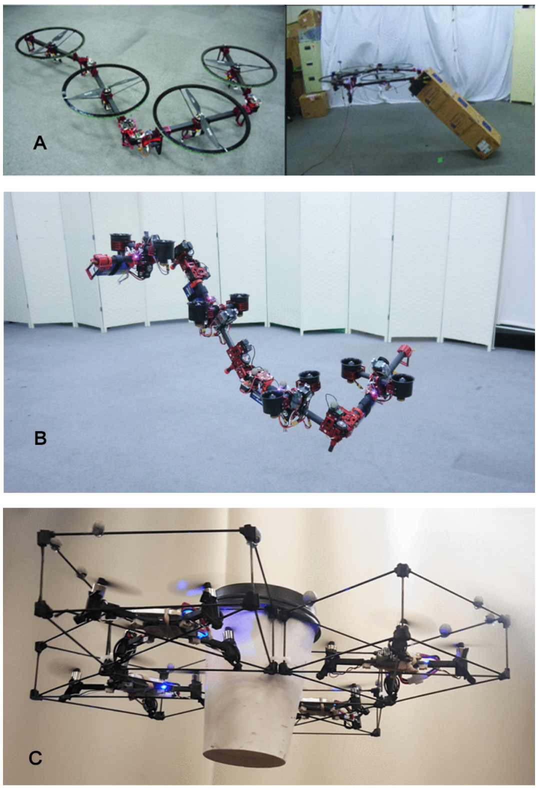

Fig. 6. Pictures of the presented examples of UAV as UAM morphology. The sources of the pictures are given following the order of the pictures themselves. Sources: [39], [40], [42].

manipulation. In the existing literature, two types are found. The first type uses a UAV which is able to change its shape. An example is Hydrus, shown in Figure 6A, which is a transformable multi-link aerial robot. Multiple DoFs are added to the UAV frame which makes it possible to transform into multiple shapes which can be exploited to manipulate objects. The idea behind this design is that the weight and downwash are decreased as an extra manipulator is no longer required [39]. A similar design is shown in Figure 6B, this design called Dragon uses a 2 DoF thrust vectoring mechanism which makes it able to achieve an arbitrary 6 DoF pose in the air [40], [41]. The other strategy is to use multiple smaller UAVs as the links, this is found in [42]. The UAM is shown in Figure 6C, it uses multiple smaller drones that are connected with circular magnets. The drones are all equipped with a lightweight cage which forms the contact point between the environment/object and the UAV.

Discussion

Using the drone as the manipulator is an interesting approach as it avoids the use of an additional manipulator and thereby complexities that follow from the manipulator. Think of the control of the manipulator and coupled dynamics. Unfortunately, the UAV itself becomes more complex in terms of both design and control which evens this more or less out. The weight saving is also considered as moderate as most of the saved parts of the manipulator come back in the UAV's design itself. Furthermore, as the UAV frame is used to manipulate, the rotors have to be in close proximity to the object that is manipulated making the design less safe. Other benefits brought by manipulators, such as faster dynamics to compensate for positioning errors or agility to be able to reach tight spaces are not present in this morphology. Though this class possesses one main advantage, and that is the possibility to adapt the system by adding more links or utilizing more drones to adapt to the use case.

The UAMs using this morphology are able to manipulate to the side of it as the platform commonly has to remain horizontal. The UAM shown in Figure 6B shows that this can be overcome with an over-actuated flying platform, leading possibly to a fully omnidirectional workspace. The stability is harder to evaluate for this morphology as there is no distinguishable manipulator. Moving the manipulator intrinsically means moving the UAV, and complex control must be used to handle this. Lastly, this morphology can be considered inherently more dangerous as there can not be kept distance between the UAM and object, which means the propellers are in close proximity. Furthermore, interaction forces are transmitted directly to the UAM and can cause destabilisation and make the UAM crash.

III. COMPARISON

After analyzing the morphologies individually the gained insights are used to compare them to one another. As mentioned this is done for the workspace of the manipulator, the stability and the safety of the UAM.

Starting with the workspace of the different morphologies. The center-mounted morphology is the only morphology able to manipulate all around the UAM, to create a so called omnidirectional workspace. For clarity and correctness, it has to be stated that the UAM in [10] also has the ability to manipulate omnidirectionally but this is solely achieved by the over-actuated UAV platform and has nothing to do with the manipulator. The same holds for the Dragon drone in the whole-body manipulator morphology. The center-mounted morphology distinguishes itself, as it has the ability to rotate the manipulator around its center, enabling a circular workspace while only utilizing the DoFs of the manipulator.

The bottom and top mounted morphology do not offer an omnidirectional workspace because their workspaces are limited by the rotors and the design would therefore need to be able to go around these propellers to operate above and below the rotors. This would likely lead to a heavy design and cause a large shift of the COM and destabilise the UAM. Example B in Figure 2, nicely demonstrates how the UAM would be able to manipulate above it while the manipulator is mounted below once stability is not an issue. Stability is no issue in this example because moving the manipulator is only intended once a stable platform is formed by using the top-mounted gripper to attach to a rigid object. Opposed to going around the propellers, a direction that could be more beneficial would be a bottom or top-mounted design that is able to cross through the center to the other side but this would require a suitable UAV design. The side-mounted morphology does theoretically also have the ability to manipulate both below, to the side and above the UAV but due to the mass of this manipulator placed far from the center of the UAV this seems practically not achievable as the size of the manipulator has to remain small. The suspended morphology does provide the design freedom to mount an omnidirectional manipulator, but due to the suspended setup, it is still only able to manipulate below the UAV.

The effect of the morphologies on the stability is also compared, this is done from a mechanical point of view. As mentioned previously the distribution of mass, the shifting COM due to manipulator movement and reaction forces are important aspects that influence the stability. With this investigation, it is intended to find a morphology that poses the least disturbances to this stability and will therefore be likely beneficial to use for high-accuracy UAMs. The whole-body manipulator does not possess a manipulator that could influence the stability of the UAV, therefore this morphology is not considered in this comparison.

The different morphologies show solutions or features intended to improve stability. For the side-mounted morphology, this is not the case. This is likely due to the fact that the designs in this morphology do suffer less from the stability issue and therefore no solutions improving on this are invented. This should not be mistaken for a benefit of this morphology. The side-mounted morphology only showed a very small manipulator. As a result, negligible influence on stability is obtained as the weight and movement of the manipulator are small. Once the manipulator would get larger the stability issue would become more and more present. Likely these issues become even worse than for other morphologies as the manipulator is placed far from the COM of the UAV which makes the coupling effects worse due to the longer moment arm. The suspended manipulator morphology exploits the nonrigid connection to make sure no reaction forces can be transmitted. Unfortunately, this approach does not help with improving the positioning accuracy of the manipulator. Once accurate positioning is of interest while using this morphology, the stability issue again arises and is then solved often by creating a platform which is able to cope with disturbances created by the manipulator.

A common design approach which can improve stability is placing heavy components, think of for example actuators, close to the COM of the UAV. This helps decrease the shift of the COM and the reaction forces due to manipulator movement. Next to that some more advanced designs are found, that further improve the stability. Starting with the designs in the center-mounted morphology. This morphology offers a free planar space in which the design can be constructed. In both examples shown, counter masses are placed and can rotate with the manipulator keeping the COM almost stationary requiring only a static or a one DoF balancing solution. In the bottom-mounted morphology, the most advanced balancing solutions are observed. Two approaches are found, first utilising additional DoFs or even whole robotic arms to actively keep the COM stationary. Secondly, balanced mechanisms are used which keep the COM stationary in a purely mechanical fashion. These designs can also remove reaction forces, and therefore do not, or only to a small extent, disturb the stability. Here it is important to mention that this is an accomplishment of the design itself and not necessarily due to the morphology. Other morphologies could also benefit from using such designs, and especially the center-mounted morphology shows great potential.

In [4] safety is acknowledged to be one of the challenges that have to be tackled in new generations of UAMs. Therefore a comparison of the safety among the different morphologies is included. In [16], the design strategy of placing the manipulator far from the UAV in a non-rigid fashion is explained to be safer as the risk of impact between propellers and obstacles is lower but also the non rigid connection avoids the rigid propagation of impact forces to the UAV. Lastly, this approach gives the controller more time to react to the perturbations. The example shows that this is possible for the bottom-mounted morphology, and it is not hard to imagine that similar approaches can be applied to top-mounted UAMs as well as center-mounted ones. The same design features improving safety are found in the suspended morphology, see for instance the design presented in [33]. The suspended morphology is the safest morphology. This morphology inherently places the manipulator far from the UAV in a non rigid fashion. This morphology allows for very large distances between manipulator and UAV, providing even more time to react to disturbances and decreasing the risk of impact with the propellers further. Again, the non rigid connection reduces the transmission of interaction forces, lowering the risk of destabilisation. Both, the side-mounted and whole-body manipulator are considered as the least safe morphologies as the before mentioned features are harder to obtain if it is possible at all.

IV. CONCLUSION

In this study existing UAM designs are categorized based on the manipulator placement, or in this work called the morphology. For each morphology examples found in research are presented and their design features are listed. This categorisation was used to explore the influence of the manipulator placement on the characteristics of a UAM and are discussed per morphology. Three distinctive and relevant features; the workspace, stability and safety are compared among all morphologies. From this, it is found that the center-mounted morphology offers the largest workspace, as this morphology is the only morphology that enables the manipulator to manipulate all around the UAV. The bottom-mounted manipulator morphology showed to be the most stable. This, as the most advanced balancing solutions are found in this morphology. The suspended morphology offers a large distance between the UAV and the manipulator, which keeps the dangerous rotors far away from the manipulator and results in longer reaction times for the controller. Furthermore, the suspended setup does not allow rigid transmission of interaction forces which decreases the risk of destabilisation. Resulting in the suspended manipulator morphology being the safest found in literature.

REFERENCES

[1] R. Murphy and V. Gandudi. How are robots helping in the coronavirus pandemic? [Online]. Available: https://www.weforum.org/agenda/2020/05/robots-coronavirus-crisis

[2] The impact of demographic change in europe. [Online]. Available: https://ec.europa.eu/info/strategy/priorities-2019-2024/new-push-european-democracy/impact-demographic-change-europe_en

[3] F. Ruggiero, V. Lippiello, and A. Ollero, "Aerial manipulation: A literature review," *IEEE Robotics and Automation Letters*, vol. 3, no. 3, pp. 1957–1964, 2018.

[4] A. Ollero, M. Tognon, A. Suarez, D. Lee, and A. Franchi, "Past, present, and future of aerial robotic manipulators," *IEEE Transactions on Robotics*, vol. 38, no. 1, pp. 626–645, 2022.

[5] H. Bonyan Khamseh, F. Janabi-Sharifi, and A. Abdessameud, "Aerial manipulation—a literature survey," *Robotics and Autonomous Systems*, vol. 107, pp. 221–235, 2018. [Online]. Available: https://www.sciencedirect.com/science/article/pii/S0921889017305535

[6] P. E. Pounds and A. Dollar, "Hovering stability of helicopters with elastic constraints," in *Dynamic Systems and Control Conference*, vol. 44182, 2010, pp. 781–788.

[7] K. Kondak, F. Huber, M. Schwarzbach, M. Laiacker, D. Sommer, M. Bejar, and A. Ollero, "Aerial manipulation robot composed of an autonomous helicopter and a 7 degrees of freedom industrial manipulator," in *2014 IEEE International Conference on Robotics and Automation (ICRA)*, 2014, pp. 2107–2112.

[8] N. Imanberdiyev, S. Sood, D. Kircali, and E. Kayacan, "Design, development and experimental validation of a lightweight dual-arm aerial manipulator with a cog balancing mechanism," *Mechatronics*, vol. 82, p. 102719, 2022. [Online]. Available: https://www.sciencedirect.com/science/article/pii/S0957415821001781

[9] Y. Ohnishi, T. Takaki, T. Aoyama, and I. Ishii, "Development of a 4-joint 3-dof robotic arm with anti-reaction force mechanism for a multicopter," in *2017 IEEE/RSJ International Conference on Intelligent Robots and Systems (IROS)*, 2017, pp. 985–991.

[10] K. Bodie, M. Tognon, and R. Siegwart, "Dynamic end effector tracking with an omnidirectional parallel aerial manipulator," *IEEE Robotics and Automation Letters*, vol. 6, no. 4, pp. 8165–8172, 2021.

[11] K. Suryavanshi, "Adapt: A 3 degrees of freedom reconfigurable force balanced parallel manipulator for aerial applications," 2022.

[12] K. Zhang, P. Chermprayong, F. Xiao, D. Tzoumanikas, B. Dams, S. Kay, B. B. Kocer, A. Burns, L. Orr, C. Choi *et al.*, "Aerial additive manufacturing with multiple autonomous robots," *Nature*, vol. 609, no. 7928, pp. 709–717, 2022.

[13] P. Chermprayong, K. Zhang, F. Xiao, and M. Kovac, "An integrated delta manipulator for aerial repair: A new aerial robotic system," *IEEE Robotics & Automation Magazine*, vol. 26, no. 1, pp. 54–66, 2019.

[14] T. W. Danko, K. P. Chaney, and P. Y. Oh, "A parallel manipulator for mobile manipulating uavs," in *2015 IEEE International Conference on Technologies for Practical Robot Applications (TePRA)*, 2015, pp. 1–6.

[15] M. Kamel, K. Alexis, and R. Siegwart, "Design and modeling of dexterous aerial manipulator," in *2016 IEEE/RSJ International Conference on Intelligent Robots and Systems (IROS)*, 2016, pp. 4870–4876.

[16] A. Suarez, A. M. Giordano, K. Kondak, G. Heredia, and A. Ollero, "Flexible link long reach manipulator with lightweight dual arm: Soft-collision detection, reaction, and obstacle localization," in *2018 IEEE International Conference on Soft Robotics (RoboSoft)*, April 2018, pp. 406–411.

[17] G. Nava, Q. Sablé, M. Tognon, D. Pucci, and A. Franchi, "Direct force feedback control and online multi-task optimization for aerial manipulators," *IEEE Robotics and Automation Letters*, vol. 5, no. 2, pp. 331–338, 2020.

[18] M. Beacom, "Synthesis and control of a 3 degrees of freedom inherently dynamically balanced manipulator for an unmanned aerial vehicle," 2021.

[19] P. E. Pounds, D. R. Bersak, and A. M. Dollar, "Stability of small-scale uav helicopters and quadrotors with added payload mass under pid control," *Autonomous Robots*, vol. 33, no. 1, pp. 129–142, 2012.

[20] H.-N. Nguyen, C. Ha, and D. Lee, "Mechanics, control and internal dynamics of quadrotor tool operation," *Automatica*, vol. 61, pp. 289–301, 2015. [Online]. Available: https://www.sciencedirect.com/science/article/pii/S0005109815003416

[21] J. Thomas, G. Loianno, K. Daniilidis, and V. Kumar, "Visual servoing of quadrotors for perching by hanging from cylindrical objects," *IEEE Robotics and Automation Letters*, vol. 1, no. 1, pp. 57–64, 2016.

[22] S. Shimahara, R. Ladig, S. Leewiwatwong, S. Hirai, and K. Shimonomura, "Aerial manipulation for the workspace above the airframe," in *2015 IEEE/RSJ International Conference on Intelligent Robots and Systems (IROS)*, 2015, pp. 1453–1458.

[23] H. Paul, K. Ono, R. Ladig, and K. Shimonomura, "A multirotor platform employing a three-axis vertical articulated robotic arm for aerial manipulation tasks," in *2018 IEEE/ASME International Conference on Advanced Intelligent Mechatronics (AIM)*, 2018, pp. 478–485.

[24] A. Jimenez-Cano, J. Braga, G. Heredia, and A. Ollero, "Aerial manipulator for structure inspection by contact from the underside," in *2015 IEEE/RSJ International Conference on Intelligent Robots and Systems (IROS)*, 2015, pp. 1879–1884.

[25] A. Ivanovic, L. Markovic, M. Car, I. Duvnjak, and M. Orsag, "Towards autonomous bridge inspection: Sensor mounting using aerial manipulators," *Applied Sciences*, vol. 11, no. 18, 2021. [Online]. Available: https://www.mdpi.com/2076-3417/11/18/8279

[26] T. Bartelds, A. Capra, S. Hamaza, S. Stramigioli, and M. Fumagalli, "Compliant aerial manipulators: Toward a new generation of aerial robotic workers," *IEEE Robotics and Automation Letters*, vol. 1, no. 1, pp. 477–483, 2016.

[27] M. Fumagalli, R. Naldi, A. Macchelli, F. Forte, A. Q. Keemink, S. Stramigioli, R. Carloni, and L. Marconi, "Developing an aerial manipulator prototype: Physical interaction with the environment," *IEEE Robotics & Automation Magazine*, vol. 21, no. 3, pp. 41–50, 2014.

[28] M. Fumagalli, S. Stramigioli, and R. Carloni, "Mechatronic design of a robotic manipulator for unmanned aerial vehicles," in *2016 IEEE/RSJ International Conference on Intelligent Robots and Systems (IROS)*, 2016, pp. 4843–4848.

[29] A. Keemink, M. Fumagalli, S. Stramigioli, and R. Carloni, "Mechanical design of a manipulation system for unmanned aerial vehicles," in *2012 IEEE International Conference on Robotics and Automation*, 2012, pp. 3147–3152.

[30] A. Albers, S. Trautmann, T. Howard, T. A. Nguyen, M. Frietsch, and C. Sauter, "Semi-autonomous flying robot for physical interaction with environment," in *2010 IEEE Conference on Robotics, Automation and Mechatronics*, 2010, pp. 441–446.

[31] H. La Vigne, G. Charron, J. Rachiele-Tremblay, D. Rancourt, B. Nyberg, and A. Lussier Desbiens, "Collecting critically endangered cliff plants using a drone-based sampling manipulator," *Scientific Reports*, vol. 12, no. 1, pp. 1–11, 2022.

[32] F. Käslin, T. Baur, P. Meier, P. Koller, N. Buchmann, P. D'Odorico, and W. Eugster, "Novel twig sampling method by unmanned aerial vehicle (uav)," *Frontiers in Forests and Global Change*, vol. 1, p. 2, 2018.

[33] A. Suarez, P. Sanchez-Cuevas, M. Fernandez, M. Perez, G. Heredia, and A. Ollero, "Lightweight and compliant long reach aerial manipulator for inspection operations," in *2018 IEEE/RSJ International Conference on Intelligent Robots and Systems (IROS)*, 2018, pp. 6746–6752.

[34] R. Miyazaki, R. Jiang, H. Paul, Y. Huang, and K. Shimonomura, "Long-reach aerial manipulation employing wire-suspended hand with swing-suppression device," *IEEE Robotics and Automation Letters*, vol. 4, no. 3, pp. 3045–3052, 2019.

[35] Y. S. Sarkisov, M. J. Kim, D. Bicego, D. Tsetserukou, C. Ott, A. Franchi, and K. Kondak, "Development of sam: cable-suspended aerial manipulator," in *2019 International Conference on Robotics and Automation (ICRA)*. IEEE, 2019, pp. 5323–5329.

[36] D. Sanalitro, H. J. Savino, M. Tognon, J. Cortés, and A. Franchi, "Full-pose manipulation control of a cable-suspended load with multiple uavs under uncertainties," *IEEE Robotics and Automation Letters*, vol. 5, no. 2, pp. 2185–2191, 2020.

[37] M. A. Trujillo, J. R. Martínez-de Dios, C. Martín, A. Viguria, and A. Ollero, "Novel aerial manipulator for accurate and robust industrial ndt contact inspection: A new tool for the oil and gas inspection industry," *Sensors*, vol. 19, no. 6, 2019. [Online]. Available: https://www.mdpi.com/1424-8220/19/6/1305

[38] S. Hamaza and M. Kovac, "Omni-drone: on the design of a novel aerial manipulator with omni-directional workspace," in *2020 17th International Conference on Ubiquitous Robots (UR)*, 2020, pp. 153–158.

[39] F. Shi, M. Zhao, M. Murooka, K. Okada, and M. Inaba, "Aerial regrasping: Pivoting with transformable multilink aerial robot," in *2020 IEEE International Conference on Robotics and Automation (ICRA)*, 2020, pp. 200–207.

[40] M. Zhao, T. Anzai, F. Shi, X. Chen, K. Okada, and M. Inaba, "Design, modeling, and control of an aerial robot dragon: A dual-rotor-embedded multilink robot with the ability of multi-degree-of-freedom aerial transformation," *IEEE Robotics and Automation Letters*, vol. 3, no. 2, pp. 1176–1183, 2018.

[41] M. Zhoa, K. Okada, and I. Masayuki, "Versatile articulated aerial robot dragon: Aerial manipulation and grasping by vectorable thrust control," p. 027836492211124. [Online]. Available: http://dx.doi.org/10.1177/02783649221112446

[42] B. Gabrich, D. Saldaña, V. Kumar, and M. Yim, "A flying gripper based on cuboid modular robots," in *2018 IEEE International Conference on Robotics and Automation (ICRA)*, 2018, pp. 7024–7030.

3

Design of an Inherently Fully Dynamically Balanced Flying Manipulator with Omnidirectional Workspace

Design of an Inherently Fully Dynamically Balanced Flying Manipulator with Omnidirectional Workspace

Alexander Bom

***Abstract*—The manipulation accuracy of unmanned aerial manipulators suffers from the dynamic unbalance of the manipulator arm. The movement of the manipulator arm creates disturbances, i.e. reaction forces, reaction moments and a shifting center of mass, affecting the position and attitude of the unmanned aerial vehicle. To address this problem, this paper presents the design of a two degree of freedom inherently fully dynamically balanced manipulator. A new design approach was used by making a manipulator fly in stead of the common approach of mounting a manipulator arm to a drone. This new approach helps to avoid interference with the drone's components, making it possible to achieve an omnidirectional workspace and allow for an inherently balanced design. The kinematics, workspace and balance conditions of the design are presented. The design's workspace is optimised while the mass of the manipulator is minimized with a bilevel optimisation. Finally, the design is validated both by simulation and experiments performed with the built prototype.**

***Index Terms*—Unmanned aerial manipulator, UAV, UAM, Morphology, Bilevel Optimisation, Omnidirectional Aerial Manipulator, Inherent balance.**

I. INTRODUCTION

The field of aerial manipulation combines the mobility of unmanned aerial vehicles (UAVs) with the physical interaction capabilities of manipulators, to create so-called unmanned aerial vehicles (UAMs). To change the position of the manipulator's end-effector, reaction forces and moments are usually exerted on the UAV. Additionally, the movement of the manipulator can cause the distribution of mass within the system to change, leading to a shifting center of mass (COM). Both the reaction forces and shifting COM can affect the position and attitude of the UAV, and even lead to destabilisation. These coupled dynamics between the manipulator and the UAV make it challenging to position the end-effector accurately. In many studies, control approaches are taken to reduce the effects of coupled dynamics on the performance of the UAM, by approaching the control of the UAV and manipulator as a unified system. The computational resources onboard of a UAM limit the complexity of the control model that can be implemented [1], and thereby the performance that can be achieved. The theory of dynamic balance could be of great interest as this has the potential to decouple the dynamics in a purely mechanical fashion, allowing the manipulator to move rapidly in all directions without disturbing the UAV.

A mechanism is said to be force-balanced if the linear momentum is conserved and it is moment-balanced if the angular momentum is conserved. The mechanism is fully dynamically balanced if it is force and moment-balanced. In practice, these two conditions can be formulated more strictly, resulting in the following two conditions [2].

$$\frac{\mathrm{d}\mathbf{r}}{\mathrm{d}t} = 0 \tag{1}$$

$$\frac{\mathrm{d}\mathbf{H}_O}{\mathrm{d}t} = 0 \tag{2}$$

Where $\mathbf{r}$ is the position vector of the combined center of mass of the mechanism's components, and $\mathbf{H}_O$ is the angular momentum about a point O in this case located in the UAV's body fixed frame. If these conditions are satisfied the mechanism will cause no reaction forces and moments to its base due to the mechanism's movement.

There are different approaches to achieve dynamic balance in an existing mechanism, one adds more weight than the other but generally, the added mass and inertia are substantial [3]. The theory of inherent dynamic balance is different, it uses the principles of dynamic balance to design the mechanism instead of balancing it once the kinematics are established. This helps to reduce the weight and inertia of the mechanism as it reduces the need for heavy counterweights and such, while the balance is inherently present in the structure [4]. This makes this subclass of dynamically balanced mechanisms best suited for aerial manipulators, nevertheless, it will remain a fairly new endeavour as weight plays a different role for aerial manipulators than it does for high-speed manipulators, a field where dynamic balance is more commonly used for. The DUAL-V [5] and Super-B [6], are examples of such high-speed balanced manipulators.

Trying to mount a balanced manipulator to a UAV shows not to be the ideal approach. Mostly because the drone's design limits the design freedom left for the manipulator, which makes it especially difficult to use balance masses efficiently. A balanced mechanism usually is constructed of many links therefore interference with the drone is difficult to avoid. The design presented in [7] illustrates this problem, integrating the manipulator and drone design to make the design viable for practical use is recommended in their work.

The placement of a manipulator on a drone influences not only the design freedom of the manipulator but also the workspace it can achieve. The state-of-the-art aerial manipulators can be categorised by the way the manipulator is mounted to the drone, i.e. the morphology of the UAM (unmanned aerial manipulator). By doing this the following morphologies can be found; The most commonly used one is the bottom-mounted morphology. It places the manipulator underneath the UAV. Many different designs using this morphology can be found and range from single degree of freedom (DoF) grippers to many DoF serial or parallel manipulators [8],

[9], [10], [11], [12], [13], [14], [15], [16], [17], [18]. The workspace of the manipulators found in this morphology is limited to the area underneath the propellers. In some cases, the manipulator can also manipulate to the side of the UAM, but their workspace remains below the rotors. How far a manipulator can extend to the side is limited by the shifting COM, as this shift has to be corrected to keep the UAM stable. A very practical remark about this morphology is that often some sort of landing gear is placed underneath the UAV conflicting the workspace of the manipulator. Alternatively, the manipulator can be placed on top of the drone. This forms the second morphology, the top-mounted morphology. A common use for the top mounted morphology is using a single DoF gripper on top of the drone to attach to an object [19], [20], [21]. In [22], [23], [24], manipulators with multiple DoFs are attached to the drone using the top mounted morphology. Similar to the bottom-mounted morphology, the top-mounted morphology's workspace is limited by the propellers. The area is restricted to the area above and possibly includes the area to the side of the UAM. The third morphology, the side-mounted morphology, places the manipulator to the side of the UAV. Examples of side-mounted manipulators are rare. To the author's knowledge, only one example containing a manipulator exists. It places a small delta-like manipulator on the side of a drone [25]. Other side-mounted UAMs do exist, however, these do not possess a manipulator, instead, they have tools mounted to the UAV [26]. As the manipulator is placed on the side of the UAV, already beyond the rotors, it seems easy for the manipulator to manipulate both below, beside and above the UAV. However, examples that can do this are not found in the literature. A likely cause for this is the undesired distribution of mass due to the placement of the manipulator positioned very far from the COM of the UAV.

Furthermore, there is the morphology with suspended manipulators, this morphology distinguishes itself by the non-rigid connection between the UAV and the manipulator, by a rope or rod. This morphology is mostly used once the to-be-manipulated object should remain at a large distance from the propellers either to avoid effects from downwash [27] or to ensure safe operation due to the drone remaining at a distance[28]. More UAM designs using this morphology can be found in [29], [30], [31], [32]. The morphology allows all kinds of manipulators to be used, however, due to the setup the workspace remains limited to the area underneath the drone.

The center mounted morphology places the manipulator in the center and constructs the UAV around it. From the examples found this results in the unique ability to manipulate below, beside and above the UAV. The Aerox manipulator [33], is an example of such a UAM. The Omni-Drone takes it a step further and can manipulate in an omnidirectional circular workspace around the drone [34].

The last morphology distinguishes itself by the use of the UAV as the manipulator, this is also known as whole-body manipulation. In the existing literature, two types are found. The first type uses a UAV which can change its shape, examples are Hydrus [35] and Dragon [36]. The other strategy is to use multiple smaller UAVs as it were the links from which a manipulator is constructed, this is found in [37].

The Omni-Drone, with a center-mounted morphology, [34] is the only UAM found with an omnidirectional workspace achieved solely by the DoFs of the manipulator arm. Having an omnidirectional workspace makes the manipulator more versatile and hence broadening the range of tasks that can be accomplished. Other morphologies are unable to achieve this, as the rotors form a boundary which is hard to breach. Especially because large displacements of the manipulator and therefore of the COM are undesired.

The center-mounted morphology allows to freely design a planar manipulator arm which can be transformed into an aerial manipulator by attaching the UAV's propellers to both sides. This insight led to a new design approach which enables to focus on the design of the manipulator arm. As long as this manipulator arm is planar and allows for the connection of the UAV's propellers to both sides it can be transformed into a flying manipulator. This design approach of making a manipulator fly, is different from the common approach of trying to integrate an manipulator arm and UAV. It avoids interference with the UAVs components making it suited for achieving an omnidirectional workspace as well as a dynamically balanced design. Especially for inherently balanced designs which typically use many links, and therefore could easily interfere with the UAV.

The goal of this paper is to present the design of a two DoF fully inherently balanced manipulator with omnidirectional workspace which can be transformed to a flying manipulator. First, the kinematics and workspace of the manipulator arm are investigated, followed by the balance conditions. These balance conditions are then used in an optimisation process to optimise the workspace of the manipulator within a mass budget. The found optimum is translated to a design of which a prototype has been developed and built. Tests of the design, by experiment and simulation, to verify the balance of the design are shown.

II. KINEMATICS AND WORKSPACE

It was chosen to use two four-bar linkages stacked on top of one another, as shown in [38], for the manipulator's design. It can achieve an omnidirectional workspace while it is fully inherently balanced. A schematic overview of this mechanism along with the parameters to describe the kinematics is presented in Figure 1. Several other concepts derived from inherently balanced mechanisms were considered but were discarded mainly for one of the following reasons. Two DoF inherently force-balanced mechanisms require a counter-inertia to moment balance the system as one of the DoFs is a rotation of the whole mechanism around their COM. Using balanced mechanisms with more DoFs and constraining these such that two remain results in fully inherently balanced mechansisms. Unfortunately, the added constraints limit the workspace heavily and this approach therefore seems not suitable for an omnidirectional manipulator.

The mechanism consists of two four-bar linkages, both in an inverted configuration, meaning the input link and output link are on opposite sides of the base link. The first inverted four-bar linkage consists of links one (P_1P_2), two (P_2P_3) and three

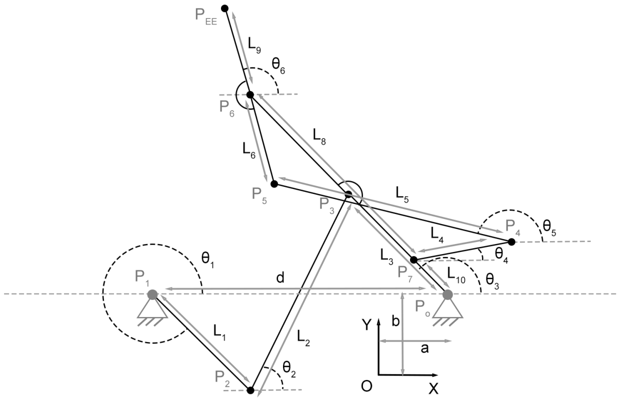

Fig. 1: Schematic representation of the 2-DoF manipulator with base link P_oP_1 and end-effector P_{EE} and relevant parameters establishing its kinematics. Parameter b is defined to clearly indicate the origin's position and remains $b = 0$ throughout this work.

(P_oP_3) and is connected to the base consisting of points P_1 and P_o. The links are connected with revolute joints in points P_o, P_1, P_2 and P_3. Link one is used as the input link, and thus the first DoF, θ_1. The second inverted four-bar consists of links four (P_7P_4), five (P_4P_5) and six (P_5P_6), connected by revolute joints in P_4, P_5, P_6 and P_7, with the last two points forming the base. P_6 and P_7 are positioned on the extended link three (P_oP_6), for clarity this is one rigid link on which the revolute joints P_3 and P_7 are mounted. Link four is used as the input link and forms the second DoF of the mechanism, θ_4. These DoFs control the position of the end-effector P_{EE}, which is located on the tip of the extended link six (P_5P_{EE}). The movement associated with both DoFs of the mechanism is displayed in Figure 2. θ_1 moves the inverted four-bar constructed by links one, two and three (the black lines). The plot shows a displaced configuration and its reference, represented by the dotted line. The second inverted four-bar is mounted on link three, and for that reason follows the displacement caused by θ_1. The second DoF is θ_4, and solely displaces the inverted four-bar consisting of links four, five and six (shown in red).

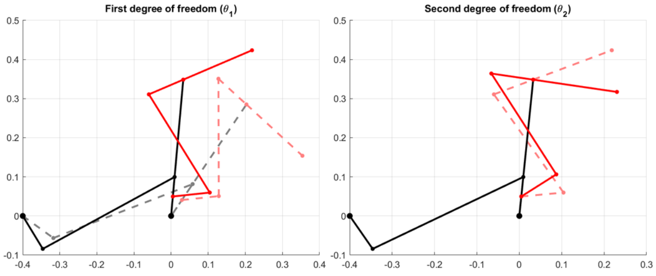

Fig. 2: Kinematics visualized per DoF, the dotted lines represent the initial state and the solid line represents the moved state.

The inverted four-bar mechanism can be configured in two ways. For the manipulator arm this means that four different combinations can be made, each with a different workspace. Figure 3 shows the workspace (in red) corresponding to the configuration displayed by the solid black lines. By combining these workspaces an omnidirectional workspace can be created.

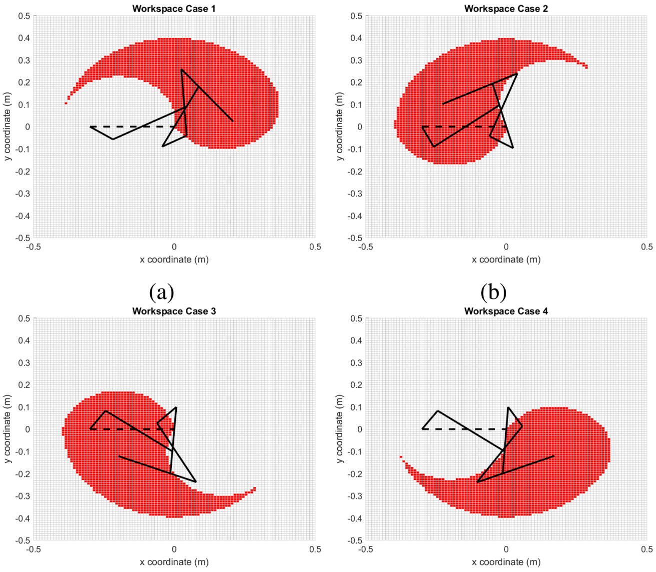

(a) (b)

(c) (d)

Fig. 3: Workspace plot of the four configurations of the manipulator.

III. BALANCE CONDITIONS OF MANIPULATOR ARM

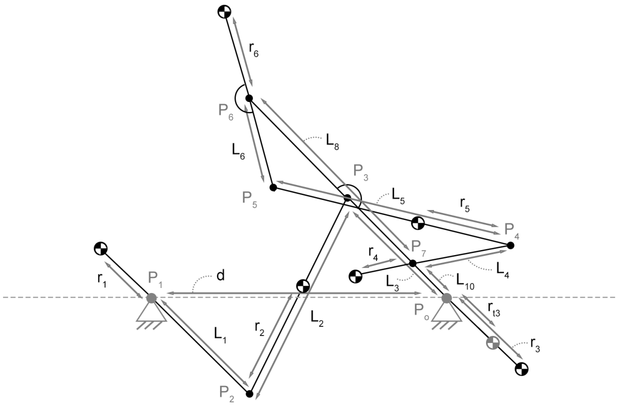

Fig. 4: Relevant parameters used to express the balance conditions of the manipulator arm.

In [38] the balance conditions of a single four-bar mechanism are presented. These equations can be used to write the balance equations of the manipulator arm. In Figure 4 the parameters used in the balance equations are defined. The link lengths of the six links are denoted by L_i. L_{10} and L_8 define the positions of points P_7 and P_6. The length of the base link P_oP_1 is defined by d. Each link has a mass of m_i and an inertia of I_i about the center of mass of the link which is positioned at a distance of r_i. The COM in light grey represents the combined COM of links three, four, five and six positioned on link three at a distance of r_{t3}, with an associated mass of m_{t3} and inertia of I_{t3}. The manipulator is fully balanced if the following conditions are satisfied. Firstly, the link lengths must satisfy:

$$l_4 = l_6 \tag{3}$$

$$l_5 = l_8 \tag{4}$$

$$l_1 = l_3 \tag{5}$$

$$d = l_2 \tag{6}$$

If these are met the mechanism can be force-balanced if the mass om the mechanism is distributed according to the following equations.

$$r_5 = l_5(1 - \frac{m_4 r_4}{l_4 m_5}) \tag{7}$$

$$r_6 = \frac{l_4 m_5 r_5}{m_6 l_5} \tag{8}$$

$$r_2 = l_2(1 - \frac{m_1 r_1}{l_1 m_2}) \tag{9}$$

$$r_{t3} = \frac{l_1 m_2 r_2}{m_{t3} l_2} \tag{10}$$

Lastly the conditions below can be used to moment balance the mechanism.

$$I_5 = m_5(l_5 r_5 - {r_5}^2) - m_4(r_4 l_4 + {r_4}^2) - I_4 \tag{11}$$

$$I_6 = -m_6(l_6 r_6 + {r_6}^2) + m_4(r_4 l_4 + {r_4}^2) + I_4 \tag{12}$$

$$I_2 = m_2(l_2 r_2 - {r_2}^2) - m_1(r_1 l_1 + {r_1}^2) - I_1 \tag{13}$$

$$I_{t3} = -m_{t3}(l_3 r_{t3} + {r_{t3}}^2) + m_1(r_1 l_1 + {r_1}^2) + I_1 \tag{14}$$

With,

$$m_{t3} = m_6 + m_5 + m_4 + m_3 \tag{15}$$

$$\begin{aligned} r_{t3} = & \frac{r_3 m_3 - ((l_{10} + l_8)(m_6 + \frac{r_5}{l_5} m_5))}{m_{t3}} \\ & - \frac{l_{10}(m_4 + m_5(1 - \frac{r_5}{l_5}))}{m_{t3}} \end{aligned} \tag{16}$$

$$\begin{aligned} I_{t3} = & I_3 + (r_3 - r_{t3})^2 m_3 + I_{P7} - {r_c}^2(m_4 + m_5 + m_6) \\ & + (r_c + l_{10} - r_{t3})^2(m_4 + m_5 + m_6) \end{aligned} \tag{17}$$

In which,

$$r_c = \frac{l_8(m_6 + \frac{r_5}{l_5} m_5)}{m_4 + m_5 + m_6} \tag{18}$$

$$\begin{aligned} I_{P7} = & I_4 + I_5 + I_6 + m_4 {r_4}^2 + m_5 {l_4}^2 + m_5 {r_5}^2 \\ & + m_6 {l_8}^2 + m_6 {r_6}^2 \end{aligned} \tag{19}$$

I_{t3} expresses the inertia of the links three, four, five and six combined, evaluated around the combined COM. In the expression the inverted four-bar existing of links four, five and six is treated as a rigid body which is valid as this mechanism is dynamically balanced, the derivation can be found in [39]. I_{P7} expresses the inertia of this body around P_7. The distance between P_7 and the COM of the rigid body is expressed as r_c.

IV. BILEVEL OPTIMISATION OF WORKSPACE AND MASS

Constructing a physical manipulator from the stacked inverted four-bar mechanism requires finding suitable dimensions. The requirements can vary per use case but for this manipulator arm, the workspace and weight are important. This is a difficult task as there are many parameters of which the influence they have on the outcome is hard to fathom. The problem is further complicated by the balance conditions that yield unusable solutions for certain combinations of link lengths. In [39] the need for optimisation is acknowledged but was not performed for the sake of complexity. A method to optimise this problem had to be found.

At first, it was tried to optimise the workspace and minimise the weight in one multi objective optimisation problem. Soon this approach proved to be inefficient, as the workspace had to be evaluated for every new configuration. Meaning that unnecessary computations are performed as many parameters do not influence the workspace. Therefore the optimisation is separated into two optimisation steps, or a so-called bilevel optimisation, solving the problem more efficiently. The main optimisation tries to optimise the workspace of the manipulator and gets a certain mass budget to work with, which is implemented as a constraint. The mass of the mechanism is determined by another optimisation which is embedded in the constraint function and tries to minimise the mass for the set of kinematic parameters that was passed to it. To keep the explanation organised each optimisation will be explained in detail in its subsection.

A. Main optimisation: Workspace

In this work the reachable workspace is considered, this is the set of all end-effector positions that can be reached by some combination of allowable input angles. There are multiple ways of determining the workspace, for the objective function in this optimisation a numerical approach based on discretisation similar to the methods presented in [40], [41] is used. In this optimisation the kinematic parameters as shown in Figure 1 are the decision variables, with corresponding vector $\mathbf{x_m}$. In the optimisation solely the workspace belonging to the configuration as shown in Figure 3a is considered. Switching between configurations is difficult in practice and therefore deemed undesired during operation, which motivates optimising a single configuration.

$$\mathbf{x_m} = \begin{bmatrix} a & d & l_1 & l_4 & l_5 & l_9 & l_{10} \end{bmatrix}^\top \tag{20}$$

To start an area of width w and height h centered around the origin O is defined. This area is divided in n by m boxes and a point in the middle of the boxes is selected to represent it. Specific to the application a desired workspace can be determined. This manipulator aims to have an omnidirectional workspace, therefore a circular area around the origin is selected, which ranges from a radius r till $r+e$. For the points in this area, a series of checks is performed to determine if a point is part of the reachable workspace. If the point is reachable the corresponding area is assumed to be part of the workspace. The number of points that comply with the checks are counted and the output of the objective function is one divided by the number of reachable points. The functioning of the objective function is visualized in Figure 5. The blue dots represent the desired workspace and a box is marked light grey if it is part of the workspace. The checks that are performed are explained in detail in the rest of this section.

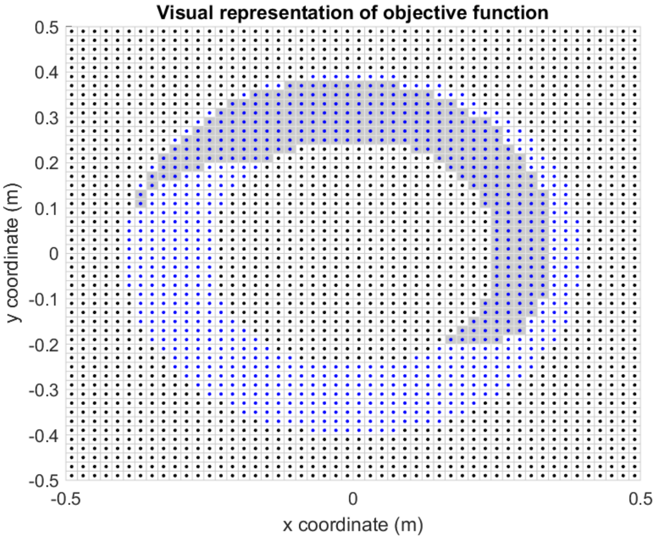

Fig. 5: Visualisation of the objective function used for the main optimisation. The blue dots are the desired points and if they are part of the workspace the corresponding box is marked with a grey color. The number of grey boxes determines the output of the objective function.

First, the inverse kinematics is solved numerically. This process start with determining if the point is reachable, meaning there is a set of joint angles that lead to the desired end-effector position. This is evaluated by accessing, if the three conditions shown in Equation 21, 22 and 23, are invalid. The $distance$ that is used in these expressions refers to the Euclidean distance between P_o and the point which is evaluated.

$$distance > l_8 + l_{10} + l_9 \tag{21}$$

$$distance + l_9 < l_8 + l_{10} \tag{22}$$

$$distance + l_8 + l_{10} < L_9 \tag{23}$$

If the point is within reach, the joint angles are determined by progressing the circle intersection method through the mechanism starting with the intersection of the circles originating in P_{ee} and P_o with radii of respectively L_9 and $L_8 + L_{10}$ from which θ_3 and θ_6 can be calculated.

As stated before, only the configuration shown in 3a will be considered for the manipulator presented in this paper. Therefore the validity of the configuration must be evaluated, which is easily checked based on the calculated angles.

The workspace could be further constrained by for instance physical constraints posed by the construction of the mechanism. As the optimisation is performed based on the schematic mechanism this information is not included. Further, it is known that manipulation near singular configurations is undesired. It is chosen to take this into account by performing a check based on the condition number of the Jacobian matrix. The condition number ranges from one to infinity, where one indicates a perfect conditioned matrix and infinite a singularity. A threshold of 50 is implemented, and the points with a higher condition number are excluded from the workspace. In this evaluation, the two norm condition number is used. The Jacobian matrix is defined as:

$$J = \begin{bmatrix} \frac{\partial x}{\partial \theta_1} & \frac{\partial x}{\partial \theta_4} \\ \frac{\partial y}{\partial \theta_1} & \frac{\partial y}{\partial \theta_4} \end{bmatrix} \tag{24}$$

B. Embedded optimisation: Mass

The embedded optimisation tries to balance the mechanism with the least amount of mass given a set of kinematic parameters. Based on the set of variables shown in Equation 25, the objective function calculates the balance masses and inertia. The parameters are defined in Figure 6. The mass of each link is divided into two parts, the mass of the link itself m_i and an additional balance mass m_{ii}. The placement of the balance mass is denoted by L_{ii}. The mass of the link itself depends on its length, the position of the COM of the link is determined by a_i. The links have an inertia of I_i evaluated around the link's COM. The balance masses have an inertia of I_{ii}.

$$\mathbf{x_e} = \begin{bmatrix} l_{11} \\ l_{22} \\ l_{33} \\ l_{44} \\ l_{55} \\ l_{66} \\ m_{22} \\ m_{55} \\ I_{22} \\ I_{55} \end{bmatrix} \tag{25}$$

The objective function starts with calculating the masses and inertia of the links from which the mechanism is constructed. At first, the same link density was used for all links, the physical design deviated too much and therefore this was changed. To model the manipulator more accurately three

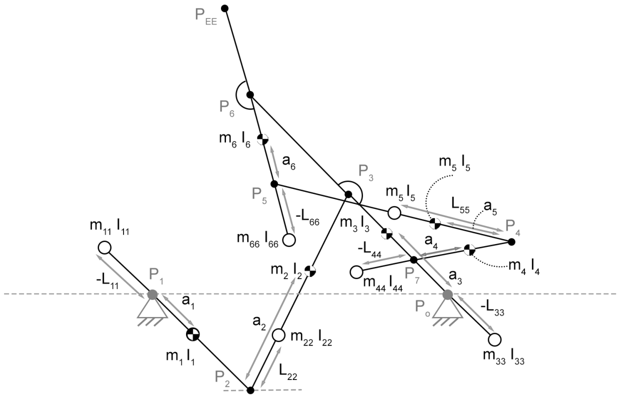

Fig. 6: Overview of the parameters used to describe the (balance) masses, inertia and their positions as used in the embedded mass optimisation.

different link densities were implemented. It is assumed that link six has a density of $\rho_1 = 0.118\,75\,\mathrm{kg\,m^{-1}}$, links two, four and five a density of $\rho_2 = 0.160\,55\,\mathrm{kg\,m^{-1}}$ and links one and three a density of $\rho_3 = 0.2375\,\mathrm{kg\,m^{-1}}$. The mass of a link is then simply calculated by multiplying the density by the length of the link. Care has to be taken in finding the lengths of the links as summing $L_i + L_{ii}$ does not always hold. For instance the cases $L_{11} > L_1$ and $0 < L_{11} < L1$ for which the length of the link is respectively L_{11} and L_1. The inertia of the link is found by:

$$I_i = \frac{1}{12}\frac{m_i^3}{\rho^2} \tag{26}$$

The decision variable vector fully defines links two and five, and from these, the mass and inertia of the other links can be calculated. Previously the balance equations of the stacked inverted four-bar mechanism were presented. These equations consider the general COM of the links and are modified for this optimisation to include the balance masses. The positions of the balance masses are defined by the decision variables therefore the required masses m_{ii} can be calculated with the following equations.

$$m_{44} = \frac{(1 - \frac{r_5}{l_5})l_4 m_{t5} + m_4 a_4}{-l_{44}} \tag{27}$$

$$m_{66} = \frac{\frac{l_4 m_{t5} r_5}{l_5} + l_6 m_6 - a_6 m_6}{l_{66} - l_6} \tag{28}$$

Link three is a special link as this link is part of the inverted four-bar consisting of links one, two and three as well as being the base for the second inverted four-bar consisting of links four, five and six. The mass and inertia of the second inverted four-bar therefore needs to be incorporated in the calculation to find the balance mass and inertia of link three.

$$m_{33} = \frac{-\frac{l_1 * m_{t2} * r_2}{l_2} - l_{10} m_{p7} - a_3 m_3 - (l_{10} + l_8) m_{p6}}{l_{33}} \tag{29}$$

with,

$$m_{p7} = m_{t4} + m_{t5} - \frac{r_5 m_{t5}}{l_5} \tag{30}$$

$$m_{p6} = m_{t6} + \frac{r_5 m_{t5}}{l_5} \tag{31}$$

Lastly, the mass, m_{11}, required to balance link one can be calculated as shown in Equation 32.

$$m_{11} = -\frac{1 - \frac{r_2}{l_2} l_1 m_{t2} - a_1 m_1}{l_{11}} \tag{32}$$

With these equations, all masses can be calculated based on the given decision variables. In these equations the parameter m_{ti} is used to denote the combined mass of the link and its balance mass, except for m_{t3} which represents the total masses of links three, four, five and six together. The same procedure has to be followed to determine the inertia these balance masses should have to moment balance the mechanism as well. Expressing the inertia of the balance masses directly in terms of the other variables results in untidy equations and therefore only the required total inertia of each link will be presented. The inertia of the balance mass can be calculated by subtracting the link's inertia, including the inertia following from the balance mass by the parallel axis theorem, from the required inertia or in other words total inertia the link should have.

$$I_{t4} = m_{t4}\left(\frac{m_{t5}(l_5 r_5 - {r_5}^2) - m_{t5}{k_5}^2}{m_{t4}} - {r_4}^2 - r_4 l_4\right) \tag{33}$$

$$I_{t6} = -m_{t6}(l_6 r_6 + {r_6}^2) + m_{t5}(l_5 r_5 - {r_5}^2) - I_{t5} \tag{34}$$

$$I_{t1} = m_{t1}\left(\frac{m_{t2}(l_2 r_2 - {r_2}^2) - m_{t2}{k_2}^2}{m_{t1}} - {r_1}^2 - r_1 l_1\right); \tag{35}$$

$$I_{t3} = -m_{t3}(l_3 r_3 + {r_3}^2) + m_{t2} * (l_2 r_2 - {r_2}^2) - I_{t2} \tag{36}$$

As the equation presented could result in negative values constraints are added to this optimisation to make sure all masses and inertia are positive. For the inertia, the added constraints are a bit more strict. The inertia values found should correspond to a rod with uniform mass distribution with a size of at least $1cm$ and at max $10cm$ to enforce realistic solutions.

C. results

The optimisation process is used to optimise the dimensions for a realistic scenario. In the optimisation, multiple constants have to be chosen case-specific. In this example, the manipulator is assumed to go on a drone with rotors of approximately 20 cm (8 inch) with 10cm spacing between the rotors. To make sure the manipulator works well with the chosen size, the optimisation can utilize a max of 750 grams for the manipulator. The workspace that is marked as desired for this manipulator ranges from $r = 25$ cm till $r + e = 40$ cm. The 25 cm is chosen such that the manipulator manipulates in

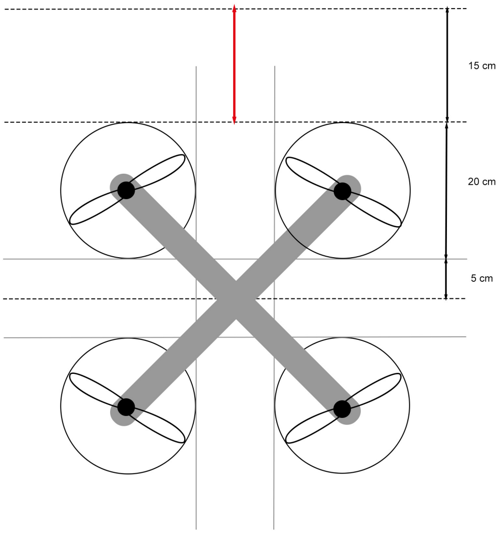

Fig. 7: Picture of the assumed size of the drone, from which the workspace requirements are derived. The red arrow indicates the workspace of the end-effector.

front of the rotors of the drone, this is illustrated in Figure 7. The size e is chosen based on the position error of the drone in real-world applications. In [42] a benchmark value of $6.9cm$ root-mean-square error in the xy direction is reported. If the manipulator can reach this distance in both the positive and negative direction it can correct the error about 70% of the operation. Two times the rms error is rounded to $15cm$ in this case. The parameter a is added as an extra parameter to allow to position P_o in front of the center of the desired workspace. This could reduce the required reach of the manipulator while still being able to manipulate in front of the propellers. This does mean that the points behind the UAV can be marked as desired while they do not reach beyond the rotors. In practice this forms no issue while the workspace of the used configuration is mostly positioned above and in front of P_o.

The area used in the main objective function has a width of $w = 1m$ and height $h = 1m$ divided in $n = 100$ by $m = 100$ boxes. The optimisation is bounded by the bounds presented in Table I.

TABLE I: Boundaries of main optimisation

Variable	Lower bound	Upper bound
a	$0\,\mathrm{m}$	$1\times10^{-1}\,\mathrm{m}$
d	$1\times10^{-1}\,\mathrm{m}$	$6\times10^{-1}\,\mathrm{m}$
l_1	$5\times10^{-2}\,\mathrm{m}$	$1\,\mathrm{m}$
l_4	$1\times10^{-3}\,\mathrm{m}$	$1\,\mathrm{m}$
l_5	$1\times10^{-3}\,\mathrm{m}$	$1\,\mathrm{m}$
l_9	$1\times10^{-3}\,\mathrm{m}$	$1\,\mathrm{m}$
l_{10}	$-1\,\mathrm{m}$	$1\,\mathrm{m}$

The pattern search optimiser from Matlab's global optimisation toolbox is implemented and used with default settings. This optimiser requires a starting point, and as the optimiser finds local minima it is important to choose the starting point wisely. In this case, the starting vector as shown in Equation 37 is used.

$$\mathbf{x_{m0}} = \begin{bmatrix} 0 & 0 & 0.4 & 0.05 & 0.1 & 0.3 & 0.2 & -0.1 \end{bmatrix}^\top \quad (37)$$

The embedded optimisation uses the fmincon optimiser with default settings. The bounds used for this optimisation are displayed in Table VIII. Fmincon also requires a starting vector and as this is an embedded optimisation the start vector that is used depends on the parameters of the main optimisation, see Equation 38.

TABLE II: Boundaries of embedded optimisation

Variable	Lower bound	Upper bound
l_{11}	-2	2
l_{22}	-2	2
l_{33}	-2	2
l_{44}	-2	2
l_{55}	-2	2
l_{66}	-2	2
m_{22}	0	1
m_{55}	0	1
I_{22}	0	1
I_{55}	0	1

$$\mathbf{x_{e0}} = \begin{bmatrix} -0.1 \cdot l_1 \\ 0.5 \cdot l_2 \\ -0.1 \cdot l_3 \\ -0.1 \cdot l_4 \\ 0.5 \cdot l_5 \\ -0.1 \cdot l_6 \\ 0 \\ 0 \\ 0 \\ 0 \end{bmatrix} \quad (38)$$

Running the optimisation yields the decision variable vectors for the main and embedded optimisation as shown in Equation 39. The workspace of the found optimum is able to reach the desired 15 cm in front of the rotors from around -40 degrees to plus 90 degrees, as shown in Figure 8. The corresponding total mass of this optimum is only 708.2 grams. In appendix A, the dynamic balance of the found optimum is verified through a simulation. In appendix B a detailed overview of the parameters defining the optimum is presented.

$$\mathbf{x_m} = \begin{bmatrix} 0.0625\,\mathrm{m} \\ 0.5509\,\mathrm{m} \\ 0.1625\,\mathrm{m} \\ 0.1078\,\mathrm{m} \\ 0.3000\,\mathrm{m} \\ 0.2547\,\mathrm{m} \\ -0.1000\,\mathrm{m} \end{bmatrix}, \mathbf{x_e} = \begin{bmatrix} -4.483\times10^{-1}\,\mathrm{m} \\ 1.399\times10^{-1}\,\mathrm{m} \\ -1.801\times10^{-1}\,\mathrm{m} \\ -1.318\times10^{-1}\,\mathrm{m} \\ 9.479\times10^{-2}\,\mathrm{m} \\ 2.597\times10^{-11}\,\mathrm{m} \\ 1.152\times10^{-1}\,\mathrm{kg} \\ 1.656\times10^{-2}\,\mathrm{kg} \\ 1.343\times10^{-6}\,\mathrm{kg\,m^2} \\ 2.684\times10^{-7}\,\mathrm{kg\,m^2} \end{bmatrix} \quad (39)$$

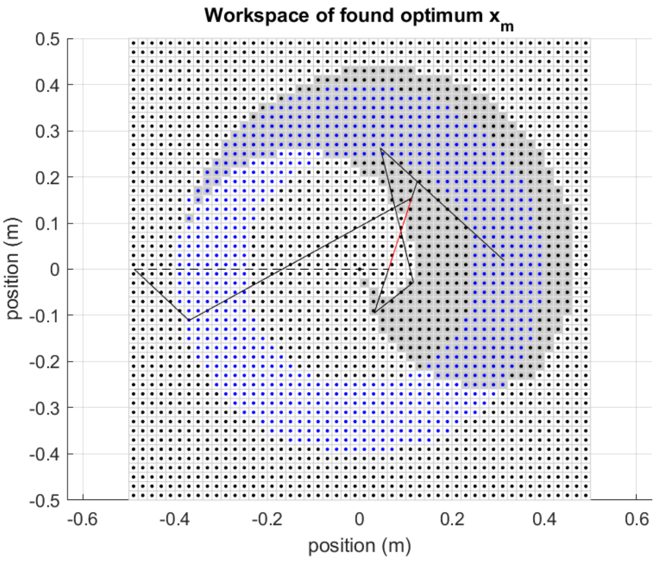

Fig. 8: Plot of the workspace of the manipulator with the optimised variables x_m.

V. DESIGN

The Computer Aided Design (CAD) of the manipulator arm is shown in Figure 9. In the design actuators for the UAV are included to illustrate how the manipulator arm can be transformed to a flying manipulator. The base link of the mechanism forms the frame to which the UAV's components can be mounted. This frame is constructed from 10x10 mm square aluminium profiles connected by a 25 mm round aluminium tube in P_1. Through this tube the cables required to connect the UAV's components, located on both halves, can be passed. A similar connection at P_o was not possible as it would interfere with link five constraining the workspace. The joint at P_o is further complicated as it should allow for free rotation of link three and should also be able to transfer torque to the gear to drive link four (θ_4). To fulfil this on both sides actuators are placed to which shafts are connected, and the gears are screwed to the ends of these shafts. Link three can rotate freely on these shafts due to plastic friction bearings. The section view presented in Figure 9 shows in detail how this is constructed. In the design Dynamixel XL430-W250 actuators are used, these were selected as they were readily available.

The design would allow to use two actuators to drive link one. However only three XL430-W250 actuators were available and therefore link one, θ_1, is actuated by a single actuator. To reduce the load on this single actuator a gear ratio of 2.5 is used. Links one, three and six are made from aluminium tubes with an outer diameter of $15mm$ and a wall thickness of 1 mm. The holes in the tubes relocate the mass of the links helping to position the COM correctly and reduce the inertia of the links. The other links are made from sheet aluminium, which reduces the width of the manipulator arm. The sheet aluminium links again have many cutouts to fulfill the weight and inertia requirements. On links two and five balance masses from sheet steel are attached. The higher density of the material helps to make balance masses with low inertia. The other balance masses, used on links one, three and four are made from aluminium.

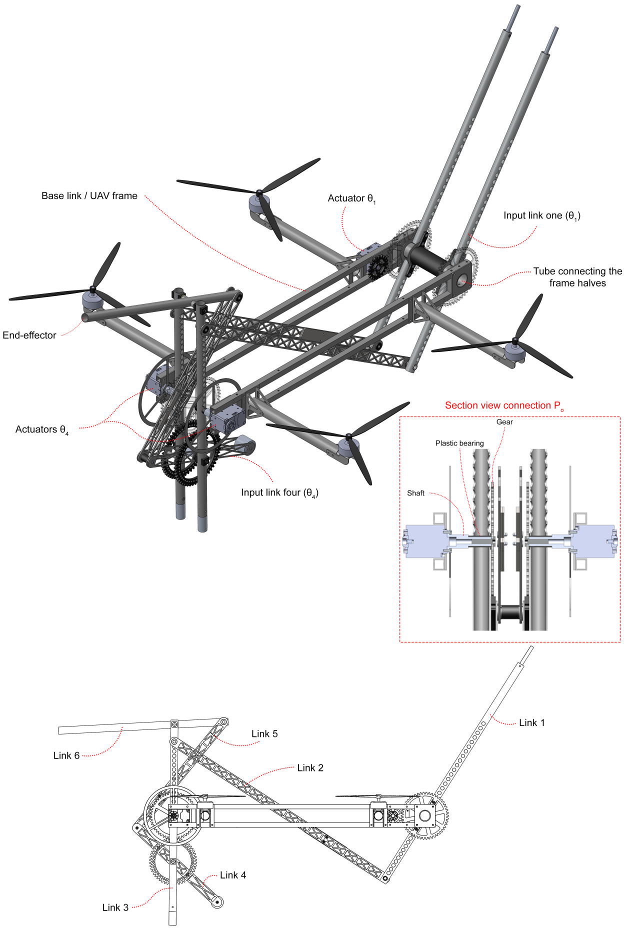

Fig. 9: CAD design of the aerial manipulator.

The parameters found with the optimisation can not directly be used. The optimum must be manually transformed into an actual design. Step by step each link is modelled in CAD software, initially starting with the parameters as found with the optimisation which then have to be tweaked to make sure the balance conditions are met. Link six was used as the starting point of this procedure. The more the link deviates from the optimisation the more cumbersome it is to find a suitable design. Link four is a link that is quite different from the optimisation due to the joint and the gears that are added to the link, see Figure 10. Force balance can be restored, without adding much weight, by redistributing the mass of the link and increasing the distance to the balance mass placed at the end of link four. Moment balance is more difficult, because the inertia of this link is too high, mainly due to the parallel axis theorem components. Increasing the inertia of link six could increase the allowed inertia of link four, but does decrease the allowed inertia of link five at the same time. Resolving the problem in this manner would lead to an increase in the weight of these links which is most undesired as then the problem will propagate to the second inverted four-bar, leading to an even larger increase in weight. Therefore another strategy is used to balance the inertia of link four. The actuators used to move link four rotate in the opposite direction compared to the link due to the geared connection. The actuators can therefore be used to balance the remaining inertia of the link. The inertia of the actuator is measured experimentally and extra inertia in the form of an aluminium disk is added to reach the required inertia for moment balance. The aluminium disks used to increase the inertia associated with the actuator are shown in Figure 11. As the COM mass of the disk is stationary this mass does not have to be incorporated in the mass of link three.

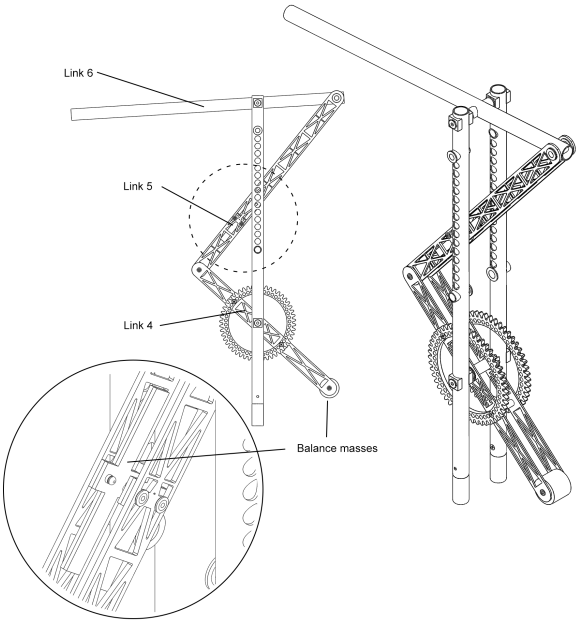

Fig. 10: The inverted four-bar consisting of links four, five and six mounted on link three.

The same procedure has to be followed to balance the second inverted four-bar. The inverted four-bar consisting of links four, five and six has to be taken into account determining the mass, COM and inertia of link three. Due to the geared connection, there is a coupling between the two DoFs. If the actuator connected to link one rotates θ_1 and the other actuator does not rotate, $theta_4$ will rotate double the amount link three rotates. The movement of $theta_4$ results in a reaction moment as the actuator does not move. Therefore the part of the inertia of link four which is balanced by the actuators inertia has to be included twice in the inertia of link three. By mistake, this is performed incorrectly for the prototype's design presented here. Movement of $theta_1$ will therefore not be entirely moment balanced, the resulting reaction moment can be calculated with Equation 40. The parameters of the links of the prototype's design are displayed in Table III. The links of the manipulator arm have a combined weight of 817 gram, including the weights of the gears connected to the actuators and the aluminium disks. The total weight of the manipulator's design, as visible in Figure 11 thus including the actuators and frame, is only 1305 grams.

TABLE III: Mass and Inertia

Variable	Value
a_6	59.5793e-3
m_6	45.1191e-3
I_6	534382.3268e-9
a_5	118.0681e-3
m_5	63.3542e-3
I_5	376511.5991e-9
a_4	47.7414e-3
m_4	86.7634e-3
I_4	645138.9245e-9
a_3	73.2642e-3
m_3	177.3227e-3
I_3	3664737.1768e-9
a_2	191.5927e-3
m_2	203.4946e-3
I_2	2486752.7520e-9
a_1	119.2496e-3
m_1	180.8666e-3
I_1	5537148.4372e-9

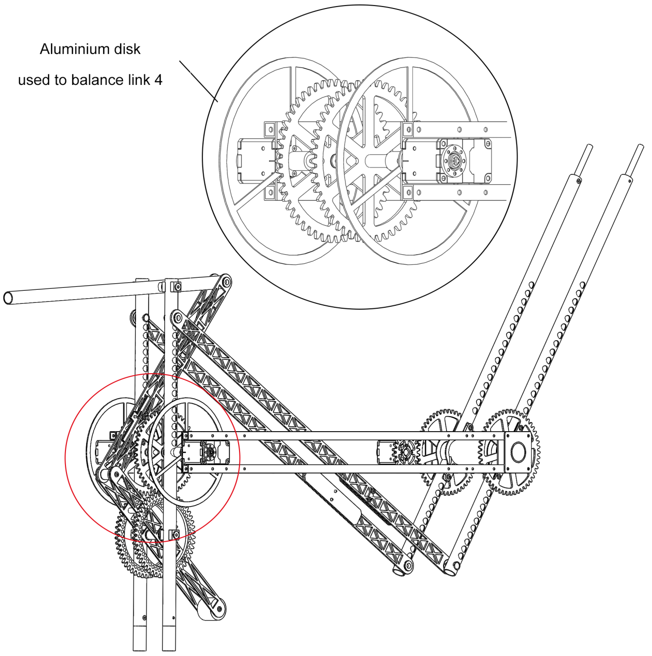

Fig. 11: Detailed view of the gear and aluminium disk attached to the actuators to moment balance link four.

VI. VALIDATION

The goal of this section is to validate that the presented manipulator is dynamically balanced. This will be done by simulation and by physical experiments. To start, the general outline of both approaches will be explained. Then the section is split in two, the first covering the simulation and its results and the second part covers the experiment, which entails explaining the experiment, setup, and showing the measurements.

Both the simulation and the experiment attempt to verify the balance of the manipulator by calculating or measuring the reaction forces resulting from the manipulator's movement. As stated in the previous section, the manipulator's design is by mistake not perfectly balanced. Movement of the inverted four-bar consisting of links one, two and three is expected to result in a reaction moment, the magnitude of this reaction moment is expressed in Equation 40.

$$M_{reaction} \approx 6.102342 \cdot 10^{-4} \cdot \ddot{\theta}_3 \tag{40}$$

To be able to validate this along with validating the other inverted four-bar to be fully balanced, the movement of DoFs θ_1 and θ_4 have to be evaluated separately. Both the simulation and experiment therefore determine the reaction force in X and Y directions as well as the reaction moment around P_o for three cases. Case one actuates θ_1, from 270° to 300° with a constant acceleration of $11.24\ rad/s^2$ and then decelerates at the same rate to $\theta_1 = 330°$. θ_4 is not actuated, but due to the construction of the physical prototype will change due to the motion of the other DoF. θ_4 is calibrated at an angle of 0° once $\theta_3 = 90°$. Case two actuates θ_4 from 0° to 45°, where it accelerates the first half and decelerates the second half of its trajectory with an angular acceleration of $11.24\ rad/s^2$. A third case performs the same trajectory as case one but this time the balance masses mounted on links three and two are removed creating an unbalance in the mechanism.

A. Simulation

The mechanism is modelled in SPACAR, a multibody simulation software package. The links of the inverted four-bar were modelled as planar beams with lengths as shown in Table IV. For each link an additional planar beam was added, this beam has a length corresponding to the distance to the COM of the link. By doing this two nodes are created both positioned at the COM of the link, one describing the position and one the rotation of the link. The inertia and mass parameters of the links are assigned to these nodes. Table III shows the parameters used, except for the inertia of links one, three and four, in the simulation. The variable a_i describes the position of the COM on the link. The inertia shown is the inertia of the respective link around their COM, the inertia of link three is thus the inertia contribution of this link without the inertia of links four, five and six. For links two, five and six the values can directly be found from the CAD model. For links one, three and four this is not the case. The actuators and the geared connections are not modelled and therefore their inertia must be incorporated into these links.

TABLE IV: Link lengths

Variable	Value
l_1	0.1625000
l_2	0.5509375
l_3	0.1625000
l_4	0.1078125
l_5	0.3000000
l_6	0.1078125
d	0.5509375
l_{10}	-0.1000000
l_9	0.2546875

If link one moves, the actuator always moves in the opposite direction with a gear ratio of 2.5. This means that the reduced inertia associated with this movement is simply the inertia of the link minus 2.5 times the inertia of the actuator and the inertia of the gear that is mounted to the actuator. In Table V the inertia of the motor and the gear are presented, along with the actual inertia of link one and the adjusted value as used in the SPACAR simulation.

For links, four and three care must be taken to account for the inertia correctly. Link four uses the counter-rotating actuator to ensure balance by enlarging the inertia associated with the actuator. The inertia of link four can simply be modelled as the inertia of the link subtracting the inertia of the actuator assembly. The actuator assembly consists of the actuator, an aluminium shaft, a drive gear and an aluminium disk to increase the inertia. Note that two actuators are used to drive this link, so the inertia of this assembly has to be subtracted twice to account for both. Once solely the inverted four bar consisting of links four, five and six moves the actuator and the link will always move with a ratio of -1 which makes this modelling choice valid. Once solely θ_1 moves link four moves as well but the actuators associated with θ_4 do not. Therefore the actual inertia of link four must be considered, this can be done by incorporating this inertia in the inertia term of link three. But due to the geared connection to link four the angle θ_4 does not change similar to θ_3 but with $2\dot{\theta}_3 = \dot{\theta}_4$. To compensate for this the inertia that was fictively subtracted from link four has to be added to link three twice. In Table V the inertia values of links three and four are shown, the actual value represents the physical value extracted from the CAD model. The Spacar value represents the value used for the simulation to incorporate the actuator and geared connection as described above.

TABLE V: Adapted values for simulation to include actuators and gears

Variable	Actual Value	Spacar Value
$I_{actuator}$	3.55e-5	-
I_{gear} (θ_1)	735.2874e-9	-
I_1	5537148.4372e-9	5446560.2187e-9
$I_{actuator-assembly}$	1.5256e-4	-
I_4	645138.9245e-9	340021.8417098380e-9
I_3	3664737.1768e-9	4274971.3424e-9

The cases described before were simulated. For case one, θ_4 starts at an angle of 0°. In the physical prototype, the orientation of link four is however coupled to the movement of θ_1 and will therefore move. For the sake of simplicity, the choice is made to keep the angle of θ_4 at zero degrees in the simulation. This is thus different from the physical experiment, however, if the prediction that the inverted four-bar consisting of links four, five and six is fully balanced is correct, the obtained results should not differ. This is for the evident reason that a dynamically balanced mechanism would generate no reaction forces or moments, regardless of the motion it undergoes. The simulation of the second case matches the movement used in the physical experiment. The results are shown in Figure 12, the first row belongs to the first case and the second row to case two. The figures show, from left to right, the reaction force in the x direction, the reaction force in the y direction, the reaction moment evaluated around P_o and the angular accelerations of the links of the moving inverted four-bar. In the first case, the expected result would show a reaction moment and no reaction forces. For the reaction moment, this expectation is easily verified. At first glance, the reaction moment follows the behaviour of the acceleration of $theta_3$, on closer inspection one can see that the magnitude also matches with Equation 40. The reaction forces however do look less convincing, as the order of magnitude of 10^{-6} seems too large to write off to rounding errors in the simulation. Especially considering the second case which shows much lower reaction forces. Therefore an additional check was performed by rerunning the simulation, this time with $m_3 = 178$ grams, which is an increase of less than a gram. The reaction forces are in this case an order of magnitude 10^2 higher. This indicates first of all how sensitive the balance is and more importantly gives confidence in the mechanism to be force balanced. The difference in magnitude between the reaction forces between cases one and two is likely because of the errors building up in link three. The second case shows reaction forces in the order of magnitude 10^{-8} and a reaction moment in the order of 10^{-9}. Considering the sensitivity as mentioned before these results seem to validate the inverted four-bar consisting of links four, five and six to be fully balanced. Case three shows the presence of reaction forces, which is expected as this is an unbalanced case. The magnitude of the obtained forces is still low due to the slow movement of the manipulator.

B. Physical Experiment

The setup used to evaluate the balance of the manufactured prototype is shown in Figure 14. The manipulator is suspended on its side by three wires, see Figure 14 D. This constrains the translation and both rotations out of the plane in which the manipulator manipulates. The in-plane motions are constrained by three FUTEK LSB 200 2lb loadcells, which measure the reaction forces produced by the manipulator. The loadcells were calibrated to measure forces in the range of minus two to plus two Newtons.The data of the loadcells is recorded using Scaime CPJ strain gauge conditioners and an NI USB 6002 DAQ device, located in the bottom right in Figure 14 A. The force is sampled at a rate of 100 Hz, as the NI USB 6002 relies on the clock of the computer to which it's connected the sample rate is not exact. The loadcells are placed such, see Figure 14 A in which the sensors are highlighted by red circles, that they only constrain the manipulator in the direction in which they measure. This is accomplished by 3D-printed flexures which are used to mount the loadcells between the manipulator and the base, see Figure 14 B and C. The reaction forces are measured for the cases as described and for an unbalanced case. The motion of the manipulator is controlled by an Arduino, using a dynamixel shield which can be seen mounted to the side of the frame of the manipulator. With this setup, the reaction forces are measured for the three cases as previously described. The obtained reaction forces are visualised in Figure 13.

Looking at the obtained data, the most obvious observation is the oscillation that is present in the data. The oscillation has a frequency of around 15 Hz and is likely an eigenfrequency of the measurement setup or the manipulator itself. This low stiffness of the setup or manipulator makes it difficult to accurately measure the reaction forces. In an attempt to remove the oscillation from the data, a moving average filter with a window of 20 data points is used and plotted in orange in the figures. In the measurements, the presented time is the actual time from the recording. The starting point, where the manipulator started moving, is visible as the amplitude got larger. In the balanced measurements, the oscillations seem to remain centred around zero during movement. The amplitude of the peaks is much higher than expected but could be caused by the imbalance introduced by manufacturing errors. Especially play in the mechanism can cause high peaks, which is likely the cause for, for instance, the peak in Figure 13 i which is present at around $t = 8$. Here the play in geared connection caused the mechanism to stop abruptly as the actuator stopped moving and the mechanism therefore bumped into it. The masses of the links of the manufactured prototype are shown in Table VI. However, the imbalance would be expected to produce a reaction force which follows a profile similar to the ones present in the simulated results. The small forces which change rapidly in combination with the low stiffness and relatively high inertia have likely resulted in the profile not showing up in the measurements. The measurement is not accurate enough to conclude anything about the moment balance in both cases. The amplitude differs for both balanced cases, which could be explained by the fact that in the first case, the total mass of the moving parts is much higher than in the second case.

The imbalanced case unfortunately does not clearly show reaction forces either. The data seems to show somewhat more of a trend in the oscillation, which is also illustrated by the smoothed data. However, even the smoothed data should not be compared to the simulations as these likely do not accurately capture the fast-changing forces. The fact that there is more of a trend in these plots could be seen as an indicator of higher reaction forces and moments being present. The amplitude of the peaks is not substantially higher in the unbalanced case. Again the imbalance is created by removing some counter masses which results in less mass moving, which could be the cause of this.

Finally, the experimental results are not accurate enough to draw any conclusions about the balance quality of the prototype. However, they show no large reaction forces being present as these would have shown up in the measurements. Combined with the simulated results, it is likely that the design is balanced correctly. To accurately measure the reaction force a better setup is required, some recommendations for improvements are shared in the discussion.

TABLE VI: Link masses prototype

Variable	Value (grams)
m_{link1}	188.2
m_{link2}	205.4
m_{link3}	176.6
m_{link4}	87.8
m_{link5}	59.2
m_{link6}	46.2

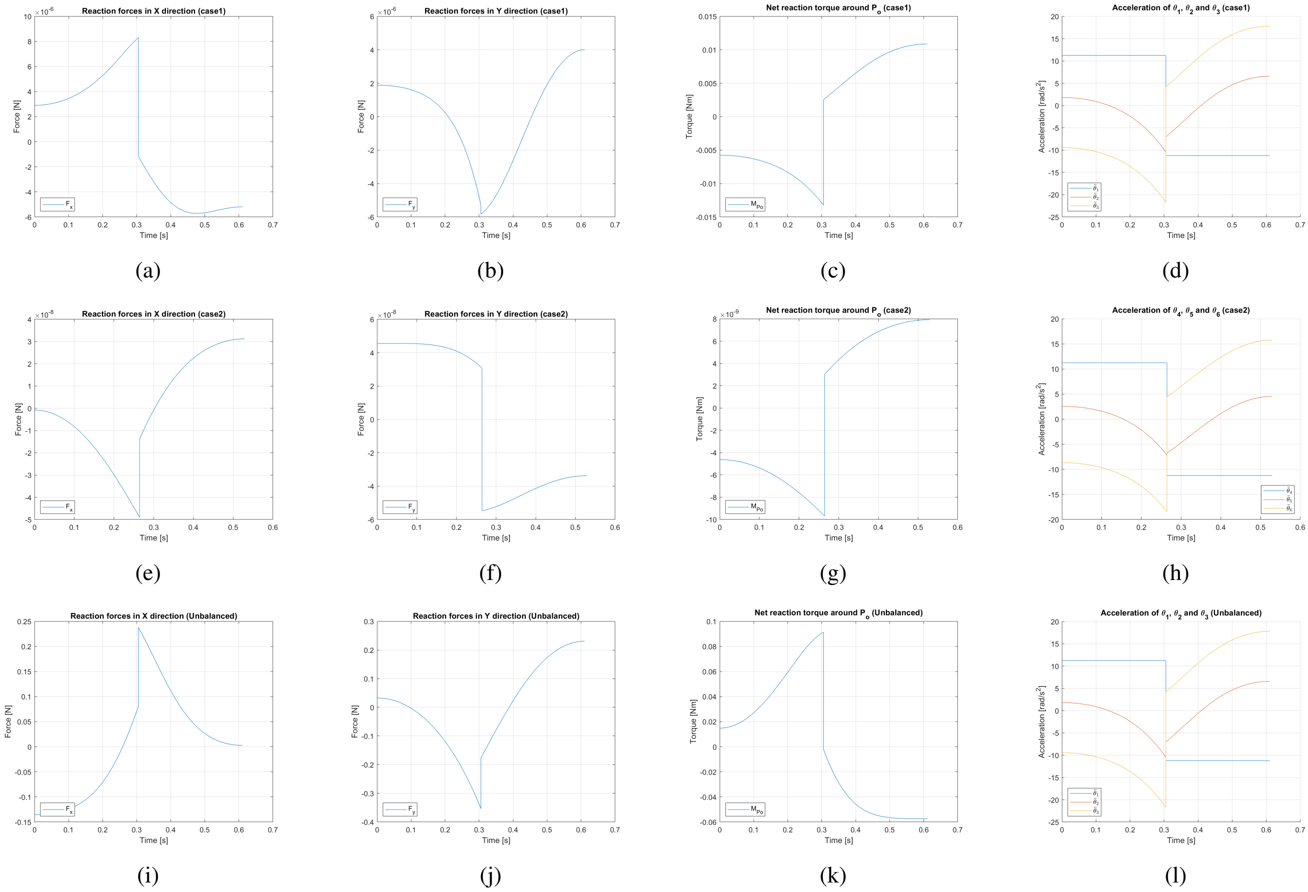

(a) (b) (c) (d)

(e) (f) (g) (h)

(i) (j) (k) (l)

Fig. 12: Simulation results.

VII. Discussion

The objective of designing a two DoF fully balanced omnidirectional manipulator has been pursued. However, the built prototype fell short of fully demonstrating these capabilities. Firstly, perfect moment balance was not obtained, due to a miscalculation, which can be easily resolved. Secondly, the prototype is not able to transition between configurations of the inverted four-bar on its own, hindering its ability to manipulate underneath the UAV.

Should the design successfully incorporate configuration switching, a reevaluation of the objective function used in the optimisation process is required. Optimising a singular configuration may not necessarily yield the optimal manipulator. Therefore, consideration should be given to incorporating other configurations into the objective function. However, it is crucial to acknowledge that switching between configurations during tasks may need to be avoided. Undesirable situations could arise where the manipulator ends up in a non-inverted configuration, altering kinematics and disrupting moment balance. Therefore leaving optimising the workspace of a single configuration to be the best option.

In addition to refining the objective function, enhancements to the optimisation process can be made. The current pattern search optimiser searches for local optima, which is therefore sensitive to the starting point. Implementing a global optimisation method may yield better results. Moreover, the existing bilevel approach utilizes a fixed weight constraint. Introducing a method capable of balancing weight and workspace considerations could be advantageous, especially when pursuing lighter designs at the expense of a slight reduction in workspace. These improvements may intensify computational efforts, warranting careful consideration of the associated benefits.

Finally, increasing the accuracy of the manipulator model used in optimisation, for instance by including the drive gears, helps to make better designs. Enriching this model with more components facilitates a smoother translation of the optimum to a physical design, thereby keeping the design closer to the identified optimum from which the overall performance benefits.

The choice of using the double inverted four-bar mechanism is grounded in its inherent balance properties, particularly its moment-balancing capabilities. This inherent balance is believed to help save weight. Despite this, a comprehensive performance evaluation is recommended, including a comparison with alternative balancing methods.

Evaluating the balance performance of the prototype turned out to be difficult as the reaction forces were low compared to the mass of the mechanism. A stiffer setup could help, but a large source of compliance, namely the loadcells can not be removed. Therefore a different approach is recommended. Instead of measuring the reaction forces of the total mechanism,

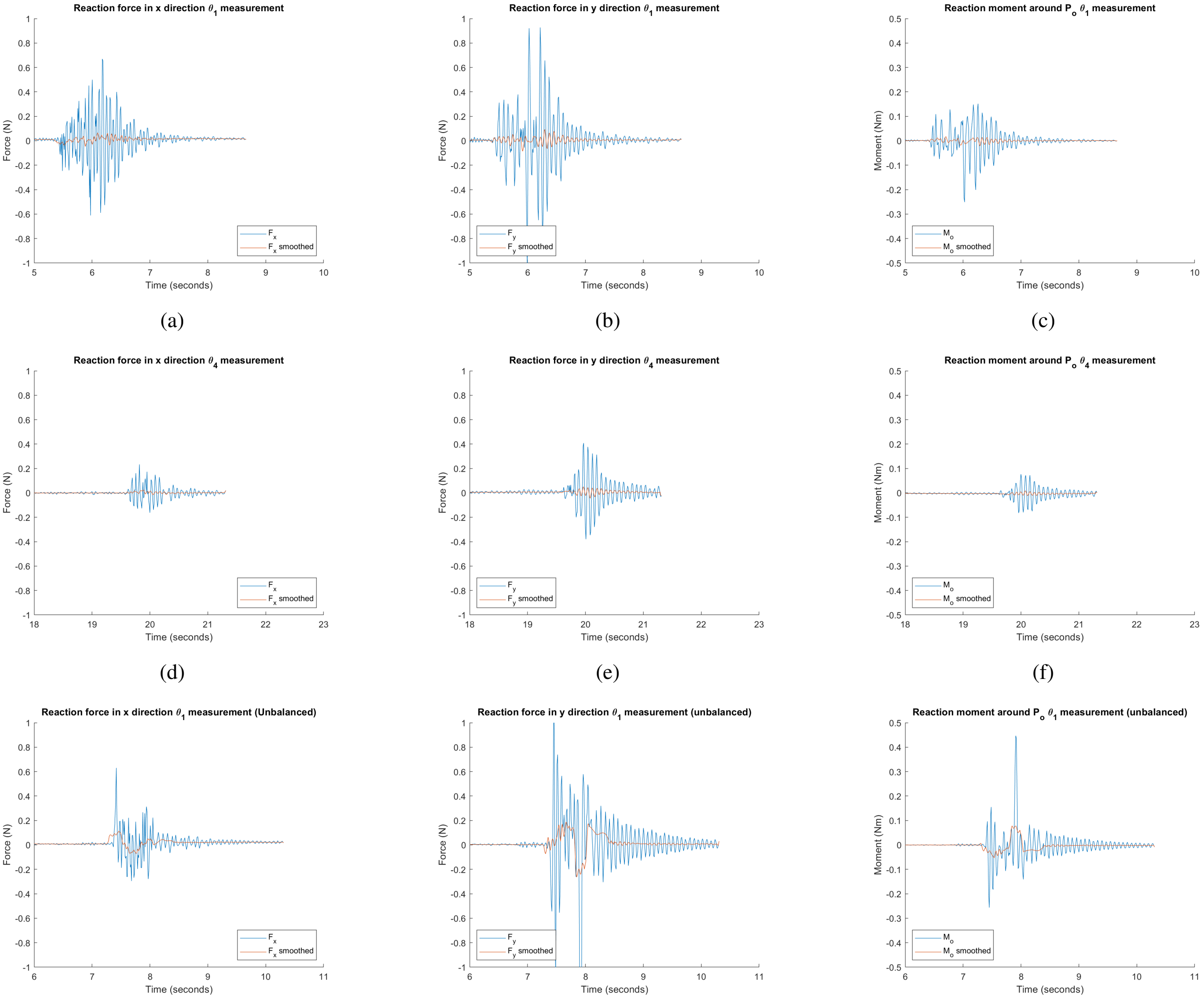

(a) (b) (c)

(d) (e) (f)

(g) (h) (i)

Fig. 13: Simulation results.

it could help if the internal forces were measured. This could be accomplished by removing the frame and constraining the points P_o and P_1 with loadcells. Even for a perfectly balanced case, substantial forces are required to keep these points stationary. The larger forces are likely better measurable and could allow for measurements where the manipulator's movement is slower which reduces the demand for a stiff setup.

In the design of the presented manipulator, no end-effector mass was included, for real-world applications, this is however necessary. This should be kept at a minimum as any extra weight placed on link six will end up in multiple in the manipulator's weight. The embedded mass optimisation is adapted and rerun to determine how the mechanism would change if a payload of 20 grams is added while using the same kinematic parameters. In this case, the mass of the mechanism increases from 708 to 1061 grams. The payload is balanced by increasing the balance mass and changing their positions, in Table VII the balance masses and their positions are shown. No balance masses are used on links one and six but these links show are large change in length. However, this is not necessarily the optimal way of including a payload. For instance, if the length of L_9 is reduced by $5\,\mathrm{cm}$ the total mass of the mechanism can be reduced to $904\,\mathrm{g}$, although this comes at the cost of a smaller workspace. This emphasizes the aforementioned recommendation of formulating the optimisation as a multiobjective problem.

VIII. CONCLUSION

This paper presents the design of an inherently fully dynamically balanced manipulator arm with an omnidirectional workspace, capable of being used as a flying manipulator. The novel design approach of enabling the manipulator to fly circumvents interference between the manipulator arm and UAV, facilitating an inherently balanced design with an omnidirectional workspace. A prototype of the manipulator

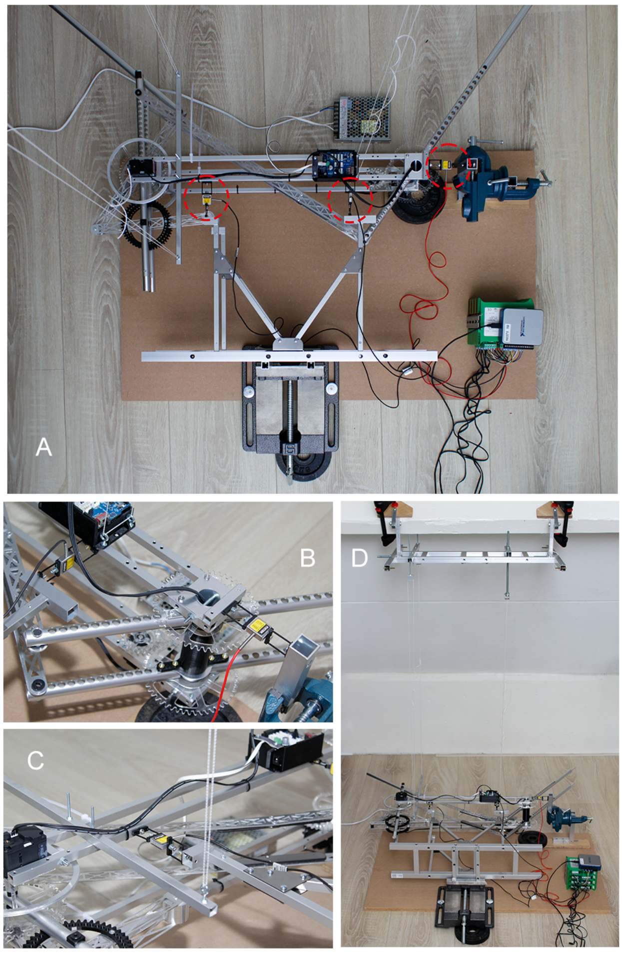

Fig. 14: Caption

TABLE VII: Link masses prototype

Variable	0 grams	20 grams	20 grams (L_9 shortened)
m_{11}	0 g	0 g	0 g
m_{22}	115 g	239 g	186 g
m_{33}	96 g	160 g	141 g
m_{44}	25 g	37 g	22 g
m_{55}	17 g	104 g	54 g
m_{66}	0 g	0 g	0 g
l_{11}	−448 mm	−559 mm	516 mm
l_{22}	140 mm	168 mm	158 mm
l_{33}	−180 mm	−185 mm	−183 mm
l_{44}	−132 mm	−197 mm	−191 mm
l_{55}	95 mm	115 mm	119 mm
l_{66}	0 mm	−76 mm	−59 mm
m_{tot}	708 g	1061 g	904 g

arm was designed and built. The design's balance is verified by simulation and physical experiment. A bilevel optimisation method was shown, which is used to optimise the workspace of the manipulator, within a mass budget. This optimisation resulted in the manipulator having a workspace of at least 15 cm in width within a range of -40 to plus 90 degrees, using a single configuration of the manipulator arm. The inherently balanced design combined with the mass optimisation resulted in the manipulator arm having a mass of 1305 grams.

APPENDIX A
VALIDATING BALANCE OF FOUND OPTIMUM BY DYNAMIC MULTIBODY SIMULATION USING SPACAR

To validate that the found optimum is indeed balanced a dynamic multi-body simulation is performed using SPACAR. The simulation starts in the position $\theta_1 = -1$ and $\theta_4 = 0$, and moves during a time frame of 1 second with an angular acceleration of $1\frac{rad}{s^2}$ for both DoFs. The initial configuration and final configuration are plotted in Figure 15. The blue dots on the links display either the joint positions or the position of the COM of each link.

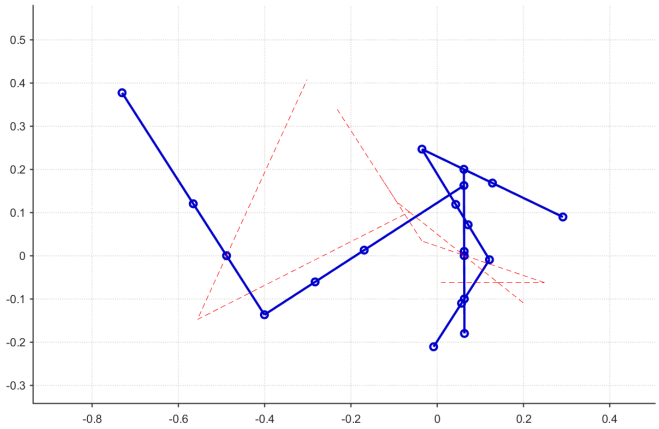

Fig. 15: Plot of the mechanism as implemented in SPACAR. The dashed red line shows the initial position and the blue line shows the mechanism in the final position of the simulation.

Although it would be expected that the reaction forces would completely vanish and only numerical noise would show up in the plots this is not the case. Luckily, the plots show that results are not far from these results as the obtained forces and moment are not much larger than the machine precision. The remaining forces are likely caused by rounding errors that are present in the calculated balance masses.

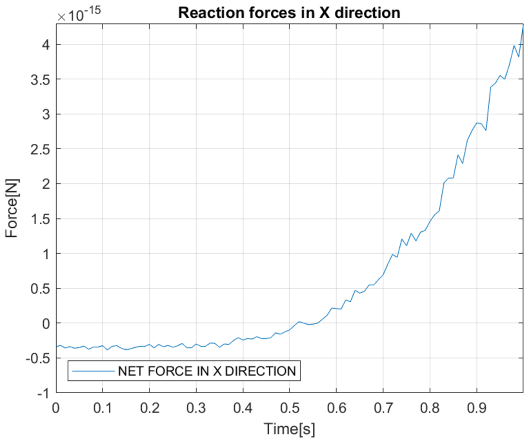

Fig. 16: Plot of the reaction forces in the X direction measured in the origin.

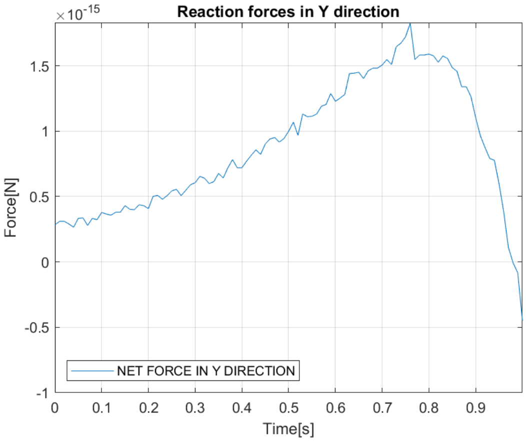

Fig. 17: Plot of the reaction forces in the Y direction measured in the origin.

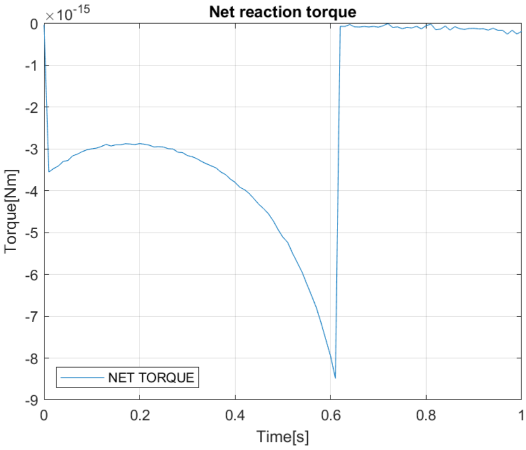

Fig. 18: Plot of the reaction torque produced by the mechanism evaluated around P_1.

APPENDIX B
DETAILED OVERVIEW OF PARAMETERS FOUND OPTIMUM

TABLE VIII: Masses and their positions of optimum

Variable	Value
l_1	$0.1625\,\mathrm{m}$
l_2	$0.5509\,\mathrm{m}$
l_3	$0.1625\,\mathrm{m}$
l_4	$0.1078\,\mathrm{m}$
l_5	$0.3000\,\mathrm{m}$
l_6	$0.1078\,\mathrm{m}$
d	$0.5509\,\mathrm{m}$
l_{10}	$-0.1000\,\mathrm{m}$
l_9	$0.2547\,\mathrm{m}$
l_{11}	$-4.483 \times 10^{-1}\,\mathrm{m}$
l_{22}	$1.399 \times 10^{-1}\,\mathrm{m}$
l_{33}	$-1.801 \times 10^{-1}\,\mathrm{m}$
l_{44}	$-1.318 \times 10^{-1}\,\mathrm{m}$
l_{55}	$9.479 \times 10^{-2}\,\mathrm{m}$
l_{66}	$2.597 \times 10^{-11}\,\mathrm{m}$
m_1	$0.1451\,\mathrm{kg}$
m_2	$0.088\,45\,\mathrm{kg}$
m_3	$0.090\,28\,\mathrm{kg}$
m_4	$0.038\,47\,\mathrm{kg}$
m_5	$0.048\,17\,\mathrm{kg}$
m_6	$0.043\,05\,\mathrm{kg}$
m_{11}	$9.4258 \times 10^{-4}\,\mathrm{kg}$
m_{22}	$0.1152\,\mathrm{kg}$
m_{33}	$0.096\,49\,\mathrm{kg}$
m_{44}	$0.025\,46\,\mathrm{kg}$
m_{55}	$0.016\,56\,\mathrm{kg}$
m_{66}	$6.2157 \times 10^{-6}\,\mathrm{kg}$
I_1	$0.004\,510\,\mathrm{kg\,m^2}$
I_2	$0.002\,237\,\mathrm{kg\,m^2}$
I_3	$0.001\,087\,\mathrm{kg\,m^2}$
I_4	$1.8409 \times 10^{-4}\,\mathrm{kg\,m^2}$
I_5	$3.6124 \times 10^{-4}\,\mathrm{kg\,m^2}$
I_6	$4.7139 \times 10^{-4}\,\mathrm{kg\,m^2}$
I_{11}	$4.9993 \times 10^{-7}\,\mathrm{kg\,m^2}$
I_{22}	$1.3428 \times 10^{-6}\,\mathrm{kg\,m^2}$
I_{33}	$1.0112 \times 10^{-6}\,\mathrm{kg\,m^2}$
I_{44}	$7.6158 \times 10^{-7}\,\mathrm{kg\,m^2}$
I_{55}	$2.6836 \times 10^{-7}\,\mathrm{kg\,m^2}$
I_{66}	$2.5479 \times 10^{-9}\,\mathrm{kg\,m^2}$
a_1	$-0.1429\,\mathrm{m}$
a_2	$0.2755\,\mathrm{m}$
a_3	$0.009\,943\,\mathrm{m}$
a_4	$-0.012\,00\,\mathrm{m}$
a_5	$0.1500\,\mathrm{m}$
a_6	$0.1813\,\mathrm{m}$

REFERENCES

[1] H. Bonyan Khamseh, F. Janabi-Sharifi, and A. Abdessameud, “Aerial manipulation—a literature survey,” *Robotics and Autonomous Systems*, vol. 107, pp. 221–235, 2018. [Online]. Available: https://www.sciencedirect.com/science/article/pii/S0921889017305535

[2] J. Herder and C. Gosselin, “A counter-rotary counterweight (crcw) for light-weight dynamic balancing,” vol. 2, 09 2004.

[3] V. van der Wijk, J. Herder, and B. Demeulenaere, “Comparison of various dynamic balancing principles regarding additional mass and additional inertia,” *Journal of Mechanisms and Robotics*, vol. 1, p. 041006, 11 2009.

[4] V. van der Wijk, “Methodology for analysis and synthesis of inherently force and moment-balanced mechanisms,” Ph.D. dissertation, University of Twente, Netherlands, Apr. 2014.

[5] V. van der Wijk, S. Krut, F. Pierrot, and J. L. Herder, “Design and experimental evaluation of a dynamically balanced redundant planar 4-rrr parallel manipulator,” *The International Journal of Robotics Research*, vol. 32, no. 6, pp. 744–759, 2013. [Online]. Available: https://doi.org/10.1177/0278364913484183

[6] D. Boere, “The constant inertia mechanism and its use in a high-speed 2-dof inherently dynamically balanced parallel manipulator,” 2022.

[7] A. B. Clark, N. Baron, L. Orr, M. Kovac, and N. Rojas, “On a balanced delta robot for precise aerial manipulation: Implementation, testing, and lessons for future designs,” in *2022 IEEE/RSJ International Conference on Intelligent Robots and Systems (IROS)*, 2022, pp. 7359–7366.

[8] P. E. Pounds and A. Dollar, “Hovering stability of helicopters with elastic constraints,” in *Dynamic Systems and Control Conference*, vol. 44182, 2010, pp. 781–788.

[9] M. Kamel, K. Alexis, and R. Siegwart, “Design and modeling of dexterous aerial manipulator,” in *2016 IEEE/RSJ International Conference on Intelligent Robots and Systems (IROS)*, 2016, pp. 4870–4876.

[10] N. Imanberdiyev, S. Sood, D. Kircali, and E. Kayacan, “Design, development and experimental validation of a lightweight dual-arm aerial manipulator with a cog balancing mechanism,” *Mechatronics*, vol. 82, p. 102719, 2022. [Online]. Available: https://www.sciencedirect.com/science/article/pii/S0957415821001781

[11] Y. Ohnishi, T. Takaki, T. Aoyama, and I. Ishii, “Development of a 4-joint 3-dof robotic arm with anti-reaction force mechanism for a multicopter,” in *2017 IEEE/RSJ International Conference on Intelligent Robots and Systems (IROS)*, 2017, pp. 985–991.

[12] K. Kondak, F. Huber, M. Schwarzbach, M. Laiacker, D. Sommer, M. Bejar, and A. Ollero, “Aerial manipulation robot composed of an autonomous helicopter and a 7 degrees of freedom industrial manipulator,” in *2014 IEEE International Conference on Robotics and Automation (ICRA)*, 2014, pp. 2107–2112.

[13] A. Suarez, A. M. Giordano, K. Kondak, G. Heredia, and A. Ollero, “Flexible link long reach manipulator with lightweight dual arm: Soft-collision detection, reaction, and obstacle localization,” in *2018 IEEE International Conference on Soft Robotics (RoboSoft)*, April 2018, pp. 406–411.

[14] G. Nava, Q. Sablé, M. Tognon, D. Pucci, and A. Franchi, “Direct force feedback control and online multi-task optimization for aerial manipulators,” *IEEE Robotics and Automation Letters*, vol. 5, no. 2, pp. 331–338, 2020.

[15] P. Chermprayong, K. Zhang, F. Xiao, and M. Kovac, “An integrated delta manipulator for aerial repair: A new aerial robotic system,” *IEEE Robotics & Automation Magazine*, vol. 26, no. 1, pp. 54–66, 2019.

[16] K. Bodie, M. Tognon, and R. Siegwart, “Dynamic end effector tracking with an omnidirectional parallel aerial manipulator,” *IEEE Robotics and Automation Letters*, vol. 6, no. 4, pp. 8165–8172, 2021.

[17] K. Zhang, P. Chermprayong, F. Xiao, D. Tzoumanikas, B. Dams, S. Kay, B. B. Kocer, A. Burns, L. Orr, C. Choi *et al.*, “Aerial additive manufacturing with multiple autonomous robots,” *Nature*, vol. 609, no. 7928, pp. 709–717, 2022.

[18] T. W. Danko, K. P. Chaney, and P. Y. Oh, “A parallel manipulator for mobile manipulating uavs,” in *2015 IEEE International Conference on Technologies for Practical Robot Applications (TePRA)*, 2015, pp. 1–6.

[19] J. Thomas, G. Loianno, K. Daniilidis, and V. Kumar, “Visual servoing of quadrotors for perching by hanging from cylindrical objects,” *IEEE Robotics and Automation Letters*, vol. 1, no. 1, pp. 57–64, 2016.

[20] H. Paul, K. Ono, R. Ladig, and K. Shimonomura, “A multirotor platform employing a three-axis vertical articulated robotic arm for aerial manipulation tasks,” in *2018 IEEE/ASME International Conference on Advanced Intelligent Mechatronics (AIM)*, 2018, pp. 478–485.

[21] S. Shimahara, R. Ladig, S. Leewiwatwong, S. Hirai, and K. Shimonomura, “Aerial manipulation for the workspace above the airframe,” in *2015 IEEE/RSJ International Conference on Intelligent Robots and Systems (IROS)*, 2015, pp. 1453–1458.

[22] A. Ivanovic, L. Markovic, M. Car, I. Duvnjak, and M. Orsag, “Towards autonomous bridge inspection: Sensor mounting using aerial manipulators,” *Applied Sciences*, vol. 11, no. 18, 2021. [Online]. Available: https://www.mdpi.com/2076-3417/11/18/8279

[23] A. Jimenez-Cano, J. Braga, G. Heredia, and A. Ollero, “Aerial manipulator for structure inspection by contact from the underside,” in *2015 IEEE/RSJ International Conference on Intelligent Robots and Systems (IROS)*, 2015, pp. 1879–1884.

[24] T. Bartelds, A. Capra, S. Hamaza, S. Stramigioli, and M. Fumagalli, “Compliant aerial manipulators: Toward a new generation of aerial robotic workers,” *IEEE Robotics and Automation Letters*, vol. 1, no. 1, pp. 477–483, 2016.

[25] A. Keemink, M. Fumagalli, S. Stramigioli, and R. Carloni, “Mechanical design of a manipulation system for unmanned aerial vehicles,” in *2012 IEEE International Conference on Robotics and Automation*, 2012, pp. 3147–3152.

[26] A. Albers, S. Trautmann, T. Howard, T. A. Nguyen, M. Frietsch, and C. Sauter, “Semi-autonomous flying robot for physical interaction with environment,” in *2010 IEEE Conference on Robotics, Automation and Mechatronics*, 2010, pp. 441–446.

[27] H. La Vigne, G. Charron, J. Rachiele-Tremblay, D. Rancourt, B. Nyberg, and A. Lussier Desbiens, “Collecting critically endangered cliff plants using a drone-based sampling manipulator,” *Scientific Reports*, vol. 12, no. 1, pp. 1–11, 2022.

[28] A. Suarez, P. Sanchez-Cuevas, M. Fernandez, M. Perez, G. Heredia, and A. Ollero, “Lightweight and compliant long reach aerial manipulator for inspection operations,” in *2018 IEEE/RSJ International Conference on Intelligent Robots and Systems (IROS)*, 2018, pp. 6746–6752.

[29] F. Käslin, T. Baur, P. Meier, P. Koller, N. Buchmann, P. D’Odorico, and W. Eugster, “Novel twig sampling method by unmanned aerial vehicle (uav),” *Frontiers in Forests and Global Change*, vol. 1, p. 2, 2018.

[30] Y. S. Sarkisov, M. J. Kim, D. Bicego, D. Tsetserukou, C. Ott, A. Franchi, and K. Kondak, “Development of sam: cable-suspended aerial manipulator,” in *2019 International Conference on Robotics and Automation (ICRA)*. IEEE, 2019, pp. 5323–5329.

[31] R. Miyazaki, R. Jiang, H. Paul, Y. Huang, and K. Shimonomura, “Long-reach aerial manipulation employing wire-suspended hand with swing-suppression device,” *IEEE Robotics and Automation Letters*, vol. 4, no. 3, pp. 3045–3052, 2019.

[32] D. Sanalitro, H. J. Savino, M. Tognon, J. Cortés, and A. Franchi, “Full-pose manipulation control of a cable-suspended load with multiple uavs under uncertainties,” *IEEE Robotics and Automation Letters*, vol. 5, no. 2, pp. 2185–2191, 2020.

[33] M. A. Trujillo, J. R. Martínez-de Dios, C. Martín, A. Viguria, and A. Ollero, “Novel aerial manipulator for accurate and robust industrial ndt contact inspection: A new tool for the oil and gas inspection industry,” *Sensors*, vol. 19, no. 6, 2019. [Online]. Available: https://www.mdpi.com/1424-8220/19/6/1305

[34] S. Hamaza and M. Kovac, “Omni-drone: on the design of a novel aerial manipulator with omni-directional workspace,” in *2020 17th International Conference on Ubiquitous Robots (UR)*, 2020, pp. 153–158.

[35] F. Shi, M. Zhao, M. Murooka, K. Okada, and M. Inaba, “Aerial regrasping: Pivoting with transformable multilink aerial robot,” in *2020 IEEE International Conference on Robotics and Automation (ICRA)*, 2020, pp. 200–207.

[36] M. Zhao, T. Anzai, F. Shi, X. Chen, K. Okada, and M. Inaba, “Design, modeling, and control of an aerial robot dragon: A dual-rotor-embedded multilink robot with the ability of multi-degree-of-freedom aerial transformation,” *IEEE Robotics and Automation Letters*, vol. 3, no. 2, pp. 1176–1183, 2018.

[37] B. Gabrich, D. Saldaña, V. Kumar, and M. Yim, “A flying gripper based on cuboid modular robots,” in *2018 IEEE International Conference on Robotics and Automation (ICRA)*, 2018, pp. 7024–7030.

[38] R. Ricard and C. M. Gosselin, “On the development of reactionless parallel manipulators,” in *International Design Engineering Technical Conferences and Computers and Information in Engineering Conference*, vol. 35173. American Society of Mechanical Engineers, 2000, pp. 493–502.

[39] Y. Wu and C. M. Gosselin, “Synthesis of reactionless spatial 3-dof and 6-dof mechanisms without separate counter-rotations,” *The International Journal of Robotics Research*, vol. 23, no. 6, pp. 625–642, 2004.

[40] S. Stan, “Workspace optimization of a two degree of freedom mini parallel robot,” in *2006 IEEE International Conference on Automation, Quality and Testing, Robotics*, vol. 2, 2006, pp. 278–283.

[41] C. Ferraresi, G. Montacchini, and M. Sorli, “Workspace and dexterity evaluation of 6 dof spatial mechanisms,” in *Proceedings of the ninth World Congress on the theory of Machines and Mechanism*, 1995, pp. 57–61.

[42] T. W. Danko, K. P. Chaney, and P. Y. Oh, “A parallel manipulator for mobile manipulating uavs,” in *2015 IEEE International Conference on Technologies for Practical Robot Applications (TePRA)*, 2015, pp. 1–6.

4

Discussion

In Chapter Two, an investigation into aerial manipulator morphologies was conducted to determine which morphology offers the largest workspace, which is the most stable, and which is the safest. This study significantly influenced the outcome of this thesis, primarily due to the potential identified in the center-mounted morphology. This morphology places the manipulator at the centre of the UAV, avoiding interference with the UAV, allowing for an omnidirectional workspace. Along this morphology offers a planar design space with limited obstructions which combines well with the theory of inherent dynamic balance. As long as the manipulator design remains planar, it can be adapted into an aerial manipulator by mounting the UAV's components on both sides of the manipulator. Thus, simplifying the problem of designing an aerial manipulator to designing a manipulator that can eventually be made to fly. This also makes that although the presented manipulator arm is designed with aerial manipulation in mind it could also be used for other applications. For example, it could be utilized on alternative mobile bases where the risk of tipping over would be a concern if the manipulator were to extend beyond its base.

From the investigation, it appeared that the suspended morphology is intrinsically the safest. This is mostly because of the large distance between the drone and the manipulator that can be created which gives more time and space to correct for disturbances. The suspended setup does not allow the transmission of forces from the manipulator which removes the possibility of destabilizing the UAV caused by the manipulator's motion. Although safety played no key role in this thesis it is often acknowledged as one of the main concerns limiting the applicability of aerial manipulators. Therefore it is important to express the possibility of combining dynamically balanced manipulators with the morphology of suspended manipulators. Balanced manipulators do not suffer from the inability to transmit reaction forces to the base, which in this case is the UAV. This combination could form a new direction for UAM design leading towards safer designs.

The use of two inverted four-bar mechanisms stacked on one another was selected as it was the only mechanism found that is inherently moment balanced while it can achieve an omnidirectional workspace. It was decided to search for an inherently balanced mechanism as the hypothesis was that this would help to decrease the weight of the manipulator. The design presented, shows that lightweight balanced manipulators can be designed with this method, but to determine if this is the optimal balance strategy, the design should be compared with other strategies.

In [15], the balancing performance regarding the addition of mass and inertia for a balanced double pendulum using counter rotating counter masses (CRCMs), separate counter-rotations (SCRs), an idlerloop (IL) with separate counter-rotations, and by duplicating the mechanism (DM) is evaluated. The addition of mass is evaluated by determining the required additional mass to balance a payload. The manipulator arm can be compared with these as in essence it is a double pendulum consisting of links three and six, see Figure 4.1. These two links are required to position the end-effector relative to the base and the other links are used to force and moment balance these. Using the mass optimisation the total mass of the manipulator arm is evaluated for two cases. The first with a payload of 20 grams located at the end-effector and the second without a payload which corresponds to the manipulator as presented in this thesis. In Figure 4.2, the result of the mass optimisation is plotted for both cases. The mechanism is shown with the balance masses represented by the red circles and the masses of the

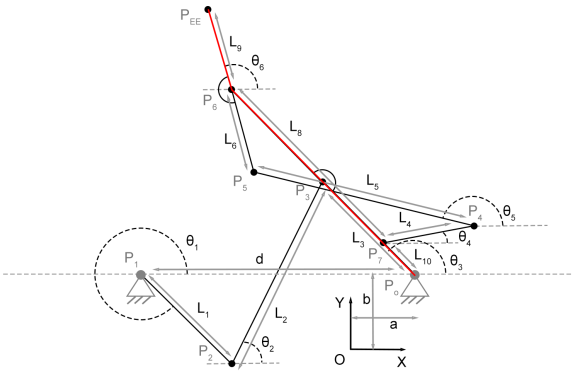

Figure 4.1: Manipulator arm in which the double pendulum is displayed with the red lines.

links by the blue circles. The case without payload requires a mass of 708.2 g and the case with 20 grams payload requires a mass of 1061.0 g for the balanced mechanism. This shows that to balance a payload of 20 grams an additional 352.8 g is required, which comes down to a factor of 17.64 times the payload. The obtained result can be compared to the results shown in [15], although this should only be considered as an indicative result as the parameters for the evaluation differ. This suggests that this method would be comparable to using counter-rotating counter masses and thus heavier than using duplicate mechanisms. Of course, there are many shortcomings in this quick comparison but it highlights the importance of evaluating the balancing performance of the presented design. It is recommended to perform this comparison in more detail in future work as the results are interesting for the field of dynamic balance and it could have an impact on future aerial manipulators benefiting from dynamic balance. It would be interesting to include the mass of the mechanism itself in this evaluation.

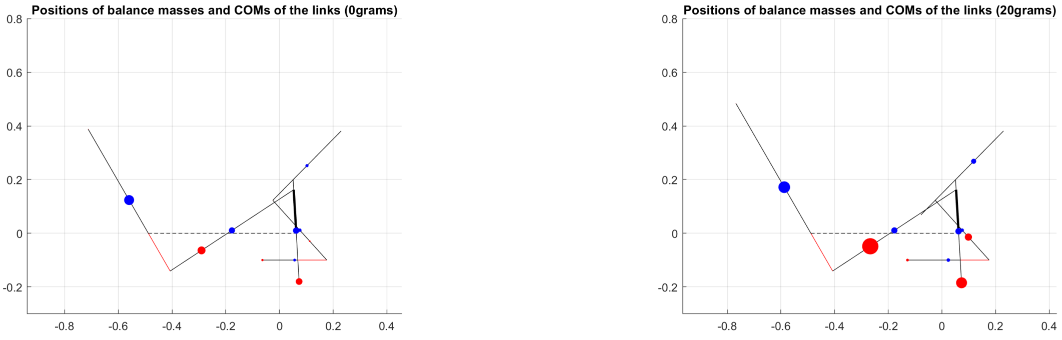

(a) No payload.

(b) Payload of 20 grams.

Figure 4.2: Visualisation of the positions of the balance masses (red) and the COMs of the links (blue).

Furthermore it would be interesting to include the method of moment balancing an inherently force-balanced mechanism with a counter inertia, to this evaluation. During the design process, this type of designs were discarded as they used counter-inertias. This decision was made with the intention of creating a manipulator that is as lightweight as possible. However, upon a brief evaluation of the manipulator arm, it appears that this decision should be questioned. For instance a similar two DoF manipulator arm could be constructed by replacing links one and two with a counter inertia. The combined COM of links three, four, five and six then needs to be located in P_1, to be force-balanced. Adding a counter inertia would restore the moment balance of the mechanism. Modelling this inertia as an ring with a radius of $25\ cm$, the counter inertia would require a mass of 154 grams if a one-to-one ratio is considered. However, the combined mass of links one and two is approximately 384 grams, indicating a higher mass compared to the counter inertia.

4.0.1. Recomendation for future work

The goal of designing an two DoF inherently balanced flying manipulator with an omnidirectional workspace is accomplished. To constrain the problem it was chosen to aim for a two-DoF design. It would be interesting to extend this in future work to three DoFs, to compensate for all spatial errors of the UAV.

Furthermore it would be interesting to test the manipulator arm in flight. Although a balanced manipulator is expected to increase manipulation accuracy of UAMs this is not yet shown in practice.

Lastly, it is recommended to extend the study as presented in [15], to find which balancing method adds the least amount of mass and/or inertia. In this study not only the method of full inherent balance, as used for the design presented in this thesis should be included, but also a hybrid version consisting of an inherent force-balanced mechanisms moment balanced with a counter inertia. It would be interesting to include the mass of the links in this evaluation. The mass optimisation used in this thesis could help perform this comparison. The different balancing methods could be modelled similarly to the model as used in this thesis, after which these can be used to optimise two cases using the same kinematic parameters. One could minimize the mass and the other the inertia of the mechanism, after which the found values can be compared.

5

Conclusion

In chapter two of this thesis, an investigation into aerial manipulator morphologies was presented. In this study, UAM designs were categorized based on the manipulator placement, i.e. morphology, to determine which morphology offers the largest workspace, which is the most stable and which is the safest. It was found that the center-mounted morphology offers the largest workspace, as this morphology is the only morphology that enables the manipulator to manipulate all around the UAV. The bottom-mounted manipulator morphology was shown to be the most stable. This, while the UAMs using the most advanced balancing solutions are found in this morphology. The suspended morphology was shown to be the safest. It offers a large distance between the UAV and the manipulator, which keeps the dangerous propellers far away from the manipulator and results in longer reaction times for the controller. Furthermore, the suspended setup does not allow rigid transmission of interaction forces which decreases the risk of destabilisation.

It was derived that the center-mounted morphology allows for the free design of a planar manipulator arm, which can be transformed into an aerial manipulator by attaching the UAV's components to both sides. This insight led to a new design approach of making a manipulator fly, different from the common approach of mounting a manipulator arm to a UAV. This novel approach enables a focus on the design of the manipulator arm. As long as the manipulator arm remains planar and the UAV's propellers can be connected to both sides, it can be transformed into a flying manipulator. This design approach avoids interference with the UAV's components, making it suitable for achieving an omnidirectional workspace as well as an inherently dynamically balanced design.

In Chapter Three, a two-degree-of-freedom, inherently fully dynamically balanced flying manipulator with an omnidirectional workspace was presented. The manipulator arm is constructed from two inverted four-bar mechanisms stacked on top of one another. The different configurations of the inverted four-bar mechanisms combined create an omnidirectional workspace. The balance conditions of the manipulator arm were presented and used to optimise the manipulator. A bilevel optimisation approach was employed to optimise the workspace while ensuring that the total mass of the manipulator arm remained under 750 grams. The mass of the manipulator was minimised through an embedded optimisation used to constrain the main optimisation process. The design of the manipulator was verified with a dynamic simulation. A prototype of the design was built, and the balance quality of the prototype was measured. Unfortunately, the measurements were insufficient for evaluation. Nonetheless, the prototype demonstrates the feasibility of the design.

A

Overview Balancing Concepts

The design process leading to the design as presented in this thesis consisted of a long concept phase. During the concept phase, many ideas were explored. This appendix gives an overview of these ideas. In the second part of this appendix, more attention is paid to one of these concepts, namely payload adjustable mechanisms. This appendix will conclude with some general remarks about these concepts.

A.1. Pantograph based 5 bar linkages

The design of the omni-drone, see [2], uses a 5-bar linkage as the manipulator, a similar structure could be constructed such that it is balanced. A dynamic force-balanced mechanism can be constructed by replacing two links of the original 5-bar and replacing it with a pantograph. Also another configuration of the pantograph, as seen in [16], can be used. The system can be balanced either by using a single pantograph, both configurations are possible, or by using two pantographs. The sketches depicted below illustrate the different options.

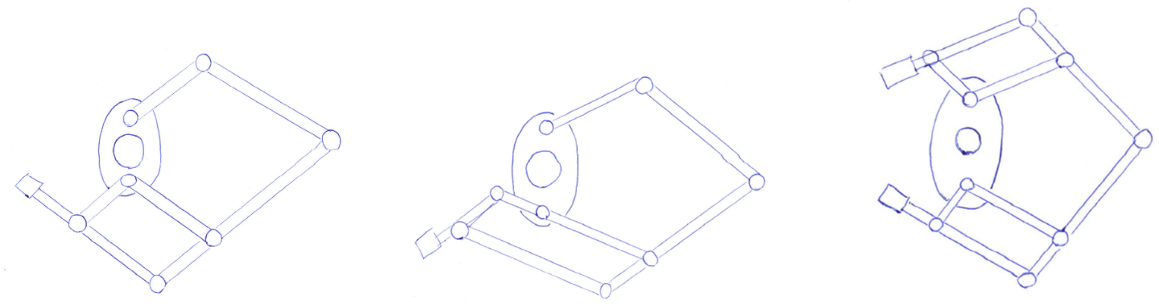

(a) Single pantograph

(b) Different configuration of pantograph

(c) Two pantographs 5-bar

Figure A.1: Different force balanced 5-bar linkages

This only yields a force-balanced design, to get a fully dynamic balanced design moment balance should also be considered. Multiple solutions can be used to obtain this. Mirroring the mechanism and the movement of the mechanism during operation is one of them. The main difficulty is that the two mechanisms obstruct each other, to solve this it would be possible to construct both planar mechanisms in another plane. This removes the physical limitations and as moments do not have a point of application it does not affect the balance.

It would be interesting to use control to make the mechanism move in a mirrored fashion. This would allow the mechanism to reshape in an unbalanced manner before manipulating at high speed or high accuracy is required. If this were done mechanically, the mechanisms would be located on opposite sides for certain parts of the movement but obstruct each other for others which is undesired.

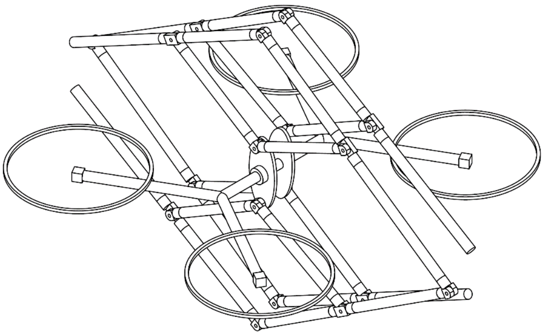

Figure A.2: Illustration of fully balanced manipulator based on pantographs and using a mirrored mechanism to obtain moment balance.

A.2. Moment balancing idler loops

In [17] several moment balancing techniques are discussed, one of which is moment balancing using idler loops. This technique is introduced by Bagci in [18]. Here the rotation of a distal link is transferred to the base with idler loops and is balanced with a counter-rotating inertia at the base.

For instance, a pantograph could be used as the moment balancing idler loop is already part of this linkage. The force balancing conditions of a pantograph allow for an efficient balancing solution and are well known. Unfortunately, from the equations, it appeared to be necessary for all the links to be force balanced individually. This is undesired as balancing the links individually likely results in heavier designs than designs that are inherently balanced. The two base links are connected to counter inertias positioned at the COM to make the mechanism moment balanced. Figure A.3a shows the pantograph used to construct the balancing idler loop. As the links have to be balanced individually and cannot use the balancing characteristics of the pantograph a linkage as shown in Figure A.3b can also be used, where the mass and inertia of the link on the lower left can be incorporated in the other links.

(a) Pantograph-based idler loop concept

(b) Idler loop concept with individually balanced links

Figure A.3: Moment balancing idler loop concepts

A.3. Counter-Mechanism

Using a counter mechanism to moment balance a system is presented in [19]. The initial manipulator is force-balanced such that only the reaction moments have to be compensated. This can be achieved by a scaled version of the manipulator but also by a different linkage. This counter mechanism should be able to reconfigure such that it matches the inertia of the system. It is also possible to use control to achieve the same with a counter inertia with fixed inertia.

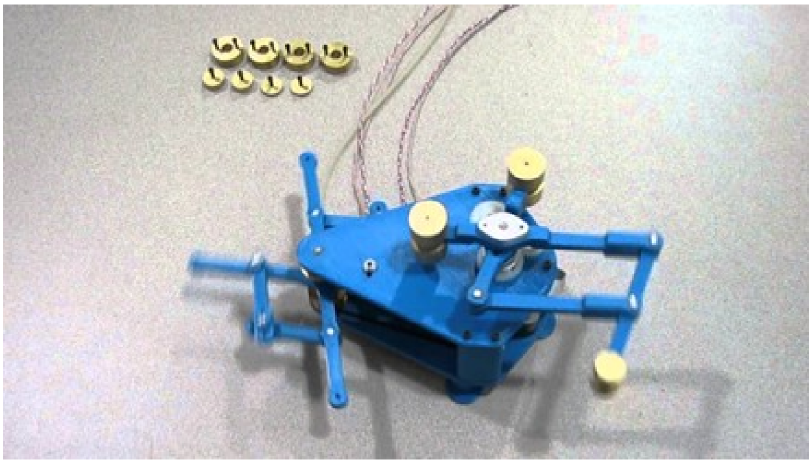

Figure A.4: Full balance using counter mechanism, source [19].

A.4. Constant inertia mechanism

As mentioned it is possible to moment balance planar systems using only one counter inertia and some help of control. This means that there can also be a mechanical solution found that requires only one counter inertia even with fixed inertia. One of these solutions is found in using a constant inertia mechanism. In [20] the conditions to balance a two DoF parallelogram are presented. The mechanisms sketched below are constant inertia mechanisms (under certain conditions) and could be used for a manipulator design. To achieve full dynamic balance the mass should be distributed such that its COM is located in the base pivot point at all times.

A.4.1. Distribution of actuators

The constant inertia concepts only require one counter inertia. To practically implement this, it is useful if the motion of the mechanism, and also the actuator/DoFs are divided in a rotation of the mechanism and an extension or translation. Otherwise, both actuators should be coupled to one counter inertia complicating the mechanism. Figure A.5a places the DoF such that one controls an extension which is moment-balanced due to symmetry and a rotation balanced by the counter inertia. Figure A.5b uses a reactionless four-bar to get a reactionless extension, note that this is not a pure extension. The other DoF rotates the whole mechanism and uses the counter inertia to balance this movement.

(a) Constant inertia parallelogram

(b) Constant inertia reactionless four-bar

Figure A.5: Concepts that distribute the movement in a reactionless rotation and extension.

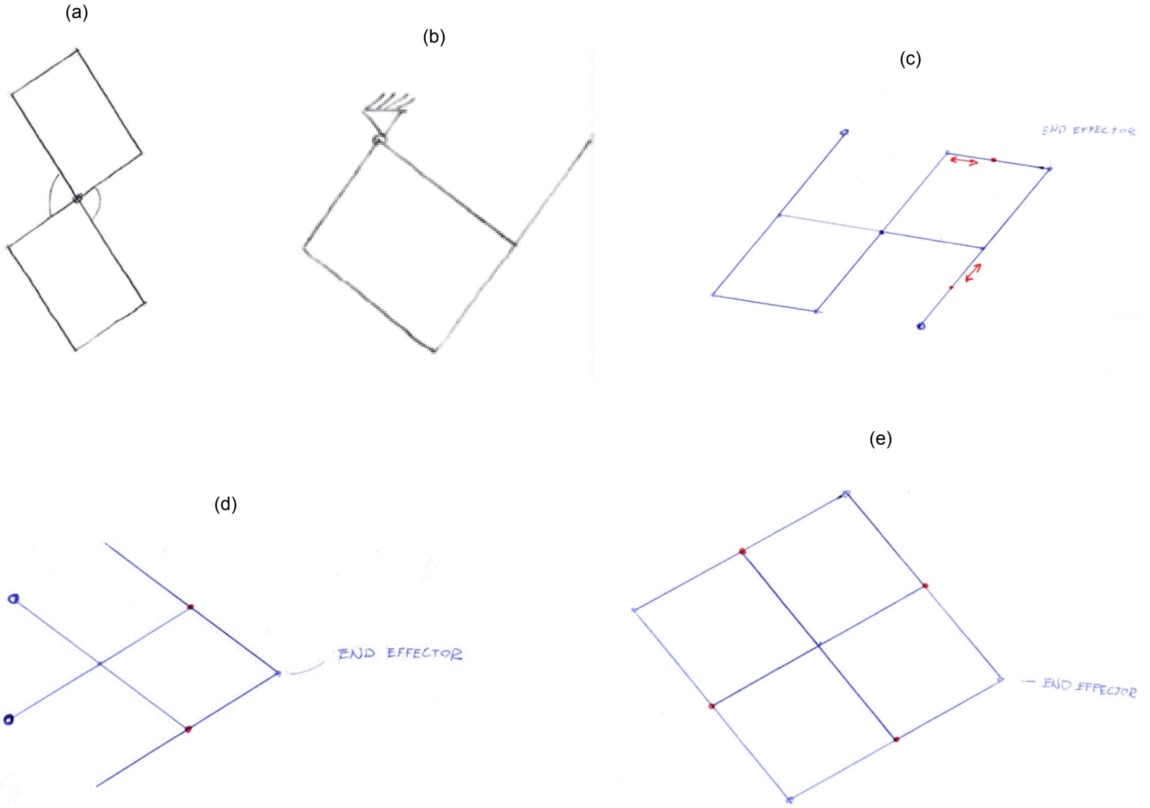

Figure A.6: Manipulator concepts based on constant inertia mechanisms

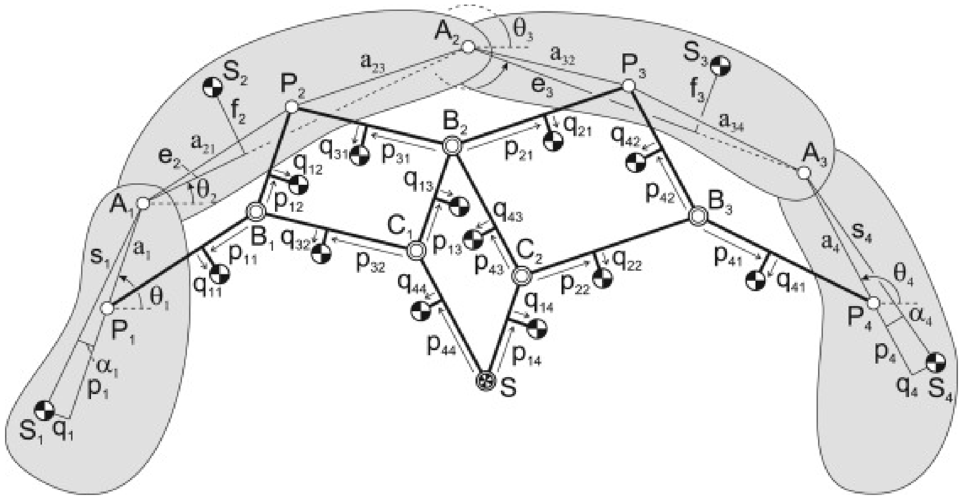

Figure A.7: 4 DoF principal vector linkage (inherently force balanced)

A.5. Reduced 4 DoF principal vector linkage

As shown in [21] a strategy of reducing a force-balanced system's DoFs can be used to obtain fully balanced concepts. The examples shown in the paper start with 3 DoF principal vector linkages and get reduced to one-DoF linkages. This approach could also be tried while starting with a 4 DoF principal vector linkage, shown in Figure A.7, hopefully resulting in a fully balanced 2 DoF manipulator. This could also be extended to starting with higher DoF principal vector linkages.

Note: A downside of this approach is that this will likely not yield an omnidirectional manipulator. The full rotation is probably not practically obtainable as other links have to make the same rotation in opposite directions, which can be obstructed due to singularities or simply because links obstruct each other.

B

Payload adjustable mechanism

Dynamically balanced manipulators are balanced for a certain condition. If these are changed, for instance by picking up a payload, the dynamic balance is lost. In most pick-and-place operations the mass of the payload is low compared to the mass of the manipulator. So although the balance is lost, the system remains close to balanced, and the benefits of reduced reaction forces or vibrations are still present. In the field of aerial manipulation weight is however much more of a concern, as there is no solid ground which can bear this mass. The manipulator has to be as light as possible and the payloads become thereby less negligible. A manipulator that can adjust for the payload is therefore interesting for this field. In [16] and [22] different strategies are presented. The methods of relocating the mass or joint positions are used for the concepts shown in this appendix, therefore these are shortly explained. As removing reaction forces is the main purpose of dynamic balancing, reconfiguring the balance of the system in a dynamically balanced fashion is desired. Unfortunately, this is generally complicated to achieve and is therefore not considered in the concepts shown in this appendix.

B.0.1. Relocating counter mass

By relocating the counter mass the balance conditions can be adjusted. The simplest case to illustrate this is a pendulum. If a pendulum gets balanced an equal counter mass can be placed at an equal distance on the opposite side. If the original mass changes this can be compensated by placing the counter mass at a larger distance. Figure B.1a shows a concept which shows how to achieve this changing mass.

B.0.2. Relocating centre of rotation

Similar to relocating the counter mass, the centre of rotation (COR) can be changed which has logically the same effect on the balance.

As reconfigurable balance could be interesting some exploration on this topic was performed. The coming sections present the exploration steps taken in this direction. Although the exploration of this path was ended during this thesis, it does not mean this path is a dead end. In this appendix, no conclusions are drawn on the feasibility or usability as this would require further work. Nevertheless, the presented results could pave the way for any future explorations in this direction.

B.1. Changeable Inertia

A practical approach to building a reconfigurable moment-balanced system is using an independently actuated counter inertia and using control to balance the system. Due to mass restriction, using an additional actuator might not be possible for a UAM. Mechanical solutions that could achieve the same rely on either changing the inertia or the transmission ratio. In Figure B.1b a sketch of a changeable counter inertia that uses linear actuators to change the inertia.

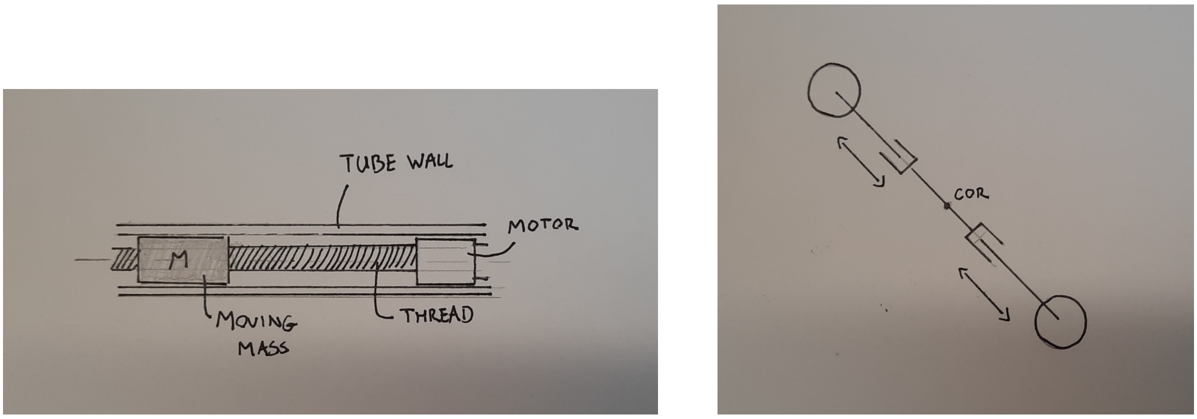

(a) Changing mass position with linear actuator

(b) Changeable counter inertia concept

Figure B.1: Reconfigurable balancing concepts

B.2. Testing reconfiguration mechanisms

In this section, the possibilities of reconfigurable mechanisms are explored. This is done for several mechanisms each with different features. All have two degrees of freedom as this is required for the intended flying manipulator. The method and results will be described per linkage.

B.2.1. Closed loop inherently balanced

There are many closed loop inherently balanced linkages possible, in [23] 32 two-DoF linkages are presented. All would suffice for this comparison, and as the sole purpose is to gain insight, little attention is paid to selecting one for this comparison. Example 5, from [23] will be used, as the distribution of links seems denser on one side than on the other, which could help to balance payload. In Figure B.2 the linkage, and its parameters accompanied by the balance equations are shown.

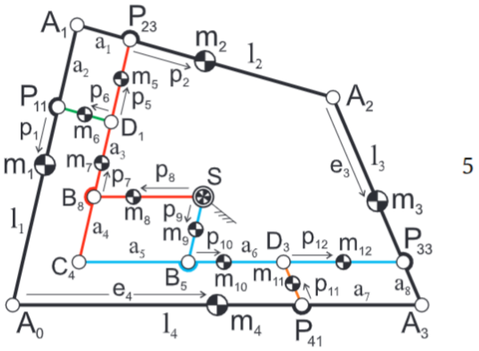

$$
\begin{aligned}
&(m_1 + m_3 + m_4 + m_{11}(1 - \tfrac{p_{11}}{a_8}))a_1 - \\
&\quad m_2 p_2 - m_3(1 - \tfrac{e_3}{l_3})l_2 + m_6 p_6 = 0 \\
&(m_1 + m_2 + m_3 + m_4 + m_5 + m_6 + \\
&\quad m_{11}(1 - \tfrac{p_{11}}{a_8}))a_3 - m_1 p_1 + m_5 p_5 + \\
&\quad m_7 p_7 + (m_2 + m_3 + m_4 + \\
&\quad m_{11}(1 - \tfrac{p_{11}}{a_8}))a_2 - (m_3 \tfrac{e_3}{l_3} + m_4 + \\
&\quad m_{11}(1 - \tfrac{p_{11}}{a_8}))l_1 - m_9 p_9 - \\
&\quad (m_{10} + m_{11} \tfrac{p_{11}}{a_8} + m_{12})a_4 = 0 \\
&(m_1 + m_2 + m_3 + m_4 + m_5 + m_6 + \\
&\quad m_7 + m_{11}(1 - \tfrac{p_{11}}{a_8}))a_5 - m_4 e_4 - \\
&\quad m_3 \tfrac{e_3}{l_3} l_4 - m_{11}(1 - \tfrac{p_{11}}{a_8})(l_4 - a_7) - \\
&\quad m_{10} p_{10} - m_{11} \tfrac{p_{11}}{a_8} a_6 - \\
&\quad m_{12}(a_6 + p_{12}) + m_8 p_8 = 0
\end{aligned}
$$

Figure B.2: 2DoF closed loop inherently balanced linkage

Point S, represent the centre of mass of the manipulator once the balance conditions are satisfied. To construct a balanced flying manipulator from this, the mechanism will be mounted to the centre of the UAV in point S. The two DoFs will also be actuated from this point, and these will control the position of the links considered with p8 and p9. These will affect the position of point A2 which is considered the end effector. So, the additional mass will be added in point A2, and it is tried to change the lengths of the links such that balance is restored. This reconfiguration will not happen in a balanced way. In an actual manipulator, the links need to be able to adjust their length and will thereby change the position of its centre of mass. How this COM changes will depend on how such a link is constructed and in this simplified version these links will be modelled as tubes which can change their length. These links will therefore not only shift the COM but their mass will also change with the extension.

To get the linkage force balanced, three equations need to be satisfied, meaning that at least three parameters must be changeable. In this case, the links will be constructed of tubes all with the same diameter, thickness and density. The COM of a link, therefore, depends on its length, which makes that only the link lengths can be used to achieve force balance. The variables, L1, L2 and L4 are picked as the links that can be changed to re-adjust the balance of the linkage. So far only the balance equations are discussed but as the picture already gives away, there are also kinematic constraints that have to be satisfied. One can identify two 4-bar linkages in the structure and if the links of these are not scaled with the same factor the balance condition will become invalid. This results in three additional kinematic relations constraining the length of links a7, a2 and a1. Equation B.1, B.2 and B.3 show the kinematic constraints and Equation B.4, B.5 and B.6 show the balance equations.

$$a_7 = \frac{a_5 \cdot (l_3 + a_8) + a_6 \cdot (l_3 + a_8) - l_3 \cdot l_4}{-a_8} \tag{B.1}$$

$$a_2 = \frac{l_3(a_3 + a_4) + a_8(a_3 + a_4) - l_1 l_3}{-a_8} \tag{B.2}$$

$$a_1 = \frac{l_2 a_8}{l_3} \tag{B.3}$$

$$\begin{aligned} a_5\, m_1 + a_5\, m_2 + \frac{a_5\, m_3}{2} + a_5\, m_5 + a_5\, m_6 + a_5\, m_7 - \frac{a_6\, m_{11}}{2} + m_8\, p_8 - m_{10}\, p_{10} + m_4\ (a_5 - e_4) \\ + \frac{m_{11}\ (a_5 - l_4)}{2} - \frac{m_3\ (a_7 - a_5 + l_4)}{2} - m_{12}\ (a_6 + p_{12}) = 0 \end{aligned} \tag{B.4}$$

$$\begin{aligned} a_4\, m_{10} - a_3\, m_6 + \frac{a_4\, m_{11}}{2} + a_4\, m_{12} - m_7\, p_7 + m_9\, p_9 - \frac{m_3\ (a_3 - l_1)}{2} - m_4\ (a_3 - l_1) \\ - \frac{m_{11}\ (a_3 - l_1)}{2} - m_1\ (a_3 - p_1) - m_2\ (a_2 + a_3) - \frac{m_3\ (a_2 + a_3)}{2} - m_5\ (a_3 + p_5) = 0 \end{aligned} \tag{B.5}$$

$$\frac{l_2\, m_3}{2} - \frac{a_1\, m_3}{2} - a_1\, m_4 - \frac{a_1\, m_{11}}{2} - a_1\, m_1 + m_2\, p_2 - m_6\, p_6 = 0 \tag{B.6}$$

Without payload

First, the mechanism will be balanced without an additional payload attached. The obtained linkage will be used as a reference to observe how the link lengths must change in order to balance added payload. Now, more and more payload can be added and the link lengths will be updated in order to maintain balance. The dimensions of the mechanism are displayed in B.1, for various payloads. These values are obtained using a mass of $0.30535(kg/m)$, which corresponds to a hollow aluminium rod with an outer diameter of $20mm$ and a wall thickness of $2mm$.

Table B.1: Overview of the dimensions of the balanced linkage with payload included in the balance equations

Payload (kg)	0	0.01	0.02	0.05
a_1 (m)	0.1531	0.1358	0.1187	0.0686
a_2 (m)	0.2284	0.2439	0.2600	0.3121
a_3 (m)	0.16	0.16	0.16	0.16
a_4 (m)	0.15	0.15	0.15	0.15
a_5 (m)	0.24	0.24	0.24	0.24
a_6 (m)	0.21	0.21	0.21	0.21
a_7 (m)	0.3420	0.3375	0.3332	0.3225
a_8 (m)	0.1	0.1	0.1	0.1
l_1 (m)	0.4481	0.4520	0.4561	0.4695
l_2 (m)	0.5970	0.5297	0.4631	0.2675
l_3 (m)	0.39	0.39	0.39	0.39
l_4 (m)	0.6531	0.6519	0.6508	0.6481

Looking at for instance the values for link l_2, it becomes clear that balancing the payload requires substantial link length reconfiguration. With these large changes, the validity of the modelling method can be questioned. In practice, the mass of the changing links will not depend on the link length and only the COM of this link will change depending on its extension. The total mass of the system is about $1.49kg$ although it changes due to the changing links. Comparing the maximum payload, 50 grams, that can be balanced to the weight of the mechanism poses the question if the reconfiguration is worth the hassle. While the payload that can be balanced is only a fraction of the weight of the manipulator. To reduce the hassle and hopefully increase the payload that can be balanced another idea is tried. This idea will be elaborated in the next section.

(a) without payload

(b) 10 gram payload

(c) 20 gram payload

(d) 50 gram payload

Figure B.3: Reconfiguration by changing link lengths

B.2.2. Sliding masses

In the previous example six links needed to change length due to the geometric constraints. If other variables present in the balancing equation are selected it is possible to reduce the complexity to only three moving elements. Changing the mass is considered not to be possible, therefore the only possibility remains to relocate the COM of three links. In this case, this will be accomplished by moving a mass over the associated links. Figure B.4 shows, in yellow, the three moving masses used to balance the payload. The mass shown in purple is an extra mass that is used to increase (relative to the total weight of the mechanism) the maximal payload that can be balanced. The lengths of the links used in this example are chosen such that these balance themselves. So, only the moving masses are used to balance the payload.

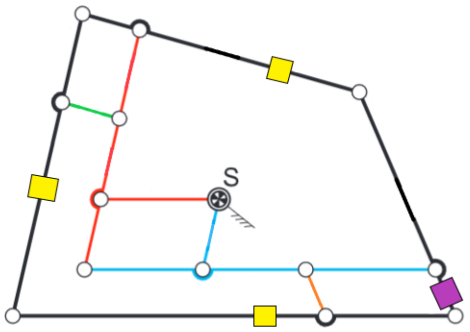

Figure B.4: Mechanism with added masses, shown in yellow, that slide over the links to balance the mechanism.

The equations enforcing balance for this mechanism are derived and are shown in Equation B.7, B.8 and B.9. All dimensions and masses are presented in Table B.2. The masses used to balance have a combined weight of $1.35kg$, with these masses the mechanism can balance a payload up to $0.2kg$.

$$\begin{aligned}(a_8+l_3)(2a_5m_1+2a_5m_2+2a_5m_5+2a_5m_6+2a_5m_7-a_6m_{11}+2a_5\mathrm{ma}_1+2a_5\mathrm{ma}_2+2m_8p_8\\ -2m_{10}p_{10}+2m_4(a_5-e_4)+m_{11}(a_5-l_4)+2\mathrm{ma}_4(a_5-\mathrm{lma}_4)-2m_{12}(a_6+p_{12}))\\ +2a_5m_3(a_8-e_3+l_3)+2a_5\mathrm{ma}_3(a_8+l_3-\mathrm{lma}_3)=2e_3m_3(a_7-a_5+l_4)\\ +2\mathrm{lma}_3\mathrm{ma}_3(a_7-a_5+l_4)\end{aligned} \tag{B.7}$$

$$\begin{aligned}(a_8+l_3)(2a_3m_6-2a_4m_{10}-a_4m_{11}-2a_4m_{12}+2m_7p_7-2m_9p_9+2m_4(a_3-l_1)+m_{11}(a_3-l_1)\\ +2\mathrm{ma}_4(a_3-l_1)+2m_1(a_3-p_1)+2\mathrm{ma}_1(a_2+a_3-\mathrm{lma}_1)+2m_2(a_2+a_3)+2\mathrm{ma}_2(a_2+a_3)\\ +2m_5(a_3+p_5))+2e_3m_3(a_3-l_1)+2\mathrm{lma}_3\mathrm{ma}_3(a_3-l_1)+2m_3(a_2+a_3)(a_8-e_3+l_3)\\ +2\mathrm{ma}_3(a_2+a_3)(a_8+l_3-\mathrm{lma}_3=0\end{aligned} \tag{B.8}$$

$$\begin{aligned}(a_8+l_3)(2a_1m_1+2a_1m_4+a_1m_{11}+2a_1\mathrm{ma}_1+2a_1\mathrm{ma}_4-2m_2p_2+2m_6p_6+2\mathrm{ma}_2(a_1-\mathrm{lma}_2))\\ +2a_1e_3m_3+2a_1\mathrm{lma}_3\mathrm{ma}_3=2l_2m_3(a_8-e_3+l_3)\\ +2l_2\mathrm{ma}_3(a_8+l_3-\mathrm{lma}_3)\end{aligned} \tag{B.9}$$

Table B.2: Overview of the dimensions to achieve balance with the sliding masses

Payload (kg)	0	0.01	0.05	0.1	0.2
Lma_1 (m)	0.4435	0.4632	0.5418	0.6402	0.8369
Lma_2 (m)	0.3494	0.3323	0.2642	0.179	0.0087
Lma_3 (m)	0.65	0.65	0.65	0.65	0.65
Lma_4 (m)	0.0476	0.0564	0.0914	0.1351	0.2226
Ma_1 (kg)	0.4	0.4	0.4	0.4	0.4
Ma_2 (kg)	0.2	0.2	0.2	0.2	0.2
Ma_3 (kg)	0.35	0.35	0.35	0.35	0.35
Ma_4 (kg)	0.4	0.4	0.4	0.4	0.4
a_1 (m)	0.0577	0.0577	0.0577	0.0577	0.0577
a_2 (m)	0.6268	0.6268	0.6268	0.6268	0.6268
a_3 (m)	0.16	0.16	0.16	0.16	0.16
a_4 (m)	0.25	0.25	0.25	0.25	0.25
a_5 (m)	0.35	0.35	0.35	0.35	0.35
a_6 (m)	0.21	0.21	0.21	0.21	0.21
a_7 (m)	0.616	0.616	0.616	0.616	0.616
a_8 (m)	0.1	0.1	0.1	0.1	0.1
l_1 (m)	0.5857	0.5857	0.5857	0.5857	0.5857
l_2 (m)	0.3407	0.3407	0.3407	0.3407	0.3407
l_3 (m)	0.59	0.59	0.59	0.59	0.59
l_4 (m)	0.7593	0.7593	0.7593	0.7593	0.7593

(a) No payload

(b) 10 grams payload

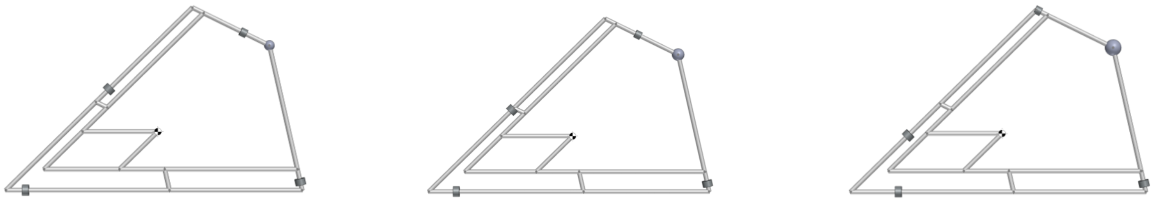

(c) 50 grams payload

(d) 100 grams payload

(e) 200 grams payload

Figure B.5: Reconfigurable balance by sliding masses

B.2.3. Changing link length with constant weight

At first, the reconfiguration by changing link lengths was modelled such that the mass of the link changes with its length. In practice, the change in length will not happen by adding or removing a piece from the link but by some sort of extension. To see how this affects the reconfiguration capacity of a mechanism a second model is made in which the links have constant weights. To make it somewhat realistic it is chosen that the COM remains in the center of the link and the extendable links have a weight that is almost double the weight of a link of its initial dimensions.

Initially, it was assumed that the same balancing equations could be used as in B.2.1. But this time the masses and COMs did not depend on the lengths of the links. Without the substitution, the balance equations were not able to solve for the variables L_1, L_3 and L_4. This is strange as there does exist a solution, but it cannot be obtained with this set of equations. The explanation for this phenomenon likely comes from the way the balancing equations are derived. The closed loop system is cut open and the mass of the link which is opened is placed on the remaining links. In this case, the link associated with L3 was opened and therefore unsolvable. Deriving a new set of equations would solve the issue, but in this case it is chosen to simply select other variables, namely L_1, L_4 and a_8. It could be that this influenced the solutions obtained in B.2.1 as the solutions exploited the relations brought in by the substitutions. It has not been tested to see if this influenced the results. Although it seems unlogical that it has influence it is good to be aware of this phenomenon and be aware that there should exist a solution using three random variables, but in some cases, you need to adjust the balance equation to find the solution.

Table B.3: Masses of the Changing Links

Link	Mass (g)
m1	400
m2	400
m3	400
m4	400
m5	140
m6	90
m11	90
m12	140

Table B.4: Overview of the dimensions to achieve balance with changing link lengths with constant mass

Payload (kg)	0	0.05	0.1	0.3
a_1 (m)	0.1829	0.2058	0.2287	0.3202
a_2 (m)	0.5554	0.5517	0.5481	0.5357
a_3 (m)	0.15	0.15	0.15	0.15
a_4 (m)	0.3	0.3	0.3	0.3
a_5 (m)	0.3	0.3	0.3	0.3
a_6 (m)	0.15	0.15	0.15	0.15
a_7 (m)	0.5554	0.5517	0.5481	0.5357
a_8 (m)	0.1829	0.2058	0.2287	0.3202
l_1 (m)	0.7618	0.7994	0.8369	0.9849
l_2 (m)	0.59	0.59	0.59	0.59
l_3 (m)	0.59	0.59	0.59	0.59
l_4 (m)	0.7618	0.7994	0.8369	0.9849

The mechanism has a weight of $2.518kg$ and can balance $0.3kg$ of payload. In Table B.4 and B.3 all important dimensions are shown. The mechanisms corresponding to these dimensions are displayed in Figure B.6. The blue links are placeholders for a mechanism that should be able to extend. To get the mass correct in this model additional masses are used such that the place and value can be controlled.

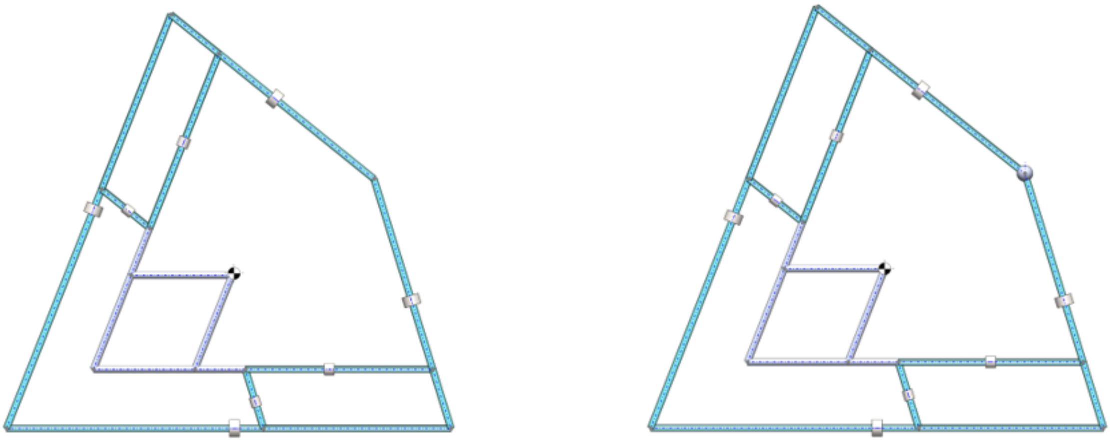

(a) No payload

(b) 50 grams payload

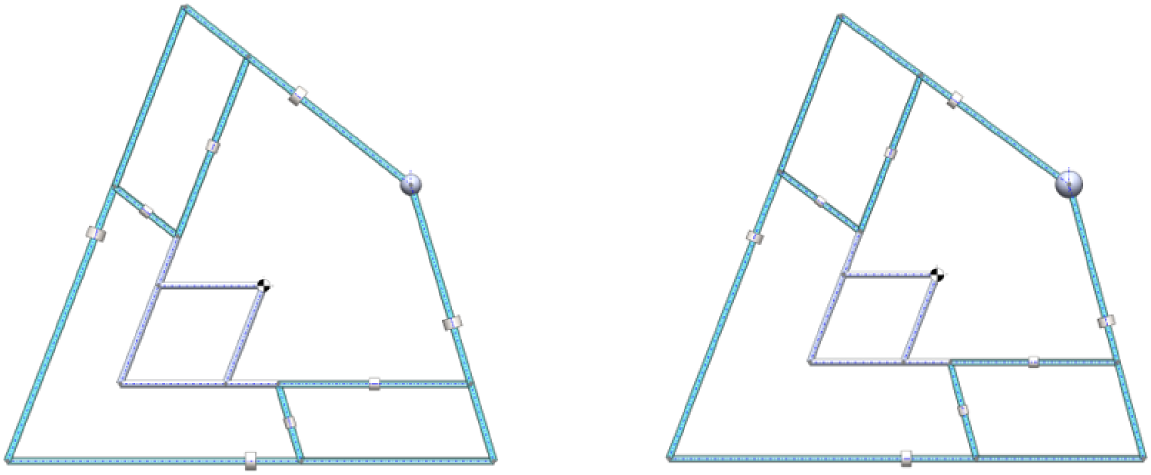

(c) 100 grams payload

(d) 300 grams payload

Figure B.6: Reconfigurable balance by changing link length with constant mass

B.2.4. Serial balanced manipulator

For the sake of comparison, the balance adaptability of a serial 2 DoF manipulator is also evaluated. The serial arms are balanced by a counterweight, of which the position can be changed. The weight of the mechanism without payload is 1.12737 kg.

B.3. Concept to design

In this section, the concept of using extendable links is further worked out. Starting with prototyping two linear actuator concepts which could be used in a reconfigurable manipulator. The concept that showed to be most promising is used to create a full CAD design.

B.3.1. Protoypes of linear actuators

To get a better feeling for the feasibility of such re-configurable manipulators two prototypes of linear actuators are made. Making linear actuators is necessary as the commercially available linear actuators

Table B.5: Dimensions serial reconfigurable manipulator

Payload (kg)	0	0.01	0.02	0.05	0.1
L_1 (m)	0.5	0.5	0.5	0.5	0.5
L_2 (m)	0.4	0.4	0.4	0.4	0.4
L_3 (m)	0.112	0.129	0.146	0.194	0.268
L_4 (m)	0.387	0.399	0.411	0.447	0.503
M_{c1} (kg)	0.2	0.2	0.2	0.2	0.2
M_{c2} (kg)	0.1	0.1	0.1	0.1	0.1

(a) No payload

(b) 10 grams payload

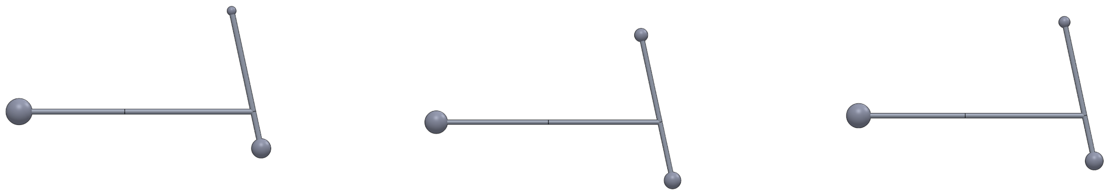

(c) 20 grams payload

(d) 50 grams payload

(e) 100 grams payload

Figure B.7: Reconfigurable serial manipulator by changing counter mass positions

are simply too heavy for drone manipulators. For each prototype, a different working principle was used to evaluate which would be most promising for further development. The linear actuator, shown in Figure B.8, uses an M3 threaded rod to convert the rotary motion of the motor into linear motion. The fine thread results in accurate motion with little play.

The second prototype, shown in Figure B.9, functions due to a rack and pinion transmission. A 3D-printed rack is glued into an aluminium U-profile. The pinion gear is driven by an inexpensive hobby-grade geared DC motor. The aluminium profiles slide in a printed housing constraining the motion of these parts to be linear. A downside of the printed parts is that the tolerances that can be achieved are low, and therefore the prototype requires a process of trial and error to get the design to work. This causes this linear actuator to display much more play, compared to the screw-based version. A benefit of this manipulator is that the movement of both aluminium parts makes large extensions possible, and is intrinsically faster. The screw-type linear actuator was shown to be most promising because it is easy to build and is more precise. A full design using this actuator of a reconfigurable manipulator is worked out and shown.

Figure B.8: Prototype of screw-based linear actuator.

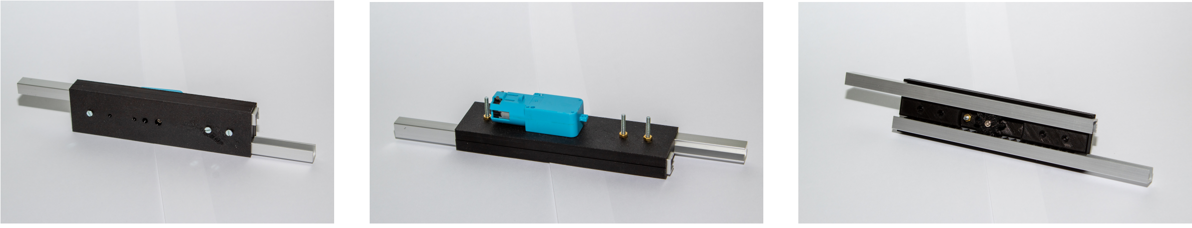

(a) Front view (b) Back view (c) Internal mechanism

Figure B.9: Rack and pinion-based linear actuator prototype.

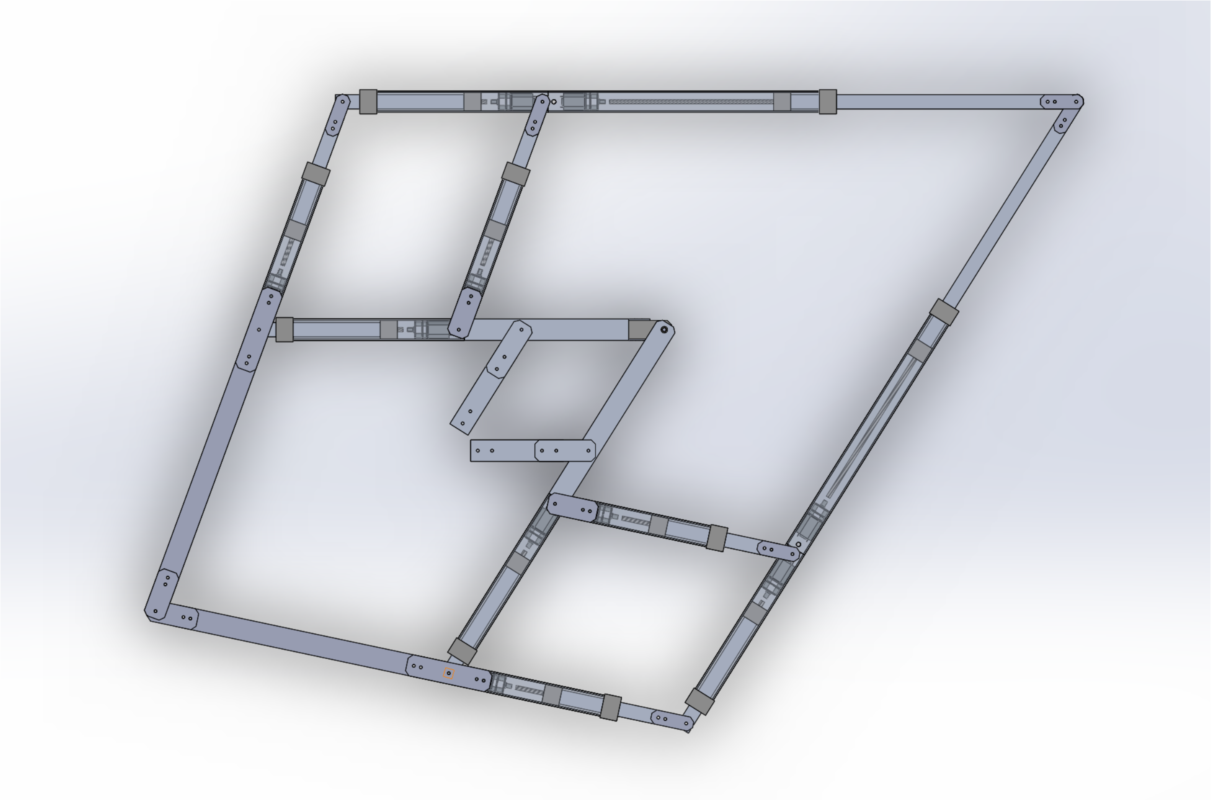

Figure B.10: Design of a reconfigurable manipulator using screw-based linear actuators.

C

An alternative approach to moment balancing

The concepts/designs in A mostly relied on using a counter-rotating inertia to moment balance the mechanism. Both passive and active counter inertias were used in these examples but the goal of finding a fully inherently balanced solution was not accomplished. In the design process, the focus shifted towards this goal of finding an inherently moment-balanced mechanism. In this appendix the three concepts, other than the stacked inverted four-bar, that were studied in this process are presented. Starting with an introduction about the inspiration behind these concepts.

C.1. Inspiration

Moment-balanced mechanisms that do not use a counter wheel do exist, and from examples found in literature, the general design rules can be learnt. Starting with the DUAL-V manipulator, in the paper presenting the manipulator the author nicely explained the key aspect of these balanced designs. *”Since for dynamic balance, the sum of the linear momentum and the sum of the angular momentum of all manipulator elements needs to be constant, dynamic balance is all about similar opposite motion of masses and inertias. This means that from a kinematic point of view elements need to counter-rotate and to counter-move with respect to one another. The more the motions are similar and opposite, the better the balanced solution can be.”* [24] The DUAL-V design is built from two force-balanced pantographs. To recognize the pantograph linkage in this manipulator it is important to mention that the pantograph is pulled apart. As long as the links remain parallel to one another this does not influence the balance. The moment balance is obtained by using the same structure twice, so this structure can make opposite and equal rotations so that combined no reaction moments exist. This has the downside that it is not perfectly balanced for motions with a rotated platform or not on the orthogonal axes. This design shows the importance of opposite rotations and on the other hand, also shows that it is not always necessary to have perfect balance. Operating in the vicinity of perfect balance could already improve the performance of the manipulator.

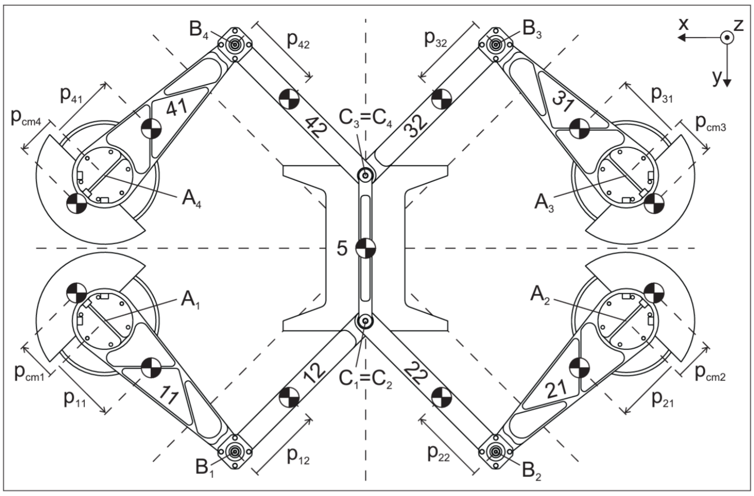

Figure C.1: Design drawing of a DUAL-V prototype manipulator. Source: [24]

Another example is the Super-B, presented in [20], a 2 DoF planar manipulator designed for manipulation at high speeds. This manipulator is balanced due to its constant inertia mechanism which is actuated by two inverted four-bar linkages. The inverted four-bar is a 1 DoF inherently balanced mechanism. The balance conditions for this mechanism are first presented in [25]. A practical design and experimental evaluation of such an inverted four-bar is presented in [26], and the design presented in this work is shown in Figure C.3. This structure uses the counter rotations that are inherently present in the kinematics to moment balance it. To do this the dimensions and properties of the links have to be selected carefully. A downside of this configuration is that it only allows for a limited range of motion, the example shown has an admissible range of 50 degrees [26].

From these examples, it becomes clear that inherent moment balance comes down to nothing else than having opposite rotations present in the kinematics at the same time. The examples also show that once one needs a two DoF manipulator the common approach is to get there by combining multiple linkages. Trying to find a 2-DoF solution that consists of one single structure could reduce the weight of the solution which would be very beneficial for the application in a flying manipulator. Improving the range of motion is another issue, as the aim of the flying manipulator is to be able to manipulate omnidirectionally. In the next sections, three ideas that were derived from these examples will presented.

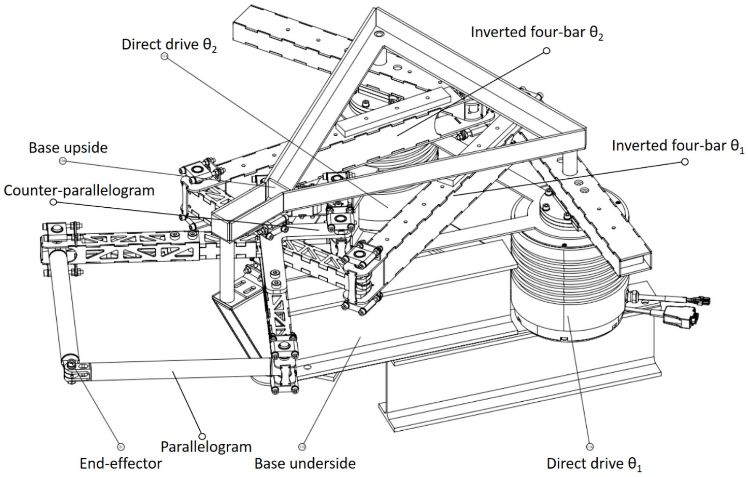

Figure C.2: Design drawing of the Super-B inherently balanced manipulator. Source: [20]

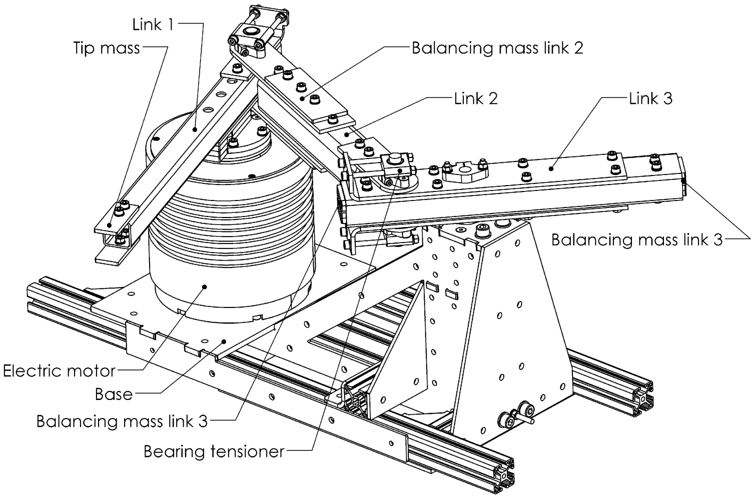

Figure C.3: Design drawing of the inverted four-bar as presented in [26].

C.2. 5-bar-concept

Reviewing the existing manipulators has led to an idea for a 2-DoF inherently balanced manipulator. The inverted four-bar is the main inspiration for this idea. It uses counter-rotating links present in the linkage to moment balance the motion. If this could also be applied to a 5-bar linkage, a moment-balanced 2-DoF manipulator can be formed. The workspace and kinematics are investigated first, to evaluate if such a mechanism is viable. A large and hopefully omnidirectional workspace is what is searched for.

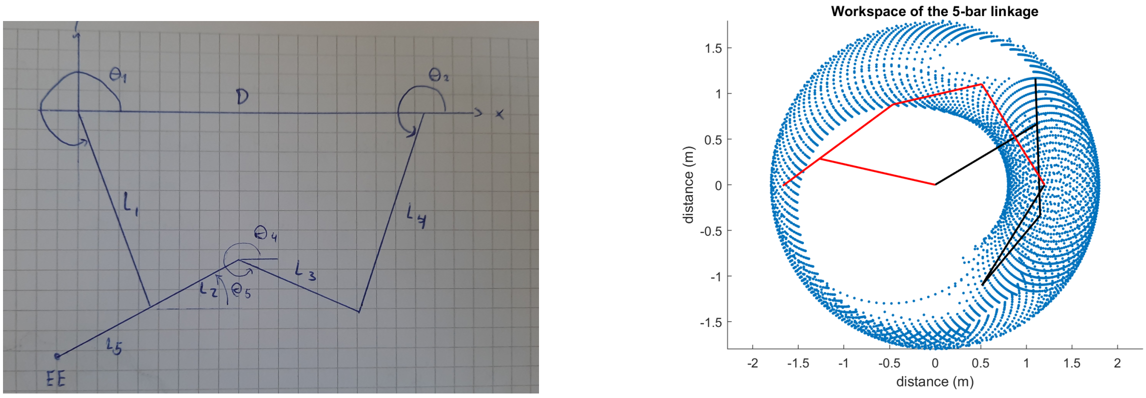

(a) Sketch of a 5 bar linkage with variable names

(b) Workspace of the 5 bar linkage visualized

Figure C.4

The link lengths are chosen by trial and error, to check if this concept would work this is sufficient. For an actual manipulator, it would be advised to pay more attention to the selection of link lengths as they heavily influence the kinematics. The link lengths are summarized in the Table C.1. The workspace of this linkage is displayed in Figure C.4b. The red and black linkages represent two different configurations to reach a point in the workspace. It is good to be aware that in practice maybe not all configurations can be used. For instance, practical constraints such as components interfering with each other, or the mechanism not being able to manipulate through a singularity position can constrain the achievable workspace. Later it will also become clear that the different configurations of the linkage form a problem for balancing it.

Table C.1: Lengths of the links of the 5-bar linkage

Link	Length (m)
L1	1.3
L2	1
L3	1
L4	1.3
L5	0.5
D	1.2

C.2.1. Force Balance

There are several ways to achieve force balancing in a 5-bar linkage. While it is always possible to balance each link individually, this approach is not preferred due to the weight it would add. Alternatively, a pantograph can be employed to replace a portion of the linkage, enabling the balancing of two links simultaneously. By doing so, the weight of the remaining distal link can be distributed between the pantograph and the remaining base link. Consequently, only one counter mass needs to be added to the base link, as the pantograph takes care of the rest of the balancing process.

C.2.2. Moment Balance

As mentioned previously, the aim is to achieve moment balance in the mechanisms by utilizing the counter-rotating links present in the system. However, not all configurations of the 5-bar linkage allow for this approach, as there are certain configurations/motions where all links rotate in the same direction. This limitation restricts the achievable workspace of manipulators that employ this concept.

Where the inverted four bar can be balanced by carefully choosing link lengths and inertia of the links, this is unfortunately not possible for the 5-bar. The fact that this 5-bar has two inputs means that there is no fixed relation between the links for a certain input. Both trajectories have different relations between the links and therefore other inertia values are required to moment balance the mechanism. A solution for this could be found in a changing inertia. Changing inertia could simply be done by changing the distance between masses and this has the benefit that it can be done in a balanced way. Because these masses can be moved in opposite directions.

In theory, this approach should work, but its practical feasibility needs to be evaluated by determining the required inertia for balancing a trajectory of the end-effector. For this evaluation, all the links are assumed to have a mass of 100 grams per meter of length. However, link L4 differs, as it will have a variable inertia consisting of two sliding masses, each weighing 250 grams. The centre of mass (COM) of link L4 is located in the middle of the link. The trajectory for this test is arbitrarily chosen and depicted by the red dotted line in Figure 5. The velocity profile is assumed as shown in Figure C.6a. The input angles and velocities are illustrated in Figure C.6b and C.6c, respectively. The inertia of link L4 can be determined using the angular momentum equation, as all other variables are known. The resulting contributions to the angular momentum of all the links are shown in Figure C.6d, where the plot demonstrates how the angular momentum contributions sum up to zero, indicating moment balance. Lastly, Figure C.6e illustrates the radius at which the masses of the variable inertia should be positioned. From this analysis, it can be concluded that although the masses have to be placed at a relatively large radius, the concept could potentially work in practice. This distance can be reduced by using heavier masses or by optimizing the kinematics. Unfortunately, the requirement of having links rotating in opposite directions at all times significantly reduces the workspace, making this concept unsuitable for an omni-directional workspace.

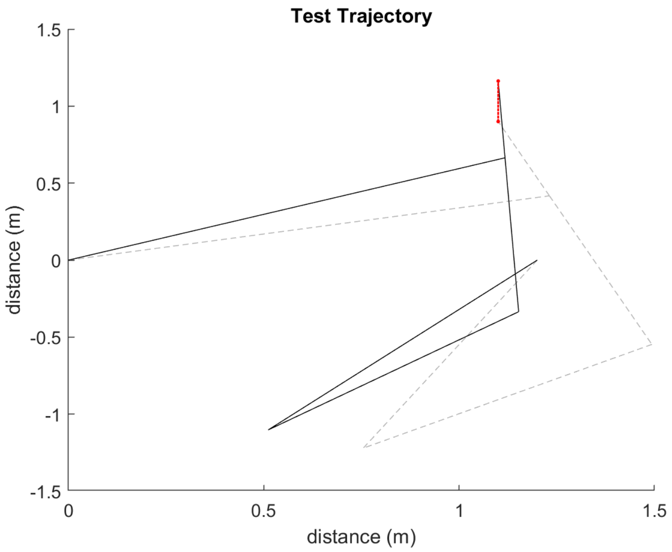

Figure C.5: Trajectory used to test the validity of the 5-bar concept.

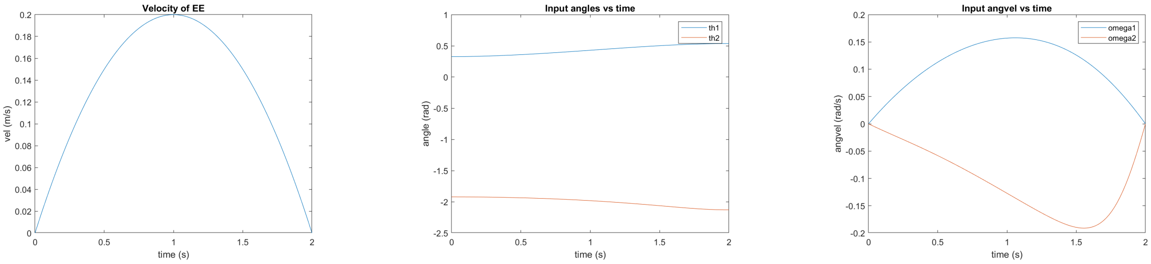

(a) Plot of the endeffector velocity

(b) Plot of the input angles

(c) Plot of the input angular velocities

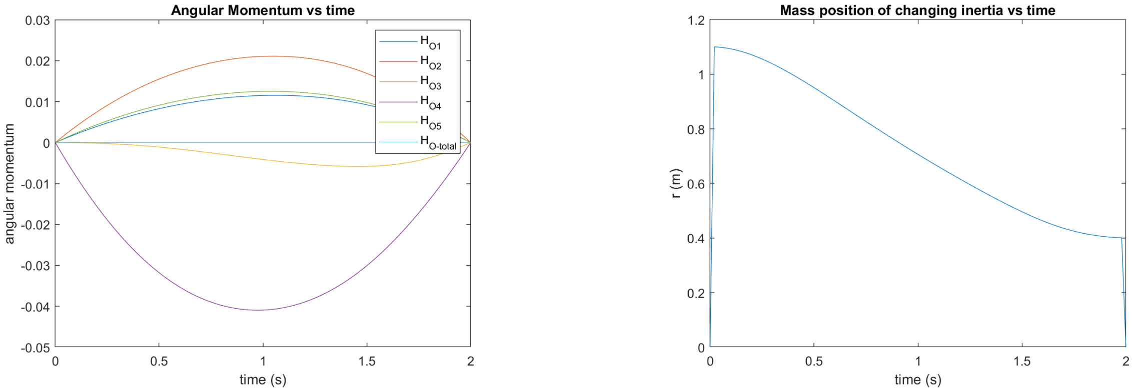

(d) Plot of the angular momentum contributions of the links

(e) Plot of the radius to the masses required for moment balance

Figure C.6

C.3. 6-Bar Concept

The 5-bar shown previously could not manipulate omnidirectionally (in a balanced way), due to the absence of counter-rotating links over the whole workspace. The aim for this concept is therefore to find a mechanism which always has a link rotating in the opposite direction as the input. A logical direction to proceed with is adding an extra link and seeing if this additional link makes it possible to find such a mechanism. After a quick search, a video of such a mechanism was found, see `https://www.youtube.com/watch?v=0TeNsu7HvjU`. The possibilities of moment balancing this mechanism will be explored in this section.

C.3.1. Kinematics

Figure C.7 shows a sketch of the linkage which will be investigated. This linkage has three fixed points, namely P1, P2 and P7, where P1 is placed in the origin O and the others are placed at positions which can be described by parameters L7, L8 and θ_6. In this evaluation θ_1 will be used as the input angle and all other angles can be defined as a function of this angle and the link lengths. These relations could be used to find the moment-balancing conditions of such a linkage. Unfortunately, these expressions become too complex to be insightful and therefore the moment balancing conditions are not derived.

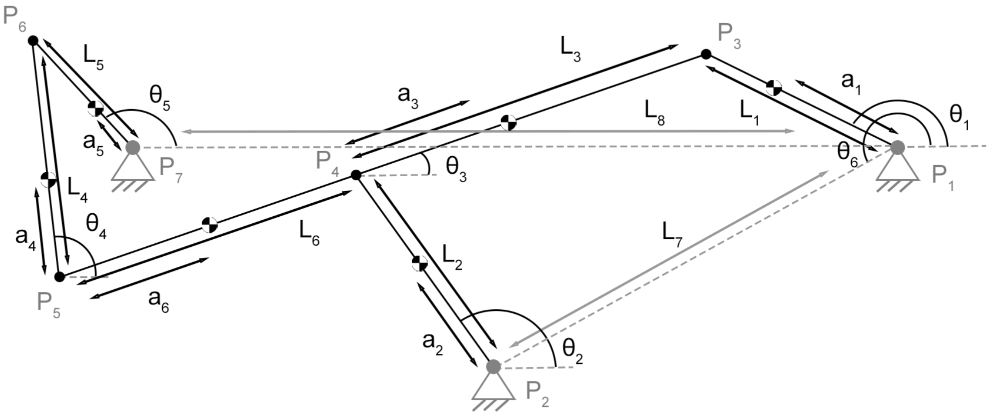

Figure C.7: Sketch of the 6bar defining the parameters

C.3.2. Moment Balancing

For a system to be moment balanced the angular momentum of the system has to remain constant, and for most systems, this practically means it has to remain zero. With algebraic angle relations the angular momentum could be written and from these relations forcing momentum balance could be studied. As mentioned previously this becomes too cumbersome for this mechanism and therefore another method, namely optimisation, is used to explore if this mechanism can become moment balanced.

The key to optimisation is finding a suitable objective function to feed to an optimisation algorithm. Such an objective function must output a number which indicates how well a certain set of input parameters performs. The convention is to minimize this objective function and therefore the objective function should be formulated such that the lower the output the better. In this optimisation, it is tried to find a configuration in which the 6-bar linkage is moment balanced over its workspace. Hence, the angular momentum around a point should be equal to zero. The objective function calculates at 100 points (linearly spaced over 2pi) the angular momentum of the mechanism around O and outputs the maximum value it obtained. Other functions could be implemented as well, for instance summing the absolute values. But the maximum value is used as this penalizes narrow peaks well. Narrow peaks would indicate large reaction forces which are particularly undesired.

The angles are determined with the circle intersection method as mentioned previously and the angular velocities are determined numerically using a central differencing scheme. These values are then used to evaluate the angular momentum equations, the equations are shown below. Unfortunately, this method was not able to find a balanced solution. However, this does not mean that the mechanism cant be moment-balanced.

$$H_{O1} = \left(I_1 + a_1^2 m_1\right) \frac{d}{dt}\theta_1(t) \tag{C.1}$$

$$\begin{aligned} H_{O2} = {} & (I_2 + m_2 (a_2 - l_2)(a_2 + l_1 \cos(\theta_1(t) - \theta_2(t)) - l_2 - l_3 \cos(\theta_2(t) - \theta_3(t)))) \frac{d}{dt}\theta_2(t) \\ & - l_3 m_2 (l_1 \cos(\theta_1(t) - \theta_3(t)) - l_3 + (a_2 - l_2) \cos(\theta_2(t) - \theta_3(t))) \frac{d}{dt}\theta_3(t) \\ & + l_1 m_2 (l_1 - l_3 \cos(\theta_1(t) - \theta_3(t)) + (a_2 - l_2) \cos(\theta_1(t) - \theta_2(t))) \frac{d}{dt}\theta_1(t) \end{aligned} \tag{C.2}$$

$$\begin{aligned} H_{O3} = {} & (I_3 + m_3 (a_3 - l_3)(a_3 + l_1 \cos(\theta_1(t) - \theta_3(t)) - l_3)) \frac{d}{dt}\theta_3(t) \\ & + l_1 m_3 (l_1 + (a_3 - l_3) \cos(\theta_1(t) - \theta_3(t))) \frac{d}{dt}\theta_1(t) \end{aligned} \tag{C.3}$$

$$\begin{aligned} H_{O4} = {} & (I_4 + a_4 m_4 (a_4 + l_1 \cos(\theta_1(t) - \theta_4(t)) - (l_3 + l_6) \cos(\theta_3(t) - \theta_4(t)))) \frac{d}{dt}\theta_4(t) \\ & - m_4 (l_3 + l_6)(a_4 \cos(\theta_3(t) - \theta_4(t)) + l_1 \cos(\theta_1(t) - \theta_3(t)) - l_3 - l_6) \frac{d}{dt}\theta_3(t) \\ & + l_1 m_4 (a_4 \cos(\theta_1(t) - \theta_4(t)) + l_1 - (l_3 + l_6) \cos(\theta_1(t) - \theta_3(t))) \frac{d}{dt}\theta_1(t) \end{aligned} \tag{C.4}$$

$$\begin{aligned} H_{O5} = {} & (I_5 + m_5(a_5 - l_5)(a_5 + l_1 \cos(\theta_1(t) - \theta_5(t)) + l_4 \cos(\theta_4(t) - \theta_5(t)) \\ & - l_5 - (l_3 + l_6) \cos(\theta_3(t) - \theta_5(t)))) \frac{d}{dt}\theta_5(t) \\ & + l_4 m_5 (l_1 \cos(\theta_1(t) - \theta_4(t)) + l_4 + (a_5 - l_5) \cos(\theta_4(t) - \theta_5(t)) \\ & - (l_3 + l_6) \cos(\theta_3(t) - \theta_4(t))) \frac{d}{dt}\theta_4(t) \\ & - m_5 (l_3 + l_6)(l_1 \cos(\theta_1(t) - \theta_3(t)) - l_3 + l_4 \cos(\theta_3(t) - \theta_4(t)) \\ & - l_6 + (a_5 - l_5) \cos(\theta_3(t) - \theta_5(t))) \frac{d}{dt}\theta_3(t) \\ & + l_1 m_5 (l_1 + l_4 \cos(\theta_1(t) - \theta_4(t)) + (a_5 - l_5) \cos(\theta_1(t) - \theta_5(t)) \\ & - (l_3 + l_6) \cos(\theta_1(t) - \theta_3(t))) \frac{d}{dt}\theta_1(t) \end{aligned} \tag{C.5}$$

$$\begin{aligned} H_{O6} = {} & (I_6 - m_6(-a_6 + l_3 + l_6)(a_6 + l_1 \cos(\theta_1(t) - \theta_3(t)) - l_3 - l_6)) \frac{d}{dt}\theta_3(t) \\ & + l1 m_6 (l_1 + (a_6 - l_3 - l_6) \cos(\theta_1(t) - \theta_3(t))) \frac{d}{dt}\theta_1(t) \end{aligned} \tag{C.6}$$

C.4. Double inverted four-bar with slider

Combining balanced linkages is a strategy that could be used to create higher DoF-balanced mechanisms. This concept uses two inverted four bars to manipulate an additional rod. In Figure C.8 the mechanism is displayed schematically. The rod, existing out of L_4 and L_8, is mounted with a revolute joint to one inverted four bar in point P_4. The rod is connected to the other inverted four-bar with a slider that can slide over link L_6. In this manner, the resulting mechanism has the required two DoFs. The mass of the added link can be incorporated into the balance of the inverted four-bar to which it is mounted with the revolute joint as long as the COM of the rod is located in point P_4. This makes it possible to force balance the mechanism, unfortunately, this is not the case for moment balance. The added link does not match the rotation of any existing link and therefore can not be included in the existing balance equation and must be balanced separately. To gain more insight into this idea and its balancing conditions, the balance conditions will be solved for a trial case and the workspace that can be obtained with this mechanism will be visualized.

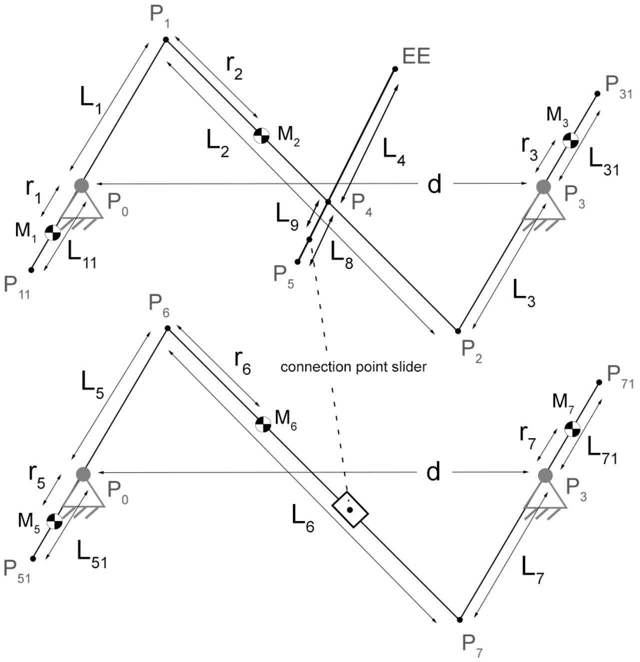

Figure C.8: Parameters of the inverted fourbar concept

C.4.1. Balancing a trial case

The balancing conditions of an inverted four-bar are first presented in [25], and a detailed derivation can be found in [27]. In the Figure C.8 a schematic overview of the mechanism is shown. The length of link i is denoted by L_i. L4 and L8 form the added link, the COM of this link will be placed in point P_4 to account for it in the balancing conditions. The links in this example case are all made of aluminium tubing with an outer diameter of 10mm and a wall thickness of 1mm, with a mass per unit length of $76.3500\ g/m$. The balancing masses are made of brass with a density of $8500\ kg/m^3$. The link lengths used for this trial case are displayed in Table C.2. The balancing masses placed at links l1, l3, l5 and l7 are shaped such that these links have their COM at the right place as well as the correct inertia to have a balanced mechanism. The balanced mechanism has a total weight of 416.41 grams. The obtained mechanism including the mass of the counter masses is presented in Figure C.9, together with the other parameters. The values followed by a * are calculated by the balancing equations shown below. The shown manipulator does not yet include a counter inertia to balance the link formed by l4 and l8.

$$L_3 = L_1 \tag{C.7}$$

Table C.2: Dimensions of the inverted four-bar trial case. * denotes calculated values determined by the balance conditions.

Link	Length (m)
L_1	0.10
L_2	0.30
L_3	0.10*
L_4	0.20
L_5	0.10
L_6	0.30*
L_7	0.10*
L_8	0.05
L_9	0.025
d	0.30*

Link	Length (m)
L_{11}	0.10
L_{31}	0.10
L_{51}	0.10
L_{71}	0.10
r_1	0.035311875*
r_2	0.15
r_3	0.035311875*
r_4	0.022905*
r_5	0.15
r_6	0.022905*

M_i	Mass (g)
M_1	100
M_2	70.62...*
M_3	100
M_4	50
M_5	22.90...*
M_6	50

k_i	Radius (m)
k_1	0.07625907...*
k_2	0.08660254...
k_3	0.07625907...*
k_5	0.06368956...*
k_6	0.08660254...
k_7	0.06368956...*

$$d = L_2 \tag{C.8}$$

$$L_6 = L_1 \tag{C.9}$$

$$L_7 = L_5 \tag{C.10}$$

$$r_1 = \frac{L_1 * L_2 * m_2 - r_2 * L_1 * m_2}{m_1 * L_2} \tag{C.11}$$

$$r_3 = \frac{L_1 * m_2 * r_2}{m_3 * L_2} \tag{C.12}$$

$$r_5 = \frac{L_5 * L_6 * m_6 - r_6 * L_5 * m_6}{m_5 * L_6} \tag{C.13}$$

$$r_7 = \frac{L_5 * m_6 * r_6}{m_7 * L_6} \tag{C.14}$$

$$I_1 = m_2 * ((L_2 * r_2 - (r_2^2)) - (k_2^2)) \tag{C.15}$$

$$k_3 = \sqrt{-(L_3 * r_3 + (r_3^2)) + (I_1/m_3)} \tag{C.16}$$

$$k_1 = \sqrt{((I_1/m_1) - (r_1^2) - (r_1 * L_1))} \tag{C.17}$$

$$I_5 = m_6 * ((L_6 * r_6 - (r_6^2)) - (k_6^2)) \tag{C.18}$$

$$k_7 = \sqrt{-(L_7 * r_7 + (r_7^2)) + (I_5/m_7)} \tag{C.19}$$

$$k_5 = \sqrt{((I_5/m_5) - (r_5^2) - (r_5 * L_5))} \tag{C.20}$$

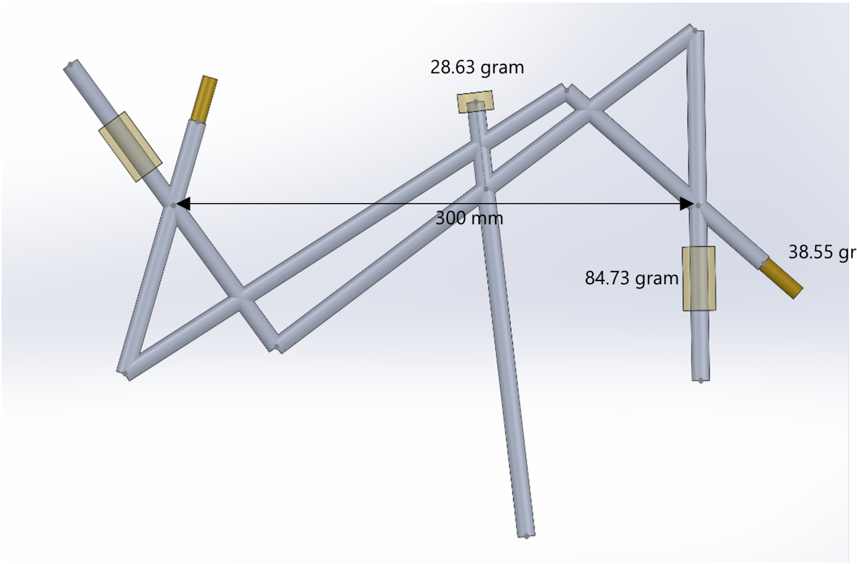

Figure C.9: Trial case of a force balanced and partially balanced double inverted 4 bar two DoF manipulator.

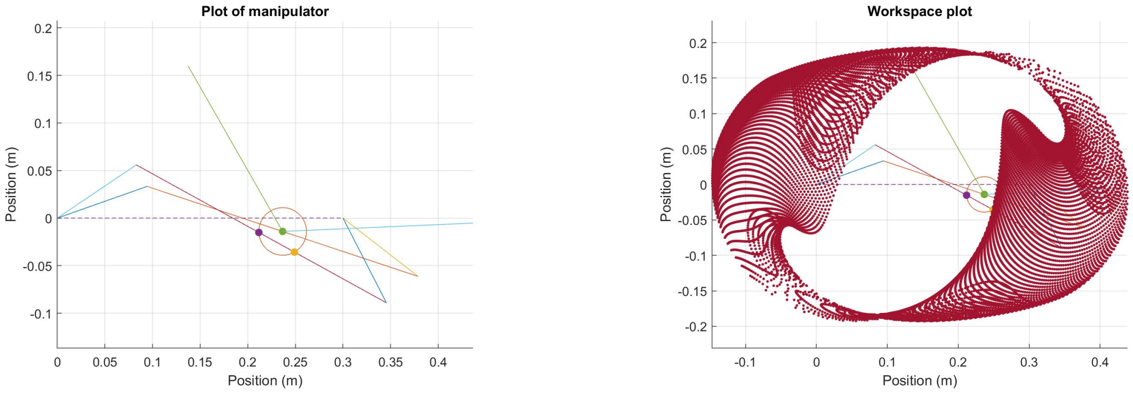

(a) Plot of mechanism showing the kinematics

(b) Workspace of the manipulator as shown in Figure C.9

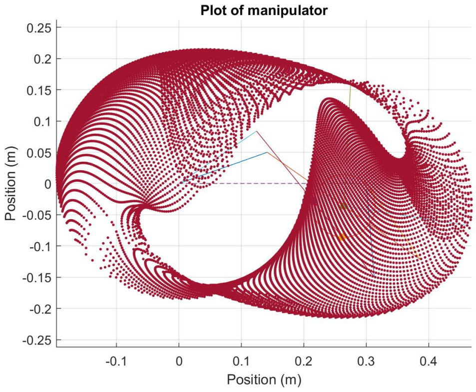

(c) Workspace the manipulator with changed link lengths, l1 = l3 = l5 = l7 = 0.15m and l9 = 0.05m.

Figure C.10: Plots of the manipulator and its workspace

C.4.2. Workspace of the manipulator

Another important aspect of the flying manipulator is its workspace. For this concept, it is intuitively not easy to predict what its workspace will look like. To make sure the workspace of such a manipulator is practically useful the position of the end-effector is determined numerically using the circle intersection method, a graphical representation can be seen in Figure C.10a. By varying the input angles of link L_1 and L_5 the workspace is visualized, the resulting plots can be seen below. In Figure C.10b the workspace of the manipulator as shown in Figure C.9 is plotted and in Figure C.10c the workspace is plotted when the links $L1$, L_3, L_5 and L_7 are increased in length to 0.15 (m) and L_9 is changed to 0.05 (m). This case is just to show that the workspace can be changed drastically by choosing different lengths.

C.4.3. Conclusion

The previous results are promising and show that a 2 DoF manipulator can be made using this concept. The workspace could be improved especially right above and below the manipulator has not much room to manipulate. Nevertheless, the plotted workspace is omnidirectional and could for instance be used for pick and place operations where it manipulates an object from one side to the other. The balanced example shows that the inverted four-bar mechanism can be balanced with counterweights of a reasonable mass compared to the added link. Balancing the moments generated by this added link show to be difficult as the rotation with respect to the fixed base needs to be compensated and this means that the counter ineratia can not simply rotate relative to link L_2. The biggest issue this concept has is the two rigid mounting points. The link L_4 + L_8 needs to move through these points. In practice, on both sides of the manipulator, a frame for the drone is required. For structural reasons, it is necessary to have at least one of the points P0 or P3 pass through the midplane (where the manipulator is located) and connect the two halves of the frame. Unfortunately, this will limit the workspace.

D

Measuring motor inertia

To fully balance a mechanism the mass and inertia of all components must be considered. For most parts, these parameters can be obtained by modelling them in CAD software. As a sanity check the mass can be used, as this is easily measurable on an accurate scale, once the actual mass matches the mass coming from the model the inertia can be trusted. Unfortunately doing this for the actuators is a bit more tricky. For this project, Dynamixel servo motors will be used of type XL-430-250-t. These actuators are reasonably well documented, but unfortunately, the inertia associated with the rotor of this motor is not given by the manufacturer. The CAD modelling approach is complicated because details about internal components are not provided. Therefore another approach had to be sought, to evaluate this property. In the next section, the setup that is constructed will be explained and the results are shown and discussed.

D.1. Setup

The goal of this measurement is to find the inertia of the motor to be able to account for it while balancing the manipulator so that in the end no reaction forces and moments are present. This forms also to basis for this experiment. While the motor is unbalanced it should produce a reaction moment once it accelerates. If the reaction moment is measured and the acceleration is known the inertia can be calculated. The setup shown in Figure D.2a is made to make this measurement possible. A stiff beam to which the motor is attached is supported by bearings to remove friction for a large part. The beam is extended to be able to balance the weight of the motor, such that the COM is almost in the centre of the support axle. Otherwise, the loadcell which is placed at the end of the stiff beam would not only measure the force due to the reaction moment but also the force coming from the mass of the motor and the beam. This is not necessarily an issue because theoretically, this would only lead to a systematic error which can be corrected for. However, in practise an accurate load cell needs to be used to measure which has a certain measurement range, which would be exceeded if the beam would not be balanced. To remove any effects from play in the setup, the beam was balanced such that the load cell was pre-compressed but had enough margin to not reach its limits. On the other hand, the acceleration of the motor needs to be controlled or measured. For the sake of ease, it was chosen to use the built-in acceleration control of the Dynamixel motor.

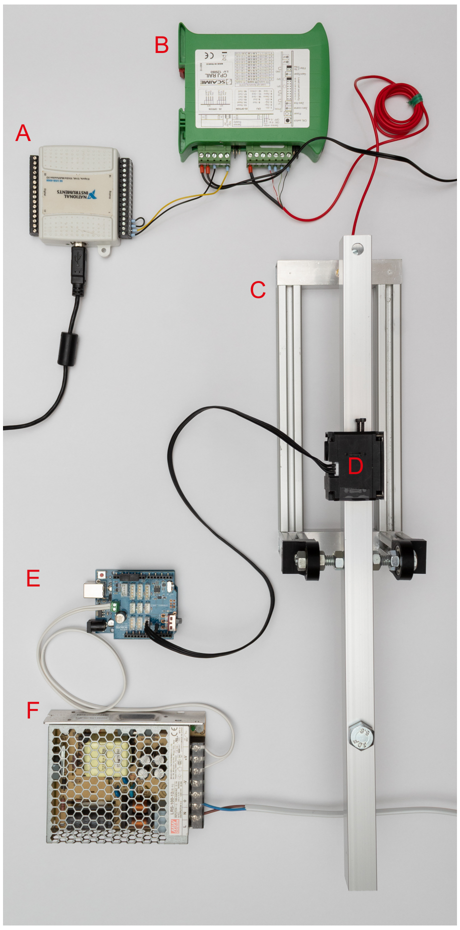

Figure D.1: Caption

The components that are used for this setup are shown in Figure D.1. The Dynamixel XL-430-250-t actuator, denoted by the letter D in the figure, is controlled with the help of a Dynamixel shield for the Arduino microcontroller (E). The motor was supplied with power by a DC-DC converter (F). The setup (C) is in more detail shown in Figure D.2a and D.2. The loadcell used in this setup is the Futek LSB200 with a 20g capacity. The loadcell is connected to a Scaime CPJ analog signal conditioner (B). The data is logged using a NI USB-6008 DAQ device (A), which sampled the signal every 10 ms. The measurement is performed for the following angular accelerations shown in Table D.1. The measurement is repeated ten times at every acceleration.

Table D.1: Angular acceleration used for the measurements.

Dynamixel Units	rad/s^2
10	3.745075149051873
20	7.490150298103745
30	11.235225447155617
40	14.980300596207490
50	18.725375745259363
70	26.215526043363106
100	37.450751490518726

D.2. Results and Discussion

The recorded data is presented in Figure D.3, for every acceleration only the first measurement is shown. The presented measurement is already corrected for the offset, this is done by calculating

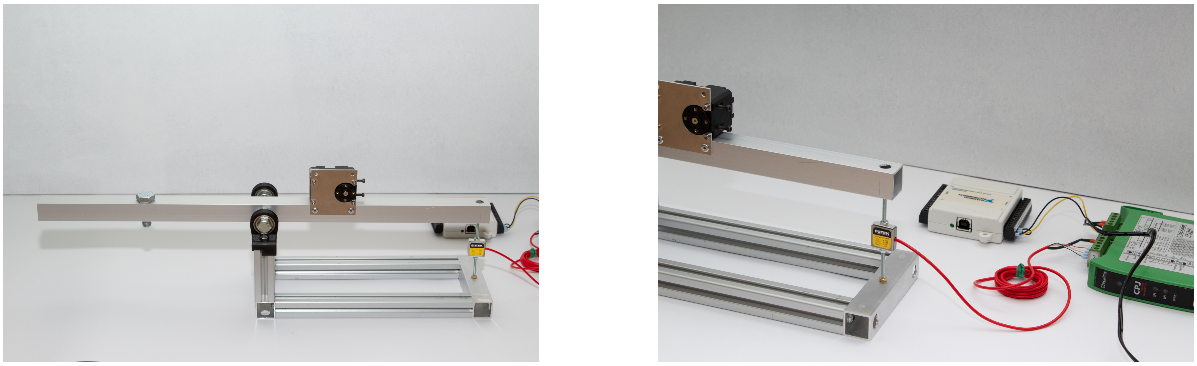

(a) Caption for the first right image.

(b) Caption for the second right image.

Figure D.2: Main caption for the entire figure.

the average of the obtained measurement and subtracting this value from every data point. All plots generally show the same, first a force close to zero as the system was in equilibrium, then a small bump caused by pressing a button to start the microcontroller to control the motor. After a while, the motor starts accelerating and the force goes up. The acceleration is constant so the measured force should be constant as well. The servo motor performed only one rotation so also had to slow down during the measurement and did this with the same deceleration. For the higher acceleration, these two phases are separated by a period of force measurements being close to zero. Here the maximum speed of the motor was reached and moving at a constant angular velocity does not produce any reaction forces. For the high acceleration measurements, two things can be noticed in the deceleration phase. First, these peaks become narrower and higher, this seems to come from a much more abrupt deceleration. Although it is not verified it seems that the controller is not able to control this well. A theory for this could be that once the controller decelerates fast, the output does not follow this directly because it first moves through the play in the system and then creates a spike because the output comes into contact with the gears and has to change its speed more or less instantaneously. Secondly, some of these peaks are not measured, see for instance Figure D.3g, because the measurement got saturated. Once this was noticed the following measurements were performed further away from this point to avoid saturation in these measurements. However, this phase will be discarded for the determination of the reaction forces because of the first observation, therefore the measurements containing the saturation effect are not redone.

The data processing started with applying a Gaussian-weighted average filter, with a window size of 10 samples to the left and to the right of the sample point. The maximum force from the smoothed data is determined and from this, a threshold of $0.8 * max$ is constructed. This threshold is used to select a section from the data, this section satisfies that the smoothed data is larger than the threshold. The actual data in this section is average and the outcome of this represents the reaction force due to the acceleration of the motor. In Figure D.4, this is visually represented. So first the selection is made based on the smoothed data (orange line) being higher than the solid horizontal line. For all blue data points in this area, the average is determined, and the resulting value is represented by the dotted line in the figure.

This is done for all measurements and the outcome is shown in Figure D.5. The two lines that are plotted are constructed by applying linear least squares regression on the data points. The orange line uses all data points and the yellow line excludes the data points corresponding to the acceleration of $37.45 rad/s^2$. These were excluded while the method used seems to be not as well suited for the narrow peaks. Figure D.6 shows that the method seems to underestimate the reaction force. This results in a line which passes more closely through the origin, which is a sign that excluding the measurements at the highest acceleration yields a better prediction of the reaction force. The reaction moments can be calculated from the measured reaction forces due to the known distance between the axle and the loadcell of $220(mm)$. So the slope of the line represents the force per unit of acceleration, $6.04975278738212 * 10^{-5}(N/214.577(rev/min^2))$. To convert the force to a moment this number is simply multiplied by the moment arm, which results in $1.330945613224067 * 10^{-5}(Nm/214.577(rev/min^2))$. This can be expressed as $3.553855557640861 * 10^{-5}(Nm/(rad/s^2))$

, which equals to $3.553855557640861 * 10^{-5} (kg \cdot m^2)$.

D.3. Conclusion

The experiment that was performed aimed to measure the inertia of the motor by measuring the reaction moment by a prescribed angular acceleration. By the angular analogue of Newton's second law, Equation D.1, the inertia can be determined. The obtained inertia is 3.55×10^{-5} kg m^2.

$$\sum \tau = I * \alpha \tag{D.1}$$

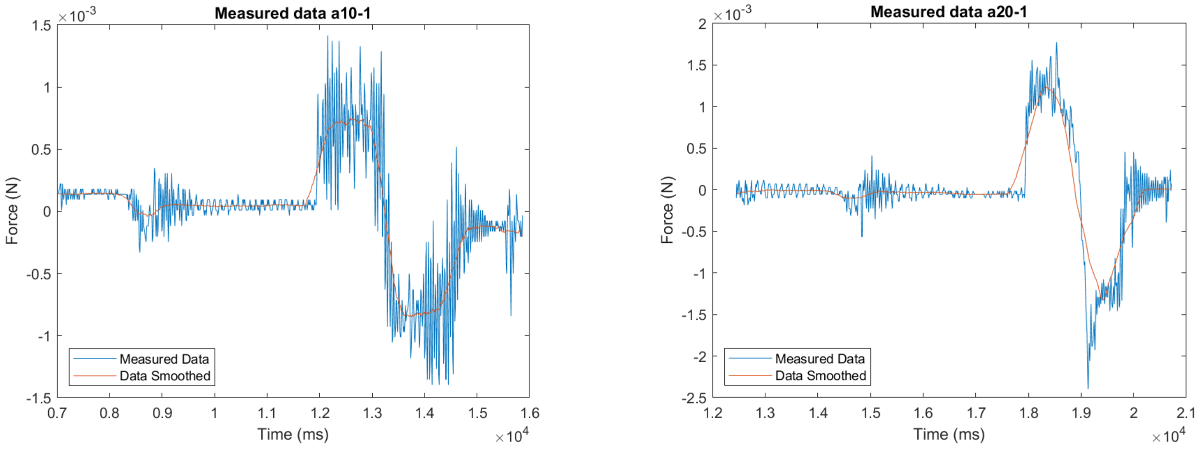

(a) Measurement data with acceleration of 3.75 rad/s^2.

(b) Measurement data with acceleration of 7.49 rad/s^2.

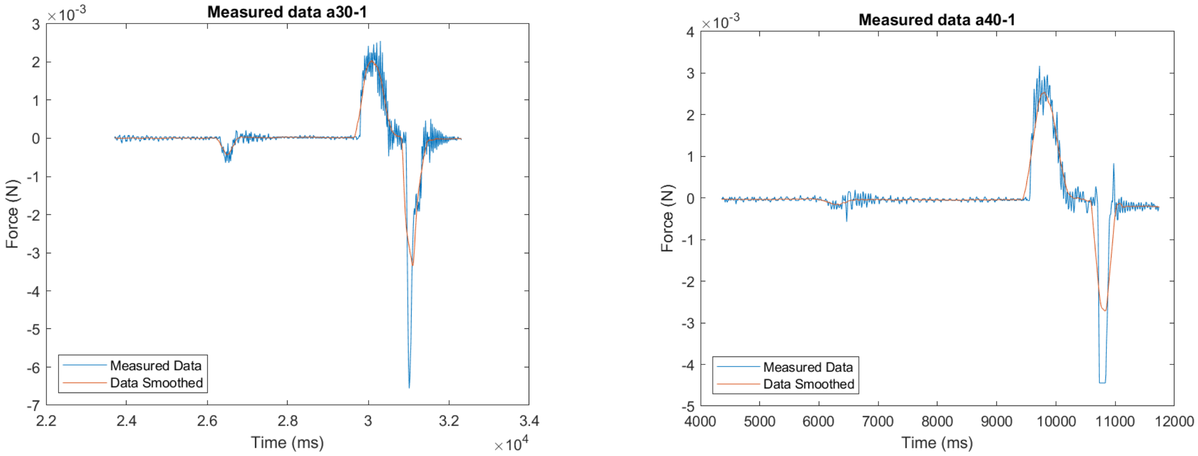

(c) Measurement data with acceleration of 11.24 rad/s^2.

(d) Measurement data with acceleration of 14.98 rad/s^2.

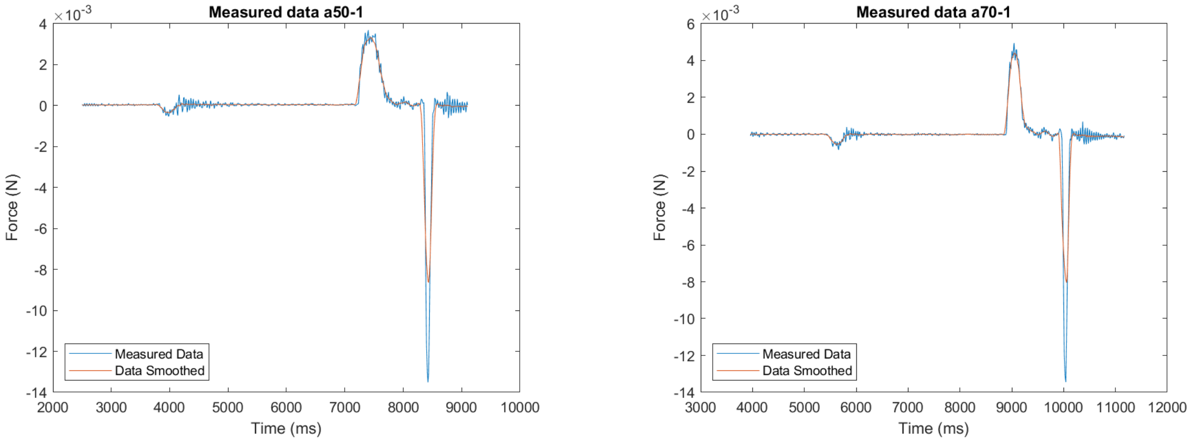

(e) Measurement data with acceleration of 18.73 rad/s^2.

(f) Measurement data with acceleration of 26.22 rad/s^2.

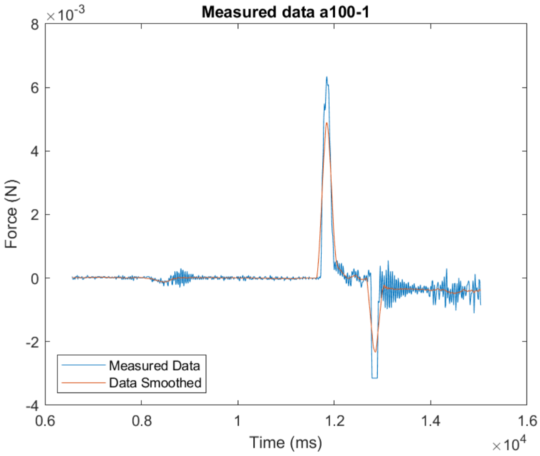

(g) Measurement data with acceleration of 37.45 rad/s^2.

Figure D.3: Plots of the recorded forces.

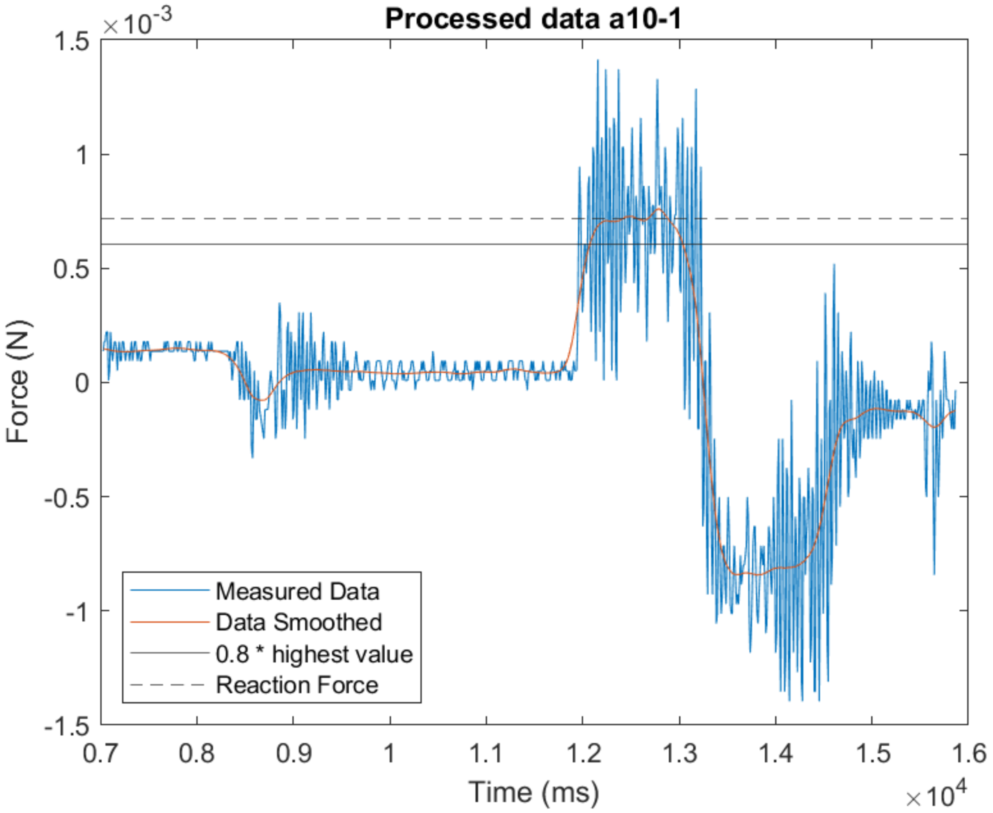

Figure D.4: Visual representation of the data processing.

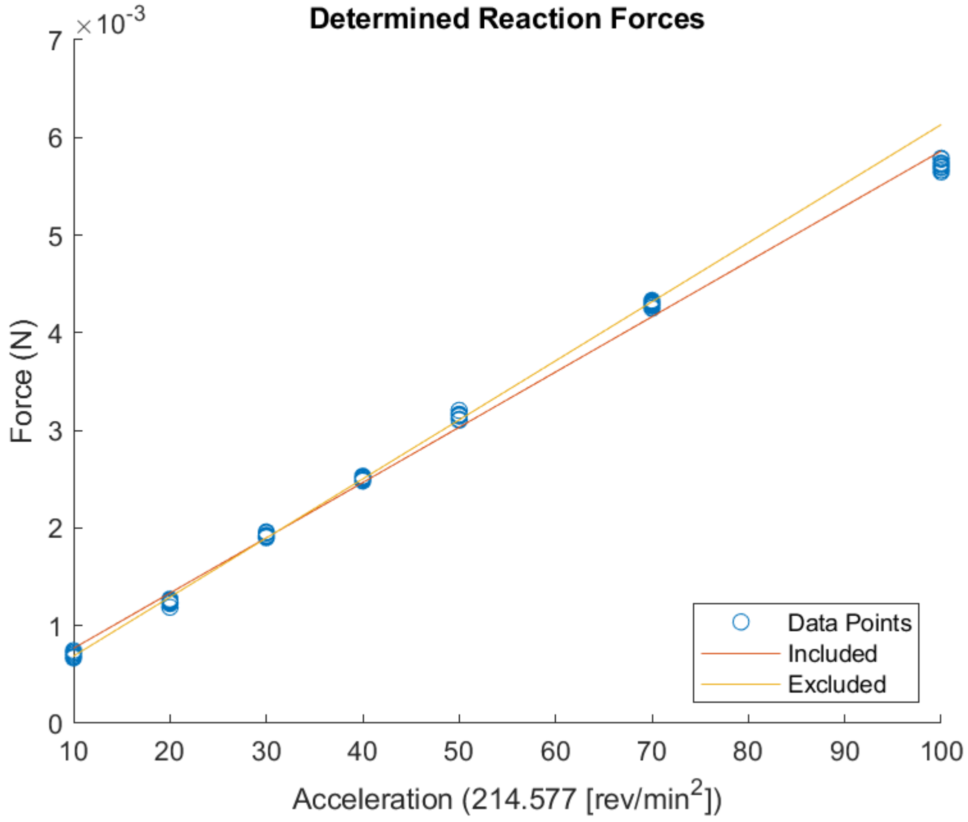

Figure D.5: The reaction forces extracted from the measurements.

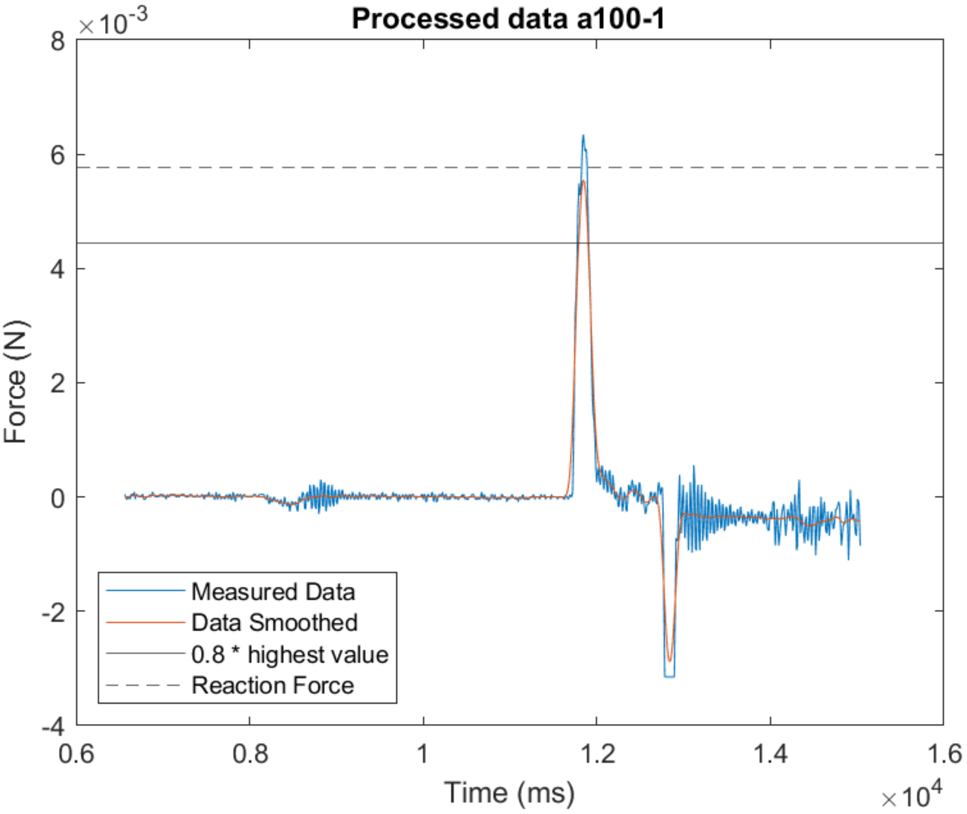

Figure D.6: Processed data for a measurement performed with an acceleration of $37.45 rad/s^2$.

E

Reaction Force measurement

As detailed in Chapter Three, capturing the reaction forces proved challenging, leading to the development of multiple setups before reaching the final configuration. This appendix will delve into the construction of these setups, providing an overview of their designs and showcasing the measurements obtained from the setup preceding the final iteration. Additionally, the simulations conducted will be explained.

E.1. Measurement setup

The manipulator's design is planar and therefore the in-plane forces are of interest to assess how well the manipulator is balanced. This limits the requirement for the setup to measure only two forces and one moment. Measuring these forces is however easier said than done. Initially, the setup was supposed to measure these in-plane forces using an ATI mini 45 six-axis force-torque sensor, see Figure E.1. The manipulator would be mounted rigidly to this sensor and the sensor would record the reaction forces during movement of the manipulator. Unfortunately, it turned out that the ATI mini sensor was not in a condition in which it was able to take measurements. Along with the concern that the sensor's resolution would be to course, this plan was discarded.

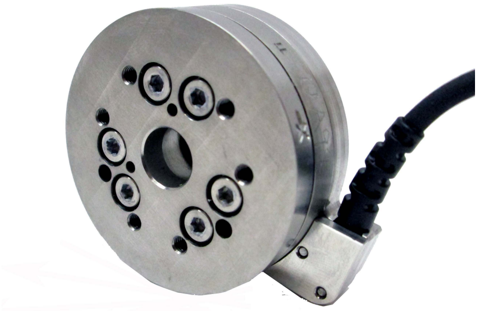

Figure E.1: ATI mini 45 sensor, source: `https://www.ati-ia.com/products/ft/ft_models.aspx?id=mini45`

Given the resources available the other approach had to use loadcells which can be borrowed from the measurement lab located at the 3Me faculty. The measurement of the forces in the x direction should not constrain the motion in the y direction and vice versa, to accurately measure these forces. To do this a suspended setup was devised. The manipulator is suspended from three loadcells, which measure the forces in the y direction. The moment can be calculated from the loadcell measurements as the location at which the force acts is known. A fourth loadcell would be placed to measure the force in the x direction. This sensor should be placed at the same height as P_0 so it would not be influenced by the reaction moment. The sensor should be mounted to the manipulator rigidly in the axial direction but should not constrain other movements. The sensor to measure the force in x direction would heavily complicate the setup and was therefore discarded. The idea was to first measure the force in the y direction and the reaction moment, and if time would allow the setup would be extended.

The setup was built as described and a picture of this setup is shown in Figure E.2. Unfortunately, the frame which can be mounted to the manipulator to serve as a stand makes this picture slightly confusing. The manipulator is freely suspended in this picture, the stand is not connected and is placed behind the manipulator. This setup showed to have two flaws, which influenced the measurement. The y-direction, the rotation around the x and the rotation around the z-axis are constrained. The manipulator is therefore free to make a swaying motion, which could be excited by external factors or the reaction forces. The swaying motion itself introduces reaction forces which disturb the measurement. The other flaw is the stiffness of the setup. Stiffness is required to pick up quick changes in the measurement. The long cables and especially the connections add compliance to the setup which is undesired. To improve upon both shortcomings the setup is changed once more.

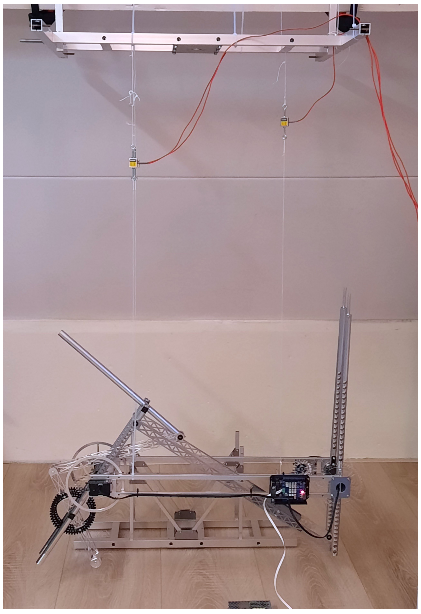

Figure E.2: Suspended setup reaction force measurement

Finally, the setup as it was used for the experiments in this appendix can be described. This is thus not the setup as shown in chapter three, the setup as used in chapter three is the next iteration of the setup presented here, benefiting from the gained experience. The manipulator was this time placed on top of the three loadcells, loading them in compression. This allowed removing the compliant ropes and replacing them with relatively stiff aluminium parts. In Figure E.3 the sensor placement is visualised, mounting sensor two required a custom aluminium part not shown in this figure.

An overview of the setup is shown in Figure E.4. On the left, an aluminium stand for the manipulator is repurposed to mount sensors one and three. Sensor two is mounted to a square aluminium profile, and combined with a vice, the sensor was mounted rigidly with room for adjustment to level the manipulator. A close-up showing how the sensors are mounted is presented in **??**. The load cells, to be specific FUTEK LSB 200 FSH00093, have a maximum load capacity of $22.2N$ which is required to support the weight of the manipulator. These loadcells were connected to Scaime CPJ strain gauge conditioners, and the outputted signals were recorded with an NI USB 6002 DAQ device using Labview every $10ms$. The manipulator's actuators are controlled by a Dynamixel shield attached to an Arduino Uno.

The manipulator consists of two inverted four-bar mechanisms, one of these inverted four-bars (links 4, 5 & 6) is mounted on a link (link 3) of the other inverted four-bar (link 1, 2 & 3). The inverted four-bar mechanism consisting of links four, five and six is fully dynamically balanced. The other inverted four-bar is due to a miscalculation not entirely moment balance. To verify this difference the experiment is split into two. The first experiment measures the reaction forces once θ_1 moves from $270°$ to $330°$. θ_1 accelerates the first half of its trajectory with an angular acceleration of $11.24\,\mathrm{rad\,s^{-2}}$ and then decelerates at the same rate until it travelled $60°$. Although the location of θ_4 should not influence this

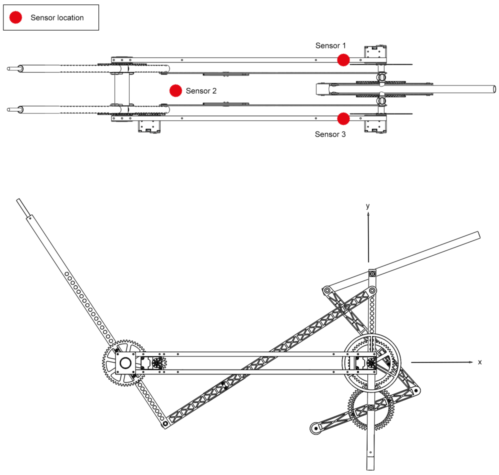

Figure E.3: Schematic overview of sensor placement measurement setup

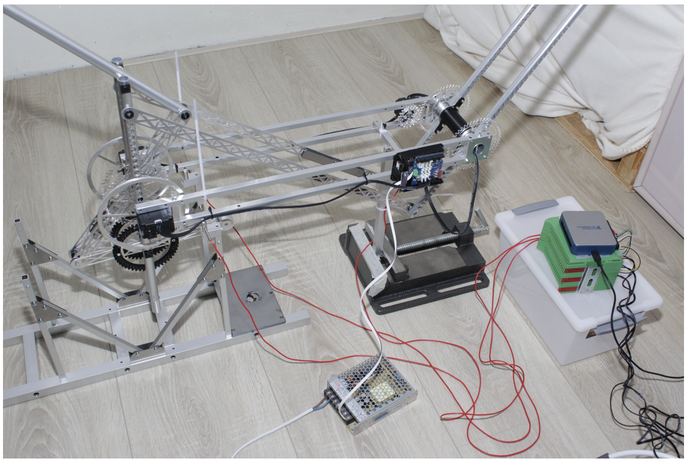

Figure E.4: Overview of experimental setup

measurement for the sake of completeness, θ_4 was calibrated to an angle of $0°$ once $\theta_3 = 90°$. This experiment is expected to show a reaction moment.

The second experiment measures the reaction forces once solely θ_4 is moved. Initially $\theta_4 = 0°$ and $\theta_3 = 90^{\circ}$. During the measurement θ_4 move $45°$, the first half it accelerates and the last half it decelerates, both at a constant rate of $11.24\,\mathrm{rad\,s^{-2}}$. The acceleration of the motor is controlled by the internal controller of the actuator used. The acceleration rate used corresponds to an acceleration of 30 in the units used by the motor controller. This rate is fairly conservative, to avoid the controller of the motor not being able to follow the desired trajectory.

E.2. Spacar simulation

Before the experiments were executed the reaction forces due to the movement of the manipulator were simulated. These simulations predict the outcome of the experiment and are used as a reference for the experimental data. As described in the previous section the experiment was split up in two, of course, the simulation matches this. The mechanism is modelled in a multibody simulation software package called SPACAR. The links of the inverted four-bar were modelled as planar beams with lengths as shown in Table E.1. For each link an additional planar beam was added, this beam has a length corresponding to the distance to the COM of the link. By doing this two nodes are created both positioned at the COM of the link, one describing the position and one the rotation of the link. The inertia and mass parameters of the link are assigned to these nodes. Table E.2 shows the parameters

(a) Sensor 1

(b) Sensor 2

Figure E.5: Close up showing how the sensors are mounted.

used in the simulation, and the variable a_i describes the position of the COM of mass on the link. The inertia shown is the inertia of the respective link around their COM, the inertia of link three is thus the inertia contribution of this link without the inertia of links four, five and six. For links two, five and six the values can directly be found from the CAD model. For links one, three and four this is not the case. The actuators and the geared connections are not modelled and therefore their inertia must be incorporated into these links.

If link one moves, the actuator always moves in the opposite direction with a gear ratio of 2.5. This means that the reduced inertia associated with this movement is simply the inertia of the link minus 2.5 times the inertia of the actuator and the inertia of the gear that is mounted to the actuator. In Table E.3 the inertia of the motor and the gear are presented, along with the actual inertia of link one and the adjusted value as used in the SPACAR simulation.

For links four and three care must be taken to account for the inertia correctly. Link four uses the counter-rotating actuator to ensure balance by enlarging the inertia associated with the actuator. The inertia of link four can simply be modelled as the inertia of the link subtracting the inertia of the actuator assembly. The actuator assembly consists of the actuator, an aluminium shaft, a drive gear and an aluminium disk to increase the inertia. Note that two actuators are used to drive this link, so the inertia of this assembly has to be subtracted twice to account for both. Once solely the inverted four bar consisting of links four, five and six moves the actuator and the link will always move with a ratio of -1 which makes this modelling choice valid. Once solely θ_1 moves link four moves as well but the actuators associated with θ_4 do not. Therefore the actual inertia of link 4 must be considered, this can be done by incorporating this inertia in the inertia term of link 3. But due to the geared connection to link four the angle θ_4 does not change similar to θ_3 but with $2\dot{\theta}_3 = \dot{\theta}_4$. To compensate for this the inertia that was fictively subtracted from link four has to be added to link four twice. In Table E.3 the inertia values of links three and four are shown, the actual value represents the physical value extracted from the CAD model. The Spacar value represents the value used for the simulation to incorporate the actuator and geared connection as described above.

Table E.1: Link lengths

Variable	Value
l_1	0.1625000
l_2	0.5509375
l_3	0.1625000
l_4	0.1078125
l_5	0.3000000
l_6	0.1078125
d	0.5509375
l_{10}	-0.1000000
l_9	0.2546875

Table E.2: Mass and Inertia

Variable	Value
a_6	59.5793e-3
m_6	45.1191e-3
I_6	534382.3268e-9
a_5	118.0681e-3
m_5	63.3542e-3
I_5	376511.5991e-9
a_4	47.7414e-3
m_4	86.7634e-3
I_4	340021.8417e-9
a_3	73.2642e-3
m_3	177.3227e-3
I_3	4274971.3424e-9
a_2	191.5927e-3
m_2	203.4946e-3
I_2	2486752.7520e-9
a_1	119.2496e-3
m_1	180.8666e-3
I_1	5446560.2187e-9

Table E.3: Adapted values for simulation to include actuators and gears

Variable	Actual Value	Spacar Value
$I_{actuator}$	3.55e-5	-
I_{gear} (θ_1)	735.2874e-9	-
I_1	5537148.4372e-9	5446560.2187e-9
$I_{actuator-assembly}$	1.5256e-4	-
I_4	645138.9245e-9	340021.8417098380e-9
I_3	3664737.1768e-9	4274971.3424e-9

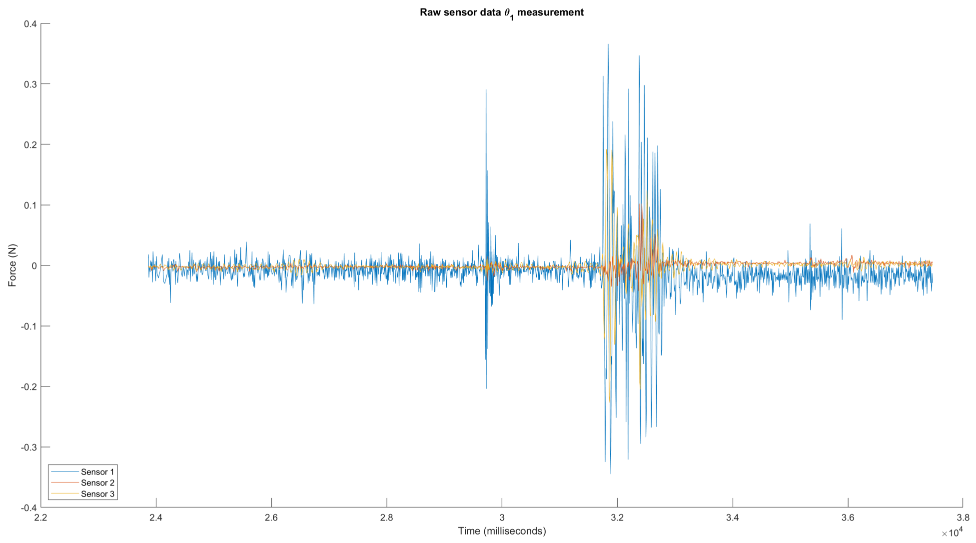

Figure E.6: Raw forces measured due to moving θ_1

E.3. Experimental results

The data obtained with the experiments is processed with Matlab, in this section, this data will be presented. Starting with the results from the first measurement. In this first experiment, θ_1 moved from $270°$ to $330°$. As described in the setup the data was obtained by three loadcells. Labview processed the recorded signal and calculated the force based on the measured voltage. An offset is used to correct for the weight of the manipulator which preloads the sensors. Before the measurement, the offset of each load cell was tuned such that the sensor's output was zero newton. In Figure E.6 the obtained data is shown. The data was recorded well before the motion of the manipulator started, this explains the first part of this plot until 31500 milliseconds. After this the motion starts and the peaks present in the data become higher. The motion stops at around 32800 milliseconds, after this moment sensors two and three seem to oscillate around a value slightly above zero, and sensor one slightly below zero. The peak visible at around 30000 milliseconds is caused by plugging in the power supply of the manipulator.

The raw data is processed to find the reaction force in Y direction and the reaction moment around P_o. The reaction force is found by summing the forces of the individual sensors, see Equation E.1. The sensors are loaded in compression and show a negative force once compressed, therefore matching the convention used in Figure E.3. Figure E.7 shows the obtained reaction force. The measured signal again seems to contain a high-frequency oscillation. The moment where the movement starts is also visible in this plot. Once the motion stops the signal becomes very similar to what it was before motion happened.

$$\sum F_y = sensor_1 + sensor_2 + sensor_3 \tag{E.1}$$

To find the reaction moment around P_o the signals are multiplied by the distance to this point and added. In Equation E.2 this is written in equation form, the sign is chosen such that it matches the definition used in the simulation.

$$\sum M_o = -0.055 \cdot sensor_1 - 0.425 \cdot sensor_2 - 0.055 \cdot sensor_3 \tag{E.2}$$

In Figure E.8 the obtained reaction moment is plotted. Again this plot looks very similar to the other plots, where the signal seems to contain a high frequency oscillation. Looking closely at the part between $t = 31600$ and $t = 33000$ the amplitude of the signal seems to drop in the middle of this section. Furthermore, there is a difference of about $3Nmm$ in the signal before and after motion.

The experiments were repeated for movement of solely θ_4. In Figure E.9 the obtained raw data is plotted. Slightly after $t = 20000$ the signal changes shortly, here the sample rate changed temporarily

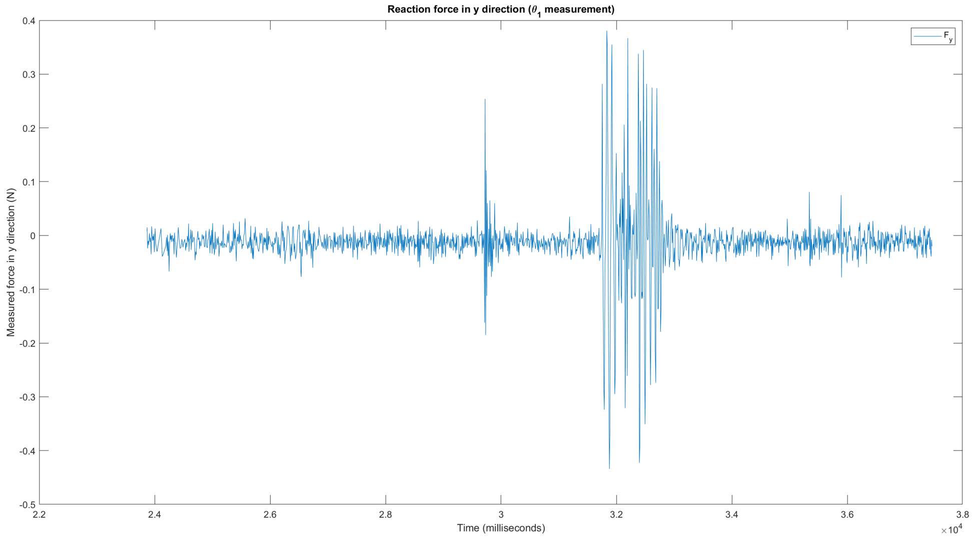

Figure E.7: Reaction force in Y-direction due to moving θ_1

from 10ms to 100ms, and the reason for this is unknown. The movement starts at around $t = 23500$, which is noticeable by the amplitude that rapidly increases. Once the manipulator is at rest the amplitude decreases again, and the signal becomes similar to what it was before the motion happened.

For this measurement, the reaction force in the Y direction is again determined by Equation E.1. The resulting plot is shown in Figure E.10. Again the signal seems to contain a high frequency oscillation.

Figure E.11 shows the reaction moment around P_o caused by the motion of θ_4, which is calculated by Equation E.2.

E.4. Changes final setup

The setup described in Chapter Three represents an evolution from the setups discussed here. The setups presented earlier all shared a common limitation: gravity acted within the same plane, necessitating sensors capable of supporting both reaction forces and counteracting gravity. Consequently, these sensors required a relatively high load rating. However, in the final setup, this issue was circumvented by rotating the manipulator and providing side support. This allowed for the utilization of more sensitive sensors.

In the setup outlined in this appendix, two sensors, sensors one and three, essentially measured the same force, resulting in a halving of the measured force magnitude. This outcome was undesirable due to the limited sensitivity of the sensors. However, this issue was rectified in the final setup. Additionally, the final setup facilitated the measurement of the reaction force in the x-direction by suspending the manipulator in rotated positions.

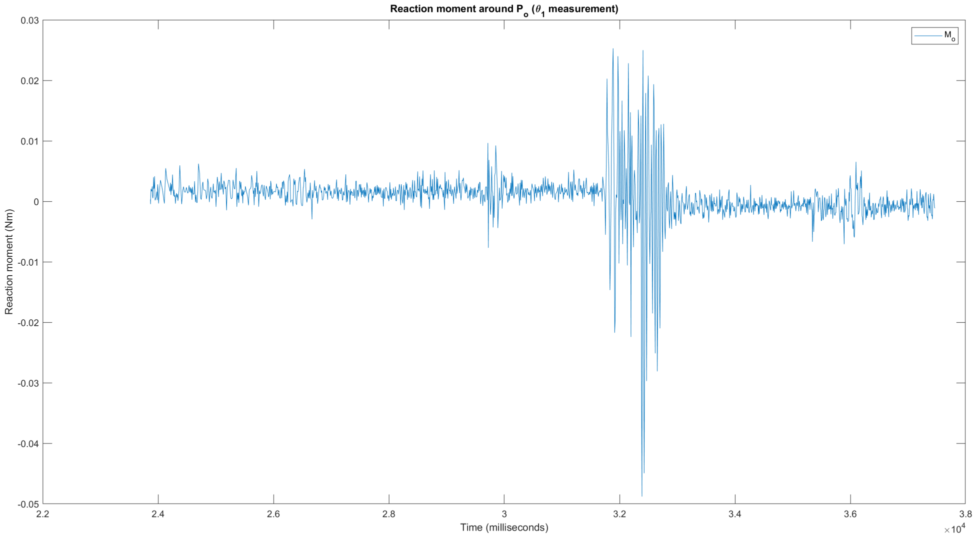

Figure E.8: Reaction moment around P_o due to moving θ_1

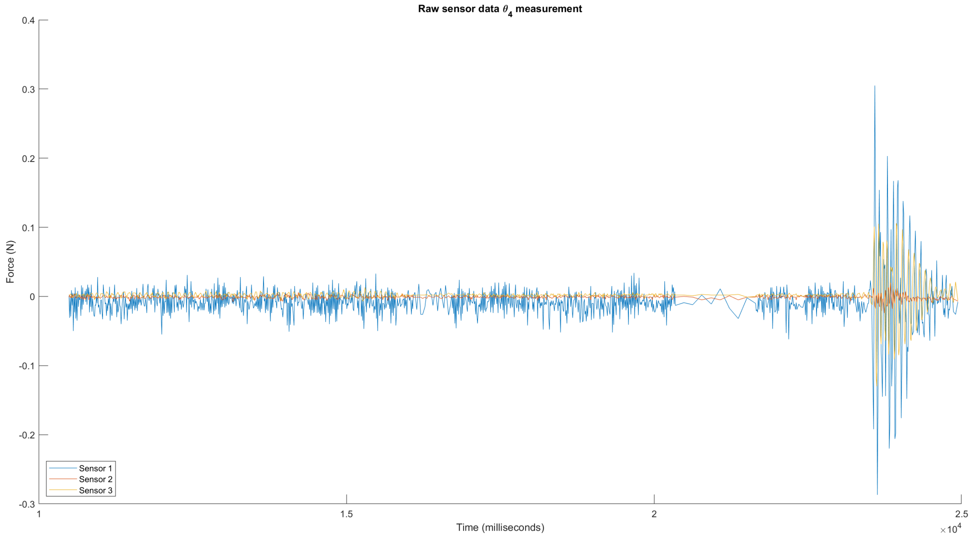

Figure E.9: Raw forces measured due to moving θ_4

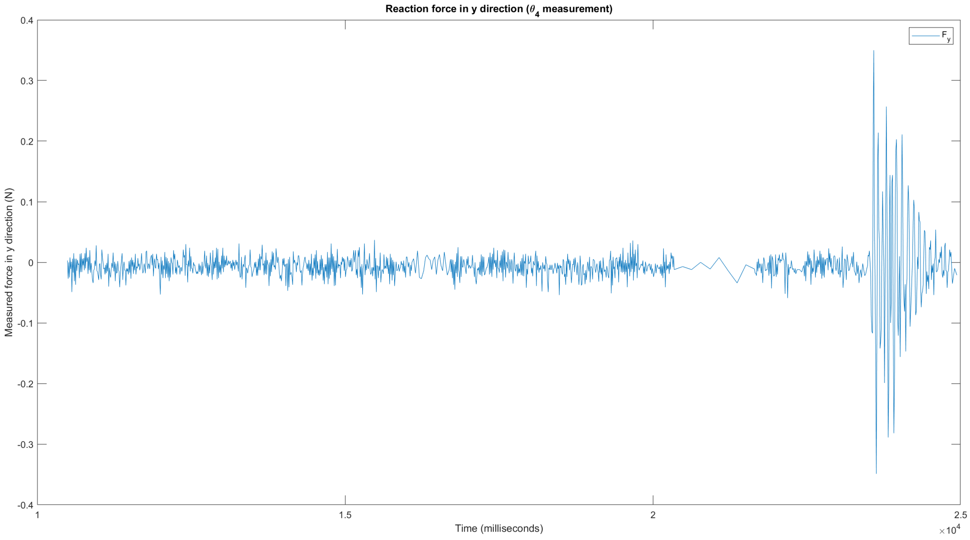

Figure E.10: Reaction force in Y-direction due to moving θ_4

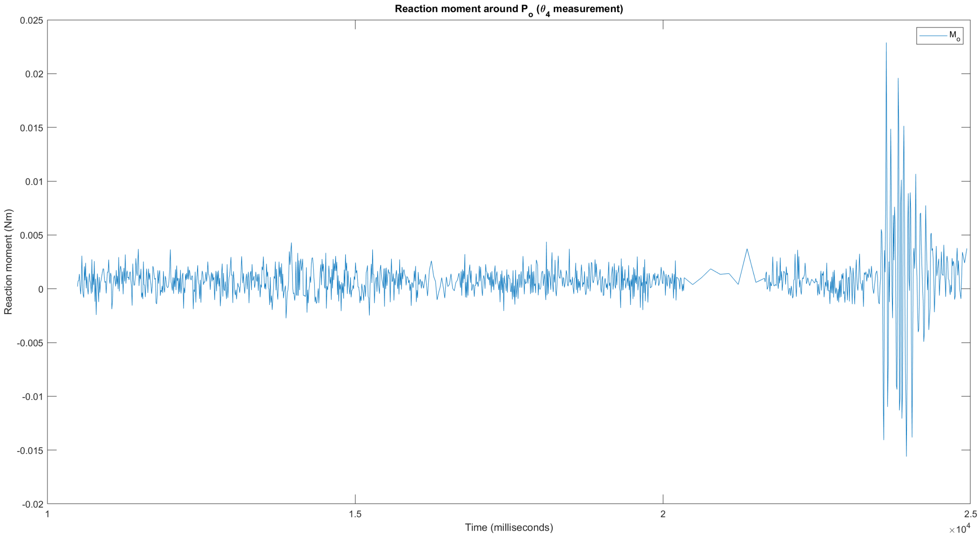

Figure E.11: Reaction moment around P_o due to moving θ_4

Bibliography

[1] https://www.aviastar.org/helicopters_eng/breguet_gyro.php, Accessed: 2024-02-18.

[2] S. Hamaza and M. Kovac, “Omni-drone: On the design of a novel aerial manipulator with omnidirectional workspace,” in *2020 17th International Conference on Ubiquitous Robots (UR)*, 2020, pp. 153–158. doi: 10.1109/UR49135.2020.9144837.

[3] F. Ruggiero, V. Lippiello, and A. Ollero, “Aerial manipulation: A literature review,” *IEEE Robotics and Automation Letters*, vol. 3, no. 3, pp. 1957–1964, 2018. doi: 10.1109/LRA.2018.2808541.

[4] H. Bonyan Khamseh, F. Janabi-Sharifi, and A. Abdessameud, “Aerial manipulation—a literature survey,” *Robotics and Autonomous Systems*, vol. 107, pp. 221–235, 2018, issn: 0921-8890. doi: https://doi.org/10.1016/j.robot.2018.06.012. [Online]. Available: https://www.sciencedirect.com/science/article/pii/S0921889017305535.

[5] P. E. I. Pounds, D. R. Bersak, and A. M. Dollar, “Grasping from the air: Hovering capture and load stability,” in *2011 IEEE International Conference on Robotics and Automation*, 2011, pp. 2491–2498. doi: 10.1109/ICRA.2011.5980314.

[6] G. Heredia, A. Jimenez-Cano, I. Sanchez, *et al.*, “Control of a multirotor outdoor aerial manipulator,” in *2014 IEEE/RSJ International Conference on Intelligent Robots and Systems*, 2014, pp. 3417–3422. doi: 10.1109/IROS.2014.6943038.

[7] K. Bodie, M. Tognon, and R. Siegwart, “Dynamic end effector tracking with an omnidirectional parallel aerial manipulator,” *IEEE Robotics and Automation Letters*, vol. 6, no. 4, pp. 8165–8172, 2021. doi: 10.1109/LRA.2021.3101864.

[8] Y. Ohnishi, T. Takaki, T. Aoyama, and I. Ishii, “Development of a 4-joint 3-dof robotic arm with anti-reaction force mechanism for a multicopter,” in *2017 IEEE/RSJ International Conference on Intelligent Robots and Systems (IROS)*, 2017, pp. 985–991. doi: 10.1109/IROS.2017.8202265.

[9] A. B. Clark, N. Baron, L. Orr, M. Kovac, and N. Rojas, “On a balanced delta robot for precise aerial manipulation: Implementation, testing, and lessons for future designs,” in *2022 IEEE/RSJ International Conference on Intelligent Robots and Systems (IROS)*, 2022, pp. 7359–7366. doi: 10.1109/IROS47612.2022.9981736.

[10] G. Lowen and R. Berkof, “Survey of investigations into the balancing of linkages,” *Journal of Mechanisms*, 1968.

[11] V. H. Arakelian and M. R. Smith, “Shaking Force and Shaking Moment Balancing of Mechanisms: A Historical Review With New Examples,” *Journal of Mechanical Design*, vol. 127, no. 2, pp. 334–339, Mar. 2005, issn: 1050-0472. doi: 10.1115/1.1829067. eprint: https://asmedigitalcollection.asme.org/mechanicaldesign/article-pdf/127/2/334/5921957/334_1.pdf. [Online]. Available: https://doi.org/10.1115/1.1829067.

[12] I. Kochev, “General theory of complete shaking moment balancing of planar linkages: A critical review,” *Mechanism and Machine Theory*, vol. 35, no. 11, pp. 1501–1514, 2000, issn: 0094-114X. doi: https://doi.org/10.1016/S0094-114X(00)00015-X. [Online]. Available: https://www.sciencedirect.com/science/article/pii/S0094114X0000015X.

[13] V. van der Wijk, J. L. Herder, and B. Demeulenaere, “Comparison of Various Dynamic Balancing Principles Regarding Additional Mass and Additional Inertia,” *Journal of Mechanisms and Robotics*, vol. 1, no. 4, p. 041 006, Sep. 2009, issn: 1942-4302. doi: 10.1115/1.3211022. eprint: https://asmedigitalcollection.asme.org/mechanismsrobotics/article-pdf/1/4/041006/5931432/041006_1.pdf. [Online]. Available: https://doi.org/10.1115/1.3211022.

[14] V. van der Wijk, “The grand 4r four-bar based inherently balanced linkage architecture for synthesis of shaking force balanced and gravity force balanced mechanisms,” *Mechanism and Machine Theory*, vol. 150, p. 103 815, 2020, issn: 0094-114X. doi: `https://doi.org/10.1016/j.mechmachtheory.2020.103815`. [Online]. Available: `https://www.sciencedirect.com/science/article/pii/S0094114X20300367`.

[15] V. van der Wijk, J. L. Herder, and B. Demeulenaere, “Comparison of Various Dynamic Balancing Principles Regarding Additional Mass and Additional Inertia,” *Journal of Mechanisms and Robotics*, vol. 1, no. 4, p. 041 006, Sep. 2009, issn: 1942-4302. doi: `10.1115/1.3211022`. eprint: `https://asmedigitalcollection.asme.org/mechanismsrobotics/article-pdf/1/4/041006/5931432/041006\_1.pdf`. [Online]. Available: `https://doi.org/10.1115/1.3211022`.

[16] V. van der Wijk and J. L. Herder, “Force balancing of variable payload by active force-balanced reconfiguration of the mechanism,” in *2009 ASME/IFToMM International Conference on Reconfigurable Mechanisms and Robots*, 2009, pp. 323–330.

[17] I. Kochev, “General theory of complete shaking moment balancing of planar linkages: A critical review,” *Mechanism and Machine Theory*, vol. 35, no. 11, pp. 1501–1514, 2000.

[18] C. Bagci, “Complete shaking force and shaking moment balancing of link mechanisms using balancing idler loops,” 1982.

[19] *Dynamic Balancing of Two-DOF Parallel Mechanisms Using a Counter-Mechanism*, vol. Volume 6B: 37th Mechanisms and Robotics Conference, International Design Engineering Technical Conferences and Computers and Information in Engineering Conference, V06BT07A001, Aug. 2013. doi: `10.1115/DETC2013-12107`. eprint: `https://asmedigitalcollection.asme.org/IDETC-CIE/proceedings-pdf/IDETC-CIE2013/55942/V06BT07A001/4254805/v06bt07a001-detc2013-12107.pdf`. [Online]. Available: `https://doi.org/10.1115/DETC2013-12107`.

[20] D. Boere, “The constant inertia mechanism and its use in a high-speed 2-dof inherently dynamically balanced parallel manipulator,” English, 2022.

[21] V. Van der Wijk, “Shaking-moment balancing of mechanisms with principal vectors and momentum,” *Frontiers of mechanical engineering*, vol. 8, pp. 10–16, 2013.

[22] J. J. de Jong and J. L. Herder, “A comparison between five principle strategies for adapting shaking force balance during varying payload,” in *Proceedings of the 14th World Congress in Mechanism and Machine Sciences, Taipei, Taiwan*, 2015, pp. 23–30.

[23] V. van Der Wijk, “The grand 4r four-bar based inherently balanced linkage architecture for synthesis of shaking force balanced and gravity force balanced mechanisms,” *Mechanism and Machine Theory*, vol. 150, p. 103 815, 2020.

[24] V. Van Der Wijk, S. Krut, F. Pierrot, and J. L. Herder, “Design and experimental evaluation of a dynamically balanced redundant planar 4-rrr parallel manipulator,” *The International Journal of Robotics Research*, vol. 32, no. 6, pp. 744–759, 2013.

[25] R. Ricard and C. M. Gosselin, “On the development of reactionless parallel manipulators,” in *International Design Engineering Technical Conferences and Computers and Information in Engineering Conference*, American Society of Mechanical Engineers, vol. 35173, 2000, pp. 493–502.

[26] M. J. Zomerdijk and V. van der Wijk, “Structural design and experiments of a dynamically balanced inverted four-bar linkage as manipulator arm for high acceleration applications,” in *Actuators*, MDPI, vol. 11, 2022, p. 131.

[27] L. Withagen, “Design of 3 dof and 6 dof force and moment balanced manipulators based on the spatial pantograph linkage,” English, 2023.